

**Naval Surface Warfare Center
Carderock Division**

West Bethesda, MD 20817-5700

NSWCCD-50-TR-2002/068 December 2002

Hydromechanics Directorate

Technical Report

**Hydrodynamic Performance of the Large Cavitation
Channel (LCC)**

by

Joel T. Park

J. Michael Cutbirth

Wesley H. Brewer



20030807 097

Approved for public release. Distribution unlimited.

**Naval Surface Warfare Center
Carderock Division**

West Bethesda, MD 20817-5700

NSWCCD-50-TR-2002/068 December 2002

Hydromechanics Directorate

Technical Report

**Hydrodynamic Performance of the Large Cavitation
Channel (LCC)**

by

Joel T. Park

J. Michael Cutbirth

Wesley H. Brewer

Approved for public release. Distribution unlimited.

This page intentionally left blank.

UNCLASSIFIED

| REPORT DOCUMENTATION PAGE | | | <i>Form Approved</i> OMB No. 0704-0188 | |
|---|------------------------------------|-------------------------------------|--|--|
| Public reporting burden for this collection of information is estimated to average 1 hour per response, including the time for reviewing instructions, searching existing data sources, gathering and maintaining the data needed, and completing and reviewing this collection of information. Send comments regarding this burden estimate or any other aspect of this collection of information, including suggestions for reducing this burden to Department of Defense, Washington Headquarters Services, Directorate for Information Operations and Reports (0704-0188), 1215 Jefferson Davis Highway, Suite 1204, Arlington, VA 22202-4302. Respondents should be aware that notwithstanding any other provision of law, no person shall be subject to any penalty for failing to comply with a collection of information if it does not display a currently valid OMB control number. PLEASE DO NOT RETURN YOUR FORM TO THE ABOVE ADDRESS. | | | | |
| 1. REPORT DATE (DD-MM-YYYY) 1-Dec-2002 | | 2. REPORT TYPE Final | | 3. DATES COVERED (From - To) - |
| 4. TITLE AND SUBTITLE Hydrodynamic Performance of the Large Cavitation Channel (LCC) | | | 5a. CONTRACT NUMBER | |
| | | | 5b. GRANT NUMBER | |
| | | | 5c. PROGRAM ELEMENT NUMBER | |
| 6. AUTHOR(S) Joel T. Park, J. Michael Cutbirth, and Wesley H. Brewer | | | 5d. PROJECT NUMBER | |
| | | | 5e. TASK NUMBER | |
| | | | 5f. WORK UNIT NUMBER | |
| 7. PERFORMING ORGANIZATION NAME(S) AND ADDRESS(ES) AND ADDRESS(ES) Naval Surface Warfare Center Carderock Division, Code 54 9500 MacArthur Boulevard West Bethesda, MD 20817-5700 | | | 8. PERFORMING ORGANIZATION REPORT NUMBER NSWCCD-50-TR-2002-068 | |
| 9. SPONSORING / MONITORING AGENCY NAME(S) AND ADDRESS(ES) Commander Naval Surface Warfare Center Carderock Division 9500 MacArthur Boulevard West Bethesda, MD 20817-5700 | | | 10. SPONSOR/MONITOR'S ACRONYM(S) | |
| | | | 11. SPONSOR/MONITOR'S REPORT NUMBER(S) | |
| 12. DISTRIBUTION / AVAILABILITY STATEMENT Approved for public release. Distribution unlimited. | | | | |
| 13. SUPPLEMENTARY NOTES | | | | |
| 14. ABSTRACT The U. S. Navy William B. Morgan Large Cavitation Channel (LCC) in Memphis, Tennessee, is the world's largest water tunnel. This report is a comprehensive documentation of its hydrodynamic performance. Three key characteristics of tunnel velocity were measured: temporal stability, spatial uniformity, and turbulence. Temporal stability and spatial uniformity were measured by laser Doppler anemometer (LDA), while the turbulence was measured with a conical hot-film and constant temperature anemometer (CTA). The velocity stability at a single point for run times greater than 2 hours was measured as +/- 0.15 % at the 95 % confidence level for velocities from 0.5 to 18 m/s. The spatial non-uniformity for the axial velocity component was +/-0.34 to +/-0.60 % for velocities from 3 to 16 m/s. The non-uniformity in the vertical velocity was nominally 2 %. The turbulence or relative turbulence intensity, which is the commonly reported performance characteristic for water tunnels, was measured as 0.2 to 0.5 % depending on tunnel velocity. Additional information includes calibration of the LDA and CTA, test section velocity as a function of pump speed, acceleration of the test section velocity, velocity spectra, and color contour plots of the axial and vertical components for velocity uniformity. The measurements demonstrate that the LCC is a high-quality world-class water tunnel. | | | | |
| 15. SUBJECT TERMS calibration, constant temperature anemometer (CTA), hot-film anemometer, laser Doppler anemometer (LDA), water tunnel, uncertainty analysis | | | | |
| 16. SECURITY CLASSIFICATION OF: | | | 17. LIMITATION OF ABSTRACT | 18. NUMBER OF PAGES |
| a. REPORT UNCLASSIFIED | b. ABSTRACT UNCLASSIFIED | c. THIS PAGE UNCLASSIFIED | SAR | 74 |
| | | | 19a. NAME OF RESPONSIBLE PERSON Joel T. Park, Ph. D. | |
| | | | 19b. TELEPHONE NUMBER (include area code) 901-947-3117 | |

This page intentionally left blank.

Contents

| | <i>Page</i> |
|---|-------------|
| Contents | iii |
| Figures..... | iii |
| Tables..... | v |
| Abstract..... | vi |
| Administrative Information | vi |
| Acknowledgements..... | vi |
| Summary | 1 |
| Introduction..... | 1 |
| Uncertainty Estimates in LDA Calibration..... | 3 |
| Tunnel Velocity | 6 |
| Long Term Temporal Stability | 6 |
| Tunnel Velocity from Pump Speed..... | 7 |
| Acceleration and Deceleration..... | 8 |
| Velocity Non-Uniformity..... | 9 |
| Turbulence | 12 |
| Theory | 12 |
| Experimental Method..... | 12 |
| Experimental Results | 13 |
| Conclusions..... | 15 |
| References..... | 67 |

Figures

| | <i>Page</i> |
|--|-------------|
| Figure 1. Schematic Drawing of the LCC [1]..... | 19 |
| Figure 2. LCC Test Section Cross-Section [1] | 19 |
| Figure 3. Uncertainty Estimates in LDA Calibration from Rotating Disk at 100 mm Radius..... | 20 |
| Figure 4. Relative Uncertainty in LDA Calibration from Rotating Disk | 20 |
| Figure 5. Uncertainty in LDA Calibration from Rotating Disk at 50 mm Radius..... | 21 |
| Figure 6. Residual Plot for Calibration of Axial Velocity Component | 21 |

| | |
|---|----|
| Figure 7. Residual Plot for Calibration of Vertical Velocity Component | 22 |
| Figure 8. Residual Plot for Calibration of Tunnel Velocity..... | 22 |
| Figure 9. Fiber Optic Probe Installation for Tunnel Velocity Measurement..... | 23 |
| Figure 10. Long-Term Temporal Stability of LCC Test Section Velocity..... | 24 |
| Figure 11. Time Series of Test Section Velocity for Submarine Model at 5 m/s..... | 24 |
| Figure 12. Time Series of Test Section Velocity for Submarine Model at 9 m/s..... | 25 |
| Figure 13. Time Series of Test Section Velocity for Hydrofoil Model at 18 m/s | 25 |
| Figure 14. Time Series of Empty Test Section at 0.2 m/s | 26 |
| Figure 15. Time Series of Empty Test Section at 0.5 m/s | 26 |
| Figure 16. Time Series of Empty Test Section at 3.0 m/s | 27 |
| Figure 17. Time Series of Empty Test Section at 12.0 m/s | 27 |
| Figure 18. Time Series of Empty Test Section at 16.0 m/s | 28 |
| Figure 19. Tunnel Velocity from Main Pump Speed for Linear Curve Fit | 29 |
| Figure 20. Tunnel Velocity Residuals from Main Pump Speed for Power-Law Fit | 30 |
| Figure 21. Velocity Residuals for LCC Open Water Dynamometer [12] | 30 |
| Figure 22. Test Section Acceleration from 1.6 to 6 m/s for NUWC Towed Array..... | 31 |
| Figure 23. Test Section Acceleration from 2.5 to 12 m/s for NUWC Towed Array..... | 31 |
| Figure 24. Test Section Deceleration from 6 to 1.6 m/s for NUWC Towed Array..... | 32 |
| Figure 25. Test Section Acceleration for Submarine Crashback at -600 rpm..... | 32 |
| Figure 26. Test Section Acceleration for Submarine Crashback at -200 rpm..... | 33 |
| Figure 27. Test Section Deceleration for Submarine Crashback at -600 rpm..... | 33 |
| Figure 28. Test Section Deceleration for Submarine Crashback at -200 rpm..... | 34 |
| Figure 29. Contour Plots for an Empty Test Section in Bay 1 at 3.1 m/s..... | 35 |
| Figure 30. Contour Plots for an Empty Test Section in Bay 1 at 9.2 m/s..... | 36 |
| Figure 31. Contour Plots for an Empty Test Section in Bay 1 at 15.4 m/s..... | 37 |
| Figure 32. Contour Plots for an Empty Test Section in Bay 7 at 3.1 m/s..... | 38 |
| Figure 33. Contour Plots for an Empty Test Section in Bay 7 at 9.1 m/s..... | 39 |
| Figure 34. Contour Plots for an Empty Test Section in Bay 7 at 15.3 m/s..... | 40 |
| Figure 35. Summary of Velocity Uniformity Measurements for 1996 | 41 |
| Figure 36. Summary of Spatial Variation in Axial Velocity | 41 |
| Figure 37. Summary of Spatial Variation in Vertical Velocity | 42 |
| Figure 38. Contour Plots for Test Section in Bay 2 Window 1 at 12 m/s in 1998 | 43 |
| Figure 39. Contour Plots for Test Section in Bay 2 Window 1 at 3 m/s in 2001 | 44 |
| Figure 40. Contour Plots for Test Section in Bay 2 Window 1 at 6 m/s in 2001 | 45 |
| Figure 41. Contour Plots for Test Section in Bay 2 Window 1 at 9 m/s in 2001 | 46 |
| Figure 42. Contour Plots for Test Section in Bay 2 Window 1 at 12 m/s in 2001 | 47 |
| Figure 43. Contour Plots for Test Section in Bay 2 Window 1 at 16 m/s in 2001 | 48 |
| Figure 44. Contour Plots for Test Section in Bay 4 Window 1 at 3 m/s in 2001 | 49 |
| Figure 45. Contour Plots for Test Section in Bay 4 Window 1 at 6 m/s in 2001 | 50 |
| Figure 46. Contour Plots for Test Section in Bay 4 Window 1 at 9 m/s in 2001 | 51 |
| Figure 47. Contour Plots for Test Section in Bay 4 Window 1 at 12 m/s in 2001 | 52 |
| Figure 48. Contour Plots for Test Section in Bay 4 Window 1 at 16 m/s in 2001 | 53 |
| Figure 49. Hot-Film Support Fixture and Submarine Strut at Test-Top Stand | 54 |
| Figure 50. Hot-Film in Test Section with LDA in Operation in Bay 4 Window | 54 |
| Figure 51. Inflow to Conical Hot-Film 2 mm Upstream at 15 m/s..... | 55 |
| Figure 52. Inflow to Conical Hot-Film 2 mm Upstream at High Resolution..... | 56 |

| | |
|--|----|
| Figure 53. Test Section Turbulence from Hot-Film in Comparison to LDA Noise..... | 57 |
| Figure 54. Velocity Frequency Spectrum for 0.5 m/s..... | 57 |
| Figure 55. Velocity Frequency Spectrum for 2 m/s..... | 58 |
| Figure 56. Velocity Frequency Spectrum for 4 m/s..... | 58 |
| Figure 57. Velocity Frequency Spectrum for 9 m/s..... | 59 |
| Figure 58. Velocity Frequency Spectrum for 14.5 m/s..... | 59 |
| Figure 59. Measured Cutoff Frequency of Turbulence from Spectra..... | 60 |

Tables

| | <i>Page</i> |
|--|-------------|
| Table 1. Optical Characteristics for Dantec 85 mm Fiber Optic Probe..... | 61 |
| Table 2. Optical Characteristics for Dantec 112 mm Fiber Optic Probe..... | 61 |
| Table 3. Window Locations Relative to Test Top Opening | 62 |
| Table 4. Statistics of Measurements for Test Section Velocity Uniformity | 63 |
| Table 5. Statistics for Velocity Uniformity Measurements for HiFoil Experiment | 63 |
| Table 6. Characteristics of U. S. Water Tunnels and SSPA | 64 |
| Table 7. Summary of Turbulence Data for TSI IFA-300 CTA | 65 |
| Table 8. Summary of Turbulence Data for Dantec StreamLine CTA | 66 |

Abstract

The U. S. Navy William B. Morgan Large Cavitation Channel (LCC) in Memphis, Tennessee, is the world's largest water tunnel. This report is a comprehensive documentation of its hydrodynamic performance. Three key characteristics of tunnel velocity were measured: temporal stability, spatial uniformity, and turbulence. Temporal stability and spatial uniformity were measured by laser Doppler anemometer (LDA), while the turbulence was measured with a conical hot-film and constant temperature anemometer (CTA). The velocity stability at a single point for run times greater than 2 hours was measured as $\pm 0.15\%$ at the 95 % confidence level for velocities from 0.5 to 18 m/s. The spatial non-uniformity for the axial velocity component was ± 0.34 to $\pm 0.60\%$ for velocities from 3 to 16 m/s. The non-uniformity in the vertical velocity was nominally 2 %. The turbulence or relative turbulence intensity, which is the commonly reported performance characteristic for water tunnels, was measured as 0.2 to 0.5 % depending on tunnel velocity. Additional information includes calibration of the LDA and CTA, test section velocity as a function of pump speed, acceleration of the test section velocity, velocity spectra, and color contour plots of the axial and vertical components for velocity uniformity. The measurements demonstrate that the LCC is a high-quality world-class water tunnel.

Administrative Information

The work described in this report was performed by the Memphis Detachment of the Naval Surface Warfare Center, Carderock Division (NSWCCD), Code 5102, and funded by the operations and maintenance budget of the Large Cavitation Channel.

Acknowledgements

The support and encouragement by Dr. William B. Morgan, former directorate head of Hydromechanics (Code 50) over the last several years is gratefully acknowledged. Dr. Morgan was responsible for the employment of all of the authors at the LCC. Dr. Morgan also provided some very valuable comments for this report. Mr. William G. Day, Jr., former department head of Code 5100, has more recently provided support and encouragement for the writing of this report. Mr. Robert J. Etter of Code 5400 developed the ideas for the support structure for the hot-film probe for the measurement of the tunnel turbulence and supervised the fabrication of the hardware. Dr. George Papadopolous of Dantec Dynamics assisted with the Dantec instrumentation for the turbulence measurements. The excellent support by the LCC Operations staff for the measurements in this report is gratefully acknowledged. Finally, Mr. James N. Blanton supplied the technical leadership and foundation for many of the experiments in this report during his tenure at the LCC. The first author of this report has known Mr. Blanton since he was a graduate student at the University of Texas, the second author had the same thesis advisor, and the third author worked with him at the LCC.

Summary

This report documents the hydrodynamic performance of the U. S. Navy William B. Morgan Large Cavitation Channel (LCC). The LCC is the largest water tunnel in the world and is located on the site of the Memphis Detachment of NSWCCD in Memphis, Tennessee. The experimental results are probably the most comprehensive available for any major water flow facility. The significant results of the measurements are as follows:

- **Temporal Velocity Stability.** The long-term velocity stability as measured by laser Doppler anemometry (LDA) at a single point for run times exceeding two hours is $\pm 0.15\%$ at the 95 % confidence level for test section velocities from 0.5 to 18 m/s (1.6 to 59 ft/s).
- **Spatial Velocity Uniformity.** The axial velocity variation in a rectangular cross-section over 17 % of the test section cross-sectional area was measured as ± 0.34 to $\pm 0.60\%$ at the 95 % confidence level for velocities from 3 to 16 m/s (9.8 to 52 ft/s). The results exceed the design goal of 1 %. The lower values were near the middle of the channel, where most models are located. The higher values were near the test section entrance. The variation in the vertical velocity component was nominally 2 %. The velocity variation of both the axial and vertical velocity components are presented in color contour plots.
- **Turbulence.** The turbulence or relative turbulence intensity, u'/U , was measured directly in the test section by a conical hot-film with a constant temperature anemometer (CTA), where u' is the standard deviation and U is the mean velocity. This is the most commonly reported performance measurement for a water tunnel. The measured value was between 0.2 % and 0.5 % depending on velocity. The velocity range of the measurements was 0.5 to 15 m/s (1.6 to 49 ft/s). Computations of the power spectra indicate that the velocity varies smoothly with frequency, and no harmonics appear in the flow.

Additional information includes calibration of the LDA and CTA, test section velocity as a function of pump speed, and acceleration of test section velocity. The measurement results demonstrate that the LCC is a high-quality world-class water tunnel.

Introduction

The U. S. Navy William B. Morgan Large Cavitation Channel (LCC) in Memphis, Tennessee, is the largest closed circuit water tunnel in the world. This publication documents the most recent performance measurements of the hydrodynamic characteristics of the channel. The design and early performance measurements were described initially by Etter and Wilson [1], [2]. The geometry and dimensions of the channel are shown schematically in Figure 1.

Historically, water tunnels and wind tunnels were symmetrical in design. The LCC was designed with a flat top so that the test section could operate at lower pressure and avoid vapor pressure in adjacent parts of the circuit. Additionally, the flat top design reduces the volume of water necessary to drain down to the test section for personnel access. Typically, water tunnels had relatively large contraction ratios, 9 and greater. A contraction ratio of 6.0 was selected for

the LCC to reduce construction costs without sacrificing flow quality. A comparison of the LCC with other water tunnels is summarized later in this report.

The walls of the tunnel are manufactured from 304 stainless steel. The tunnel is 72.8 m (239 ft) long and 19.8 m (65 ft) high and contains 5,300 m³ (1.4 x 10⁶ gallons) of water. The test section is 13.1 m (43 ft) long at the test top opening with a 3 m (10 ft) square cross section. The cross-sectional area is 8.99 m² (96.77 ft²). A diagram of the cross section for the test section is presented in Figure 2. As the figure indicates, the corners contain flat fillets with viewing ports where the flats are 539 mm (21 in) wide.

As shown in Figure 1, the settling chamber contains a flow straightener followed by honeycomb for turbulence management. The settling chamber is 7.37 m (24.2 ft) square with 762 mm (30 in) radius fillets in the corners. At the entrance of the settling chamber, the flow straightener consists of 102 mm (4 in) square cells by 610 mm (24 in) long. The honeycomb is stainless steel with 5.6 mm (7/32 in) across flats hexagonal cells with a length of 483 mm (19 in). The distance between the flow straightener and honeycomb is 610 mm (24 in).

The contraction section is asymmetric with an area ratio of 6.0. The pump is a seven bladed propeller with a diameter of 5.5 m (18 ft) and is directly driven by a 10 MW (14,000 hp) electric motor. The shaft speed is variable between about 1 and 60 rpm. The test section has a highly stable water velocity between 0.5 and 18 m/s (1.6 and 59 ft/s). Pressure at the test-section top is variable from 0.03 to 4 atm (0.5 to 60 psia). The tunnel was designed for velocity non-uniformity of 1 % in the test section and a relative longitudinal turbulence intensity of 0.1 %.

Previous measurements of the LCC hydrodynamic performance were reported by Blanton [3] and Blanton and Etter [4]. Measurements of tunnel velocity were from dynamic pressure measurements. The uncertainty in test section velocity was stated as ± 0.04 m/s (± 0.14 ft/s) at the 95 % confidence level for 15.2 m/s (50 ft/s) or ± 0.28 % [3]. For speeds greater than 6.1 m/s (20 ft/s), the uncertainty in test section velocity was estimated to less than ± 0.5 % at the 95 % confidence level.

The non-uniformity of the tunnel velocity was measured upstream of a submarine model [4]. The non-uniformity was measured and presented as a contour plot from a two-component LDA (laser Doppler anemometer) system. Near the tunnel entrance at 11.87 m/s (39.0 ft/s), the non-uniformity of the axial velocity component was ± 0.8 %, while just upstream of the model it was ± 0.6 %. For the vertical velocity component, the maximum deviation near the tunnel entrance was 3.6 % of the axial velocity or a maximum flow angle of 2°. Upstream of the model, the average vertical velocity was 1 % or 0.5°.

Since the measurements by Blanton [3] and Blanton and Etter [4], a number of improvements in procedures, instrumentation, and hardware have occurred. These include the following:

- New controller for the main drive motor
- New Dantec BSA processors for the LDA with new software
- Channel velocity by LDA rather than dynamic pressure
- Calibration of LDA by spinning disk with new calibration procedures
- New stepper motors for LDA traversing system

- New TSI IFA 300 CTA (constant temperature anemometer) with hot-film conical probes.

The new measurement results contained in this publication include the following:

- Uncertainty estimates in velocity from LDA via calibration by spinning disk
- Long-term temporal velocity stability at a single point in an empty test section (no model) by LDA
- High resolution contour plots of spatial variation in velocity at different tunnel velocities and two test section locations for the vertical and axial velocity components in an empty test section by LDA
- Longitudinal relative turbulence intensity measurements in the test section by hot-film anemometer.

Uncertainty Estimates in LDA Calibration

The LDA system at the LCC consists of 4 Dantec BSA 57N11 signal processors, 3 fiber optic probes, two Spectra Physics 6 Watt Argon-Ion lasers (models 2016 and 2017), a Dantec 3 D traverse with remote control, and Dantec Flow software. Two of the heads are two velocity components with wavelengths of 514.5 nm and 488.0 nm. The third head is single component, operates at a wavelength of 476.5 nm, and monitors tunnel speed usually in window 2 of bay 1 in the channel. The two-component heads operate with a beam expander and 1,600 mm lens, while the single component laser uses an 800 mm lens with a beam expander. One two-component head and the one single component head are Dantec 85 mm probes while the other two-component head is a 112 mm probe. The optical parameters for the 85 mm and 112 mm probes are summarized in Table 1 and Table 2, respectively.

A two-component optical head is mounted on three-dimensional traversing system for the measurement of local velocity for models and an empty test section. The traverse has a range of 1,200 mm (3.9 ft) in the y and z directions and 1,300 mm (4.3 ft) in the x direction where x is positive in the direction of flow (north), y is positive in the transverse direction toward the control room (west), and z is positive in the vertical direction. For the y-direction, the software contains a magnification factor for the index of refraction of water; consequently, the traverse range in water in the y-direction is 1,600 mm (5.2 ft).

The tunnel has 8 bays of windows with 2 windows per bay. For local velocity measurements, the traversing system can be positioned in bays 3 through 7 for measurements through the two windows in a bay. The window locations at window center are listed in Table 3 relative to leading edge opening for the test top.

The original traversing system included a Dantec 41N10 Traversing Amplifier with Baldor DC motors with optical encoders. The resolution was ± 0.001 mm with an accuracy of ± 0.05 mm. On 7 March 2000, the controller and motors were replaced with an Isel-Schrittmotor-Controller C142-4.1 and stepper motors. The stepper motors have a resolution of ± 0.005 mm.

The LDA is calibrated directly as a system with a rotating disk. The disk is 228.6 mm (9 inches) in diameter covered with 60-grit emery paper. A precision blind hole is located at the center of the disk with a diameter of 1.02 mm (0.040 inch). The disk is driven by a CompuMotor

Model SM233BE-NTQN motor and CompuMotor TQ10X Servo-Controller. The maximum velocity is rated at 200 rps, but typically the unit is operated at a maximum of 30 rps. The manufacturer's stated accuracy is ± 0.04 rps.

The magnitude of the velocity on the rotating disk is given by

$$V = 2\pi r \omega \quad (1)$$

where r is the distance from the center of the disk and ω is the rotational rate of the disk in revolutions per second (rps). Uncertainty estimates were performed in accordance with the methods of Coleman and Steele [5] and the ISO Uncertainty Guide [6]. The uncertainty in V is then given by

$$U_V^2 = (2\pi\omega)^2 U_r^2 + (2\pi r)^2 U_\omega^2 \quad (2)$$

or the relative uncertainty is

$$(U_V / V)^2 = (U_r / r)^2 + (U_\omega / \omega)^2 \quad (3)$$

where U_x is the uncertainty in x at the 95 % confidence level.

For a typical calibration, the following procedures are executed:

- The laser power is set to 200 mW, and the photo-multiplier tube (pmt) voltage is to about 600 volts.
- The focal point of the head is located at the center of the disk with the disk rotating at 10 rps or other low speed.
- The laser is then moved to 100 mm from the center in the z-direction for axial velocity and in the x-direction for the vertical velocity
- The y-distance from the disk is adjusted for maximum data rate on the processors.

The center of the disk is then relocated at the center with at least 6 repeat measurements.

Most of the uncertainty in the radial distance, r , is assumed to be in the location of the center of the disk. For the combined uncertainty, the student t is applied as the coverage factor rather than 2 as in the ISO Uncertainty Guide [6]. Thus, the uncertainty in the mean value of x and z for n measurements of the disk center is

$$U_x = t_{95} \sigma_x / \sqrt{n} \quad (4)$$

where t_{95} is the inverse student t at the 95 % confidence limit and σ_x is the standard deviation in x. In an example measurement for the new traverse controller and stepper motors, $t_{95} = 2.57$, $\sigma_x = \sigma_z = 0.042$, and $U_x = U_z = 0.044$ mm. After the repeat measurements for the center of the disk, the traverse is re-indexed at the center of the disk at the mean values of the x and z measurements. From equation (3), the contribution in relative uncertainty in the reference velocity due to position uncertainty is ± 0.044 % at all velocities for a radius of 100 mm. The actual value of the uncertainties for each experiment is dependent upon the operator, the traverse, and the fiber optic head and lens combination.

For the case where repeat measurements of are not done in the location of the center of the disk, the standard deviation of a previous measurement may be applied to the uncertainty. For example, $n = 1$, and $U_x = U_z = 2.57 * 0.042 = 0.11$ mm from the last paragraph. The relative uncertainty in velocity for center location is ± 0.11 % for a radius of 100 mm, which is still a small contribution.

The relative uncertainty in velocity from rotational speed decreases with increasing velocity. That is at the lower speed, uncertainty in rotational speed is the dominant term while at the higher speed the contribution in the uncertainty of r becomes more important. A typical result for the uncertainty in axial velocity is shown in Figure 3 for a radius of 100 mm while the relative uncertainty is presented in Figure 4. In this example, $\sigma_z = 0.029$ mm for 6 repeat measurements or $U_z = 0.0307$ mm. As stated previously, the uncertainty in the rotational rate is ± 0.04 rps. From these figures, the total uncertainty for $1 < \omega < 30$ rps or $0.62 < V < 18.85$ m/s is $4.0 > U/V > 0.14$ % or $0.025 < U_v < 0.027$ m/s.

The estimated uncertainty during calibration consists of three elements as indicated in Figure 3 and Figure 4: the rotational speed, position, and noise from the LDA. The uncertainty in velocity from rotational speed and position was computed from equations (1) and (2). The estimates from rotational speed and position were evaluated by Type B methods via the ISO Uncertainty Guide [6]. The LDA noise is a third contribution, which was computed by Type A evaluation. In this case, equation (4) is applied. Typically, the standard deviation from the LDA system was about 1 % of reading. The uncertainty in velocity from the LDA was usually based upon a 1000-sample average; consequently, the uncertainty from the LDA is typically ± 0.06 %. For the data in Figure 3 and Figure 4, the measured standard deviation was 0.4 %, which resulted in an uncertainty contribution from the LDA of less than ± 0.03 % over most of the velocity range.

Some benefit can be gained with a radius of 50 mm. This result is shown in Figure 5. Although the relative influence of the uncertainty in radius increases, the uncertainty in rotational speed still dominates. The end result is that the uncertainty is reduced by a factor of 2 at the lower speeds, while a significant improvement is still attained at the higher velocities.

In Figure 5, the results are compared to those of Bean and Hall [7] at the National Institute of Standards and Technology (NIST). Their calibration is from a single rotating wire attached to a cylinder and may be near the practical limit of uncertainty. Potentially, the uncertainty in the LCC measurements could be reduced by another factor of 2 relative to a 50 mm radius calibration.

Usually, the LDA system was calibrated in increments of 1 or 2 rps from 1 to 30 rps ($0.62 < V_x < 18.85$ m/s) for the axial component and from 1 to 10 rps ($0.62 < V_z < 6.28$ m/s) for the vertical velocity. The negative values of velocity were usually acquired by moving the fiber

optic head to the opposite side of the disk; however, the same result can be accomplished by fixing the fiber optic probe and reversing the direction of rotation. Movement of the fiber optic probe to the opposite side of the disk requires some care to insure that the disk is parallel to the probe; otherwise, the disk will not intersect the probe volume in the same location. For the calibrations, the probe volume was located at a position normal to the disk that yielded the maximum data rate. Calculations for the calibrations were based upon a statistical theory of Scheffé [8] and Carroll, et al. [9]. Essentially, the slope and offset are determined by a linear regression of the calibration data with the reference as the independent variable. On the basis of the statistical theory, the uncertainty in curve fit is computed. The linear regression equation is

$$V_m = a + bV_r \quad (5)$$

where V_r is the reference velocity from the spinning disk, V_m is the measured velocity from the Dantec processors and software, a is the intercept and b is the slope. From equation (5), the following equation is applied to subsequent data from the experiment:

$$V_r = A + BV_m \quad (6)$$

where $A = -a/b$ and $B = 1/b$. Typically, the uncertainty in the linear regressions is ± 0.015 to ± 0.020 m/s. Normally, three BSA processors were employed for experiments with BSA 1 for the local axial velocity, BSA 2 for the local vertical velocity, and BSA 3 for the tunnel velocity. BSA 1 and BSA 2 process the velocity signals from the optical head on the traverse, while BSA 3 processes the data from a head mounted near the test section entrance. For the measurement of three velocity components, the fourth processor is used for tunnel velocity.

Figures of the residual plots for calibration data are presented in Figure 6, Figure 7, and Figure 8 for the local axial, local vertical, and tunnel velocity, respectively. The data in these figures are plotted as the difference between the measured data and the linear regression in equation (6). The error bars are the uncertainties in the velocity from the rotating disk while the dashed lines are the uncertainties in the calibration from the linear regression analysis as a consequence of correcting the data with equation (6). The dominant uncertainty in the calibration is from the rotating disk. The error bars have been reduced with the new controller and new stepper motors in comparison to the previous traversing system.

Figure 6 and Figure 8 contain outliers that were excluded from the regression analysis. The outliers in these figures and in subsequent figures in this paper were determined by Chauvenet's criterion [5].

Tunnel Velocity

Long Term Temporal Stability

Tunnel velocity is monitored by LDA, which is normally located at window 2 of bay 1. From the table, tunnel velocity is measured at 978 mm (38.5 in) from the test top opening. The fiber optic probe normally used is the single component Dantec 85 mm fiber optic probe with an 800 mm focal length lens and beam wavelength of 476.5 nm. The optical characteristics are

listed in Table 1, and a typical calibration is shown in Figure 8. The installation is shown in the photograph in Figure 9. In this photograph, the fiber optic head is the 2-component 85 mm probe with an 800 mm lens and 514.5 nm wavelength beams.

A number of measurements have been completed to quantify the long-term velocity stability of velocity in the test section. These measurements are summarized in Figure 10. For the more recent measurements, the uncertainty in velocity from variations in flow speed at 0.5 to 18 m/s is 0.15 % at the 95 % confidence level for run durations greater than 2 hours.

Earlier measurements were performed with a submarine model 5495 for Bridges, et al. [10]. The model length was 6.92 m (22.7 ft), and diameter 0.623 m (2.04 ft). The results of the time series are shown in Figure 11 and Figure 12 at 5 m/s and 9 m/s (16 and 30 ft/s), respectively. At 5 m/s, the model was pitched 9.5°, while at 9 m/s the angle was 5°. The durations of these experiments were 9 hours and 16 hours with a total variation at the 95 % confidence level in velocity of 0.21 and 0.25 %, respectively. Each point in the time series is from an average of 500 to 1,000 samples.

For Bourgoyne, et al [11], the tunnel was operated at speeds up to 18 m/s with a 2-dimensional hydrofoil model. The model had a span of 3.05 m (10 ft), chord of 2.13 m (7 ft), and thickness of 171 mm (6.72 in). The time series for a 2-hour run at 18 m/s is presented in Figure 13. The time series contains 945 data points. Each point is a 1,000-sample average that was acquired automatically each time the traverse was moved in the acquisition of data for the model.

For possible test requirements at very low tunnel speeds or low Reynolds numbers, tunnel flow stability was measured at flows of 0.2 and 0.5 m/s (0.64 and 1.7 ft/s), which correspond to approximately 1 and 2 rpm pump speeds. These measurements were performed with no model in the tunnel, i. e. empty test section. The results for a 2-hour run time are presented in Figure 14 and Figure 15 for 0.2 and 0.5 m/s, respectively. The data were acquired with manual sampling of the data about every 5 minutes. Again each point in the time series is an average of 1,000 samples. These results indicate that 0.5 m/s is the lowest speed attainable for a flow stability of ± 0.15 %. At 0.5 m/s, the measured standard deviation was 0.38 mm/s (0.015 in/s). At these low speeds, approximately 15 to 20 minutes is necessary before the speed becomes stable. In Figure 15, speed stability had not been attained with the first data point; consequently, it is an outlier.

Additional empty test section data were obtained during the non-uniformity experiments. For the non-uniformity tests, velocity measurements were acquired at 672 grid points. Tunnel velocity was measured during data acquisition at each grid point. The resulting time series are presented in Figure 16, Figure 17, and Figure 18 for tunnel velocities of 3.0, 12.0, and 16.0 m/s (9.8, 39, and 52 ft/s), respectively. As these figures indicate, tunnel velocity variation was less than ± 0.15 %.

Tunnel Velocity from Pump Speed

LDA is the most accurate method for the measurement of tunnel velocity. The velocity is adjusted by the channel operators by digitally setting the pump speed in rpm. The pump speed can be set within ± 0.01 rpm. An example of the velocity for an empty test section as a function of the main drive motor speed is shown in Figure 19a. In this figure, the uncertainty in velocity is smaller than the symbols. As the figure indicates, the velocity is highly linear. All of the data appears to lie on a straight line. However when the data are plotted as residuals as shown in

Figure 19b, the data systematically deviates from a straight-line curve fit. In fact, a discontinuity exists in the curve fit. At pump speeds below 7 rpm or 2 m/s (6.6 ft/s), the fit appears to be linear but with a different slope and intercept. For pump speeds greater than 7 rpm, the curve is non-linear. Some care must be taken in the acquisition of data for stable speeds for this calibration. From the slope of this curve (0.32 m/s/rpm), tunnel speed can be adjusted within one or two iterations for a precise set-point velocity by LDA.

The data in Figure 19 were re-evaluated with two different curve fits. From a commercial computer code, "TableCurve2D," an optimal curve fit was computed to be a power-law with an exponent of 1.04. The results are presented in Figure 20. As the figure indicates, the prediction limit at the 95 % confidence level of the non-linear fit is about ± 0.02 m/s. This value is not significantly larger than the data scatter in the LDA calibration of Figure 8. The uncertainty in the velocity from LDA is only slightly larger than the prediction limit. At the lower velocities below about 2 m/s, the data are linear with nearly the same slope of 0.32 m/s/rpm. After tunnel speed is calibrated by the method in Figure 20, tunnel speed can be reproduced by rpm setting almost within the uncertainty of the LDA calibration.

With a model in the tunnel, the velocity calibration from pump speed will be different from an empty test section. However, the tunnel speed can be set to a precise speed by LDA within one or two iterations from the empty test section data. Additionally, a powered model will also influence velocity. The propeller acts as a pump and adds an incremental velocity of about 0.5 % in comparison to the dummy hub case at 12.2 m/s (40 ft/s), which is typical test condition for a submarine model. An example of the comparison of the powered and dummy hub test is presented in Donnelly, et al. [12], for the LCC open water dynamometer and is included for comparison in Figure 21.

Acceleration and Deceleration

Some experimenters have been interested in the effects of changes in velocity on model loads. A related question is the time required for test section velocity changes. Results are available for two experiments: towed array experiment sponsored by the Naval Undersea Warfare Center (NUWC) in Newport, Rhode Island, and a submarine crashback experiment by Mississippi State University. In both examples, the effect of tunnel acceleration on model loads was the primary purpose. However, these tests also provide quantitative information on the time necessary for velocity stability.

For the towed array test, tunnel blockage was low and was probably similar to an empty test section. Acceleration results are presented in Figure 22 and Figure 23. In these figures, velocity has been normalized with the higher stable velocity, and the dashed lines are the mean velocities of the two stable speeds. In Figure 22, channel speed was changed from 1.6 to 6 m/s (5.1 to 19.7 ft/s) while in Figure 23 the change was from 2.5 to 12.1 m/s (8.4 to 39.7 ft/s). In both cases, the acceleration was nearly the same, 0.047 and 0.044 m/s² (0.0048 and 0.0045 standard g where $g = 9.80665$ m/s²) for the linear region of velocity change. Consequently, the time for speed stability was higher for the larger velocity change. In Figure 22, approximately 175 s was necessary for speed stability at 6 m/s while over 250 s were required at 12 m/s in Figure 23. Nominally, 300 s (5 min) are required for channel speeds greater than 5 m/s.

An example of deceleration is shown in Figure 24 for a speed change from 6 m/s to 1.6 m/s, which is the reverse of Figure 22. The deceleration in the linear part of the curve is -0.086

m/s^2 (-0.0088 standard g), which is almost double the acceleration in Figure 22. However, attaining speed stability requires over 250 seconds, which is significantly larger than the 175 s for acceleration between the same velocities. At lower speeds less than 5 m/s (16 ft/s), 15 to 20 minutes may be required for speed stability.

The acceleration examples for a submarine model in crashback are significantly different. The submarine model was model 5495, which is the same one described in Bridges, et al. [10] but with a propeller. For these examples, the speed changes were between zero (zero pump rotation) and 2.5 m/s (8.3 ft/s) and between zero and 5 m/s (16.4 ft/s). The most dramatic effect is seen in Figure 25, where the tunnel speed is increased to 2.5 m/s with the propeller speed at -600 rpm. At the beginning of the run, the tunnel flow is reversed, and the propeller is acting as a pump at the no flow condition. The minimum velocity is -0.38 m/s (-1.2 ft/s). The acceleration is nearly constant initially, then decreases, and increases linearly again. The time to attain near speed stability is about 440 s.

For the 5 m/s case in Figure 26, the propeller speed is -200 rpm. The effect of the lower propeller speed is less dramatic. The initial tunnel velocity is nearer zero. The initial acceleration is almost linear and increases to higher value at 110 s after the beginning of the measurement. Speed stability is attained at 220 s, which is about half the time at 2.5 m/s.

The deceleration curves are similar to those of the towed array tests. In Figure 27 at 2.5 m/s and propeller speed of -600 rpm, the velocity decays to zero in about 480 s and becomes negative. At 5 m/s and a propeller speed of -200 rpm, the velocity does not quite decay to zero in 600 s in Figure 28. In the LCC open water dynamometer test [12], the tunnel reached a stable speed at no flow in about 20 minutes with a propeller speed of 660 rpm and zero pump rotation. The final tunnel velocity was 0.435 m/s (1.4 ft/s). Nominally, 30 minutes are required for the tunnel velocity to become zero without propulsion. When the LDA system registers a magnitude of mean velocity of less than 10 mm/s (0.39 in/s), the flow is considered to be zero for a model without propulsion.

Velocity Non-Uniformity

As stated previously, one of the measures of hydrodynamic performance is velocity non-uniformity. The design specification for the LCC was 1 % [1], [2]. Subsequently, velocity non-uniformity was measured as 0.6 to 0.8 % with a submarine model in the channel [4]. Later in 1996, velocity uniformity was measured for an empty test section with the same equipment. The processor was a Dantec 58N10 PDA (Particle Dynamics Analyzer). Measurements were accomplished with a 2,000 mm focal-length lens. The vertical and axial velocity components were measured in two separate surveys.

Contour plots of the axial and vertical velocity components are presented in Figure 29 through Figure 31 for bay 1 and Figure 32 through Figure 34 for bay 7. The nominal velocities for these figures are 3, 9, and 15 m/s (10, 30, and 50 ft/s), respectively. The dimensions of the survey regions were, typically, 900 by 2,200 mm (2.95 by 7.22 ft) with a spatial resolution of 100 mm wide by 150 mm high (3.9 by 5.9 in), or the cross-sectional area of the survey was 22 % of the test section cross-sectional area. The number of spatial points in the surveys was 140 to 150 outside the boundary layer. The axial velocities were adjusted with the centerline velocity so that the value at the center of the channel is 1.0 while the vertical velocity was shifted for a

value of zero at the center. The spatial coordinates, y and z , are non-dimensionalized with the test section height and width, h .

In general, these figures indicate coherent structures in the flow. For the three velocities, the flow character is nearly independent of velocity. Also, the flow does not appear to be symmetrical. Outside the boundary layer, the axial component increases from top right-hand corner to the lower left-hand corner of the survey region in bay while in bay 7 the flow velocity tends to decrease primarily from right to left or from the wall to the center of the channel. In bay 1, two coherent flow structures exist near the tunnel wall with a significant upward velocity of about +4 %. The maximum value is +4.7 %, or the flow angle is +2.7° relative to the flow at the center. This result is similar to that reported by Blanton and Etter [4].

The area survey for vertical velocity in bay 7 is nearly symmetric and does not include the region near the wall. However, a new flow structure appears in the upper right-hand side, which is upward. The maximum value is +3.7 % or +2.1°.

A summary of the spatial variation in velocity for the 1996 data is presented in Figure 35. These results are at the 95 % confidence limit for the velocities outside the boundary layer. As the figure indicates, the velocity variation is nearly independent of velocity at the center of the channel. The lowest value in axial velocity variation is about 1.1 %, which is higher than reported by Blanton and Etter [4]. The minimum value for the vertical component is 1.6 %. With the exception of the value for the axial velocity at 3 m/s, the values for both the vertical and axial components are lower in bay 7.

Since 1996, more comprehensive measurements of velocity uniformity have been conducted with a 1,600 mm lens. In these measurements, the survey area was 1,000 mm high by 1,550 mm wide (3.3 by 5.1 ft) with a resolution of 50 by 50 mm (2.0 in). The survey area was 17 % of the test section cross-sectional area. The velocity measurement at each position was an average of 1,000 samples. The total number of survey positions was 672, where the number of survey positions outside the boundary layer was typically 650 in comparison to the 140 positions previously described.

Summaries of the more recent results are shown in Figure 36 and Figure 37 for the axial and vertical components, respectively. In this case, the axial and vertical components were measured simultaneously in a single survey. The results for the vertical velocity are similar to previous results with a variation of nominally 2 %. The minimum value was 1.8 % in comparison to 1.6 % from the previous measurements. However, a significant reduction in the variation of axial velocity occurred with a minimum of 0.34 % in comparison to 1.1 % in the earlier results. The variation was systematically lower in bay 4 in comparison to bay 2 with a nominal value of 0.4 %. Bay 4 is the region of the tunnel where most models are installed. Details of the statistics for the velocity measurements outside the boundary layer are summarized in Table 4. In general, the mean values of the velocities outside the boundary layer were slightly higher than the centerline values. The data summarized in Table 4 should be considered benchmark data for future comparisons.

The measurements in 2001 were completed after modifications to the flow management section of the tunnel. A significant amount of debris was removed from the flow management section from failure of the coatings on the turning vanes. Also, structural failures had occurred due to corrosion of the brazing for the flow straighteners. These were repaired, and minor structural changes were made to prevent future failures. Finally, a seeder was installed upstream

of the flow straighteners for PIV (Particle Imaging Velocimetry) measurements. Figure 36 and Figure 37 include data from December 1998 before these changes were implemented. As the figures indicate, no measurable changes in flow are detected. In fact, two other data points are virtually coincident with the 1998 data for the axial velocity at 12 m/s. Operation of the particle seeder at maximum flow capacity does not affect the flow quality.

The contour plots for the data summarized in Table 4, Figure 36, and Figure 37 are shown in Figure 38 through Figure 48. For these contour plots, the spatial coordinates are non-dimensionalized with the channel half-width, $h/2$. The contour plot in Figure 38 from 1998 is near the tunnel entrance at window 1 of bay 2 at 12 m/s. The measurements in this figure were acquired before the major renovation of the flow straighteners and installation of the PIV seeder previously described. Figure 42 shows the data at the same location and velocity after the modifications. The results for the vertical and axial velocity components are very similar to those in Figure 38.

The results in Figure 38 through Figure 43 are for window 1 of bay 2 near the tunnel entrance, while Figure 44 through Figure 48 are for window 1 of bay 4 near the center of the test section. No velocity gradient in the axial component outside the boundary layer appears to occur that was observed in the 1996 measurements. The colors in these figures for the axial component are in increments of 0.005 (0.5 %) for the local mean velocity in comparison to the centerline velocity (U/U_o). Typically, only three colors are observed for bay 2 while bay 4 has only two. The color variation is consistent with the statistics where the velocity variation is about 0.5 % in bay 2 but 0.4 % in bay 4.

The two large coherent structures in vertical velocity near the wall observed in the 1996 data in bay 1 are apparent in both bays 2 and 4 for the more recent data. With the higher resolution for the more recent data, these structures are defined more clearly. The results are independent of velocity. However, the structure nearest the wall is influenced by boundary layer; consequently, systematic differences occur due to the thicker boundary layer in bay 4. A typical peak value in vertical velocity relative to the centerline is about +4 to 5 % or +2.3° to 2.9°.

High quality contour plots of the velocity components, which show coherent structures, are possible due to the long-term temporal velocity stability of the channel. Typically, two hours of run time was required for the 672 positions in the more recent contour plots. In fact, much of the long-term temporal stability data described earlier in this paper was accumulated during the velocity surveys for the contour plots. The tunnel velocity measurements at 3 m/s in Figure 16 are associated with the third entry of Table 4 for the PIV seeder at maximum flowrate. The tunnel entrance velocity data at 12 m/s in Figure 17 corresponds to the contour plot of Figure 47 while the 16 m/s data in Figure 18 is associated with Figure 43. The long-term velocity stability of ± 0.15 % is small in comparison to the spatial variation in velocity, which is ± 0.4 to ± 0.5 %.

During checkout of the tunnel before the HiFoil experiment [11], the coatings on the turning vanes failed. Failure of the coatings was not discovered until the completion of the HiFoil experiment. At the beginning of the HiFoil experiment, velocity uniformity was measured in window 1 of bay 2 on 27 October 1999. The results are summarized in Table 5. As the table indicates, the non-uniformity in the axial velocity outside the boundary layer was about 1 %. This increase in non-uniformity may be attributed to the debris that collected in the flow management section.

Turbulence

Theory

One of the key performance measurements for wind tunnels and water tunnels is the relative turbulence intensity in the test section, u'/U where u' is the rms or standard deviation of the mean velocity, U . Historically, low values of turbulence required careful design of the turbulence management section and the contraction. For low turbulence, a large area ratio for the contraction section was necessary. Typically, water tunnels with high performance have an area ratio of 9 with a symmetric contraction design and stainless steel honeycomb for turbulence management. Examples are the water tunnels at Penn State [13], [14] and NIST [15], [16]. Nagib, et al. [17] have indicated that little is gained in efficiency for a contraction ratio $Cr > 9$ and a non-dimensional length $L/D_i > 1.0$. The resulting turbulence in a high quality tunnel is typically 0.1 %. The characteristics of some representative water tunnels in the USA are listed in Table 6 as follows: California Institute of Technology (CIT) [18], Case Western Reserve University [19] [20] [21], NIST [15] [16], Pennsylvania State University [13], [14], Naval Ocean Systems Center (NOSC) [22], and Southwest Research Institute (SwRI) [23].

Although high contraction ratios have been required for low turbulence levels, good results have been obtained for low contraction ratios. The SSPA Sweden large cavitation tunnel [24] has reported turbulence of 0.15 % at 3.6 m/s (12 ft/s) increasing to 0.19 % at 9 m/s (30 ft/s) for a contraction ratio of 2.76. The data for the SSPA tunnel have been included in Table 6 for comparison.

Tan-atichat [25] had performed an extensive experimental program on the effects of contraction ratio on turbulence for matched cubic axisymmetric contraction sections. His experimental results for the range of contraction ratios of common interest, $6 < Cr < 30$ were summarized by the following equation

$$(u'/U)_e / (u'/U)_i = [1/Cr] \sqrt{(Cr-5)/6} \quad (7)$$

where the subscript "i" is the turbulence at the contraction inlet and "e" for the exit. From measurements at the Penn State tunnel, the inlet turbulence was $1 < (u'/U)_i < 3$ % where 1 % is the more recent value. For $Cr = 9$ and $(u'/U)_i = 0.01$, equation (7) yields 0.09 % for the test section, which is in agreement with the reported values for the Penn State tunnel [14] and NIST tunnel [15], [16]. However, the reported turbulence in the Penn State tunnel [14] for the test section was inferred from measurements of the honeycomb turbulence and was not directly measured. Although equation (7) is not valid for the LCC, it can provide a value, which may reasonably be expected. For $1 < (u'/U)_i < 3$ % and $Cr = 6$, the expected turbulence in the LCC test section is $0.07 < u'/U < 0.2$ %. As stated previously, the design goal was 0.1 %.

Experimental Method

The primary method for the measurement of turbulence in a water tunnel is by hot-film anemometry with a constant temperature anemometer (CTA). The background noise level of an LDA is about 1 %; consequently, an LDA cannot measure the anticipated turbulence of 0.1 %. One of the difficulties with CTA is the low operating temperature required in water. Since changes in water temperature will affect results, temperature corrections must be included in the

calibration. The modified King's law for calibration of a CTA is given by the following equation [26]

$$E_b^2 / (T_s - T_a) = A + BU^n \quad (8)$$

where E_b is the CTA bridge voltage, T_s is the operating temperature of the sensor, T_a is the ambient temperature, U is the velocity, and A , B , and n are calibration constants. Nominally, the value of n depends on the type of sensor. For the traditional King's law for a cylinder, $n = 0.5$. Bonis and van Thinh [26] determined that $n = 0.36$ for a conical sensor in water. By differentiation of equation (8), turbulence may be computed directly from the measured voltages and calibration constants

$$u' / U = 2e' E_b [n(E_b^2 - A\Delta T)] \quad (9)$$

where the prime indicates the rms value and $\Delta T = T_s - T_a$. The calibration constants and relative turbulence intensity may then be calculated from a single set of data.

Since water temperature increases from the energy from the pump, data acquisition is greatly simplified through acquisition of the data in a single set of measurements. That is, calibration data and turbulence data are acquired from the same set of data with equations (8) and (9). This method was previously applied by Park [23]. Additionally, the sensitivity of the bridge voltage for the CTA greatly diminishes with increasing velocity. The maximum value reported in the literature for calibration in water is about 6 m/s (20 ft/s) [15], [26]. The solution at Penn State was to measure the turbulence in the plenum chamber and extrapolate the results by theory to the test section [13], [14].

For direct measurements of turbulence in the test section, a head-form fixture attached to a submarine strut was modified to accept a TSI probe support (1159AJ) and conical film probe (1230W). The outer diameter of the adapter was 50.8 mm (2.0 inches). The installation on the strut at the test-top stand is shown in the photograph of Figure 49, while operation of the probe with the LDA is presented in Figure 50. The calibration velocity for the hot-film in equation (8) was provided by the LDA located 2 mm upstream of the conical tip as indicated in Figure 50. The CTA was a TSI IFA 300, which had been modified to provide proper frequency response of the conical film and probe support with a 4.6 m (15 ft) cable for operation in water. Additionally, the tunnel water was deaerated to 10 % saturation of oxygen for prevention of bubble problems on the probe.

Experimental Results

The reference velocity for the hot-film calibration was the LDA. The inflow to the hot-film probe was characterized by measurements 2 mm upstream of the probe tip. The results within a non-dimensional radius of 6 probe fixture radii are presented in Figure 51 for the vertical and axial velocity components for 15 m/s. The vertical and axial velocity components are referenced to a measurement 1 m (3.3 ft) from the centerline. As the figure indicates, the local velocity ratio is very nearly one. The most significant feature is the downward velocity below the centerline. The minimum measured value was -2.5 % or -1.4° for three tunnel velocity conditions of 5, 10, and 15 m/s (16, 33, and 49 ft/s).

High-resolution measurements were also completed in a small region at the probe tip with a maximum non-dimensional radius of 0.2. This radius is the same order of magnitude as the

length of the LDA probe volume from Table 2, which was about 0.26 of the probe fixture radius. The purpose of this measurement was to resolve the effect of the probe on the flowfield nearer the probe tip. The minimum axial velocity near the probe tip was measured as 0.97 of the reference velocity or 3 % below the reference for three tunnel velocities (5, 10, and 15 m/s). Contour plots for 5 and 15 m/s are shown in Figure 52 for comparison. The region shown in this figure for 15 m/s is overlaid on the contour plot in Figure 51.

The test section turbulence was measured by both a TSI IFA-300 and Dantec StreamLine CTA. The frequency response of the TSI CTA is fixed by factory settings and was adjusted at the factory for the probe and probe support combination in water. The frequency response of the Dantec CTA was adjustable through software. The measured values were 96 kHz for the TSI CTA and 140 kHz for the Dantec unit. The cutoff frequency was computed with the following formula from [26]

$$f_c = 1/(1.3\tau) \quad (10)$$

where τ is the time constant as determined from the response of the bridge output voltage to an internal square-wave generator.

The nominal operating temperatures for both CTAs was 67 °C. The over-heat ratios were 0.08 for the TSI unit and 0.09 for the Dantec CTA. The overheat ratio, a , was computed from the resistance settings for the CTAs

$$a = (R_s - R_a) / R_a \quad (11)$$

where R is the bridge resistance and the subscripts are the same as in equation (8).

The calibration constants in equation (8) were determined from a commercial computer code, TableCurve2D. However, TableCurve2D yielded a better curve fit given by the following equation

$$(E_b^2 / \Delta T)^2 = A + B \ln U \quad (12)$$

By differentiation, the relative turbulence intensity is then

$$u' / U = 4E_b^3 e'_b / (B \Delta T^2) \quad (13)$$

In this case, only the single calibration constant, B , is required for computation of the relative turbulence intensity. The results are presented in Figure 53.

As the figure indicates, good agreement in the turbulence data was obtained for the two CTAs. The turbulence had a maximum of about 0.49 % at 2 m/s (6.6 ft/s) and a minimum of 0.17 % at 0.5 m/s (1.6 ft/s). A gradual increase occurred in turbulence with increasing velocity above 4 m/s (13 ft/s) from 0.22 % to 0.41 % at 15 m/s (49 ft/s). The trend above 2 m/s (6.6 ft/s) is similar to that reported by Robbins [14].

Also as the figure shows, the background noise level of the LDA is significantly larger than obtained by CTA. The minimum noise level was 0.77 %, which occurred at the highest tunnel velocity, where the value measured by CTA was 0.41 % or approximately half of the LDA value. During the LCC OWD experiment [12], the inlet velocity to the propeller was measured by LDA. The relative turbulence intensity in the freestream was measured as 0.54 % at 12.79 m/s,

which is one of the lowest values measured by the LDA system for the LCC. In comparison, the hot-film measured 0.31 % at 12.50 m/s as shown in Figure 53.

Additional details of the measurements are summarized in Table 7 for the TSI CTA and Table 8 for the Dantec CTA. These tables include the number of samples, sample rates, and low-pass filter settings for the anemometers. Most of the averaging times for IFA 300 and Dantec CTA were 210 s and 175 s, respectively.

Velocity spectra for the IFA 300 were computed with the TSI Thermal Pro software. The data were averaged in 8192 sample record lengths. The frequency resolution is listed in Table 7 where the values are between 0.244 and 2.44 Hz with the resolution increasing with tunnel velocity and sample rate. Examples of the spectra are presented in Figure 54 through Figure 58 for velocities from 0.5 to 14.5 m/s. The frequency is non-dimensionalized with the measured cutoff frequency of the turbulence, that is, the frequency where the energy from the turbulence runs into the noise floor of the instrument. In most cases, the frequency at the minimum magnitude of spectrum was selected.

The cutoff frequencies for all of the computed spectra are summarized in Figure 59 as a function of the mean velocity as measured by LDA. These measurements indicate that the filter settings for the IFA-300 were overly conservative and were used in the selection of the filter low-pass frequency settings for subsequent measurements with the Dantec CTA. Since the turbulence intensities are very similar for the two CTAs, the filter settings did not have a significant effect on the results.

Unfortunately, the TSI Thermal Pro software does not compute the magnitude of the spectra correctly for large sample sizes. The integrated value of the spectra should yield the variance. The integrated results under-predict the turbulence intensity by a few percent at the lower velocities. At 14.5 m/s, the value is low by 45 %. The magnitude of the error seems to increase with sample size.

In any case, the spectra are quite smooth with the exception of instrument noise spikes at the higher frequencies. For comparison, the spectra include the highest and lowest velocities measured (0.5 and 14.5 m/s), the maximum turbulence intensity at 2 m/s, and the minimum in the turbulence curve at 4 m/s. The mid-range spectrum at nominally 9 m/s in Figure 57 was selected because an audible resonant frequency can be heard in the tunnel at this speed. No resonant frequency spikes are observed in this figure. The pump for the tunnel is a 7-bladed propeller. The blade frequency at this tunnel velocity was 3.0 Hz in comparison to the frequency resolution of 1.2 Hz. The blade-passage frequencies for the various tunnel speeds are listed in Table 7 with the frequency resolution of the spectra.

Conclusions

Comprehensive experimental results and data analysis have been presented on the hydrodynamic performance of the William B. Morgan Large Cavitation Channel, the world's largest water tunnel. The data from this research represents several years of accumulation of data. The results demonstrate a very high quality of hydrodynamic performance and are probably the most comprehensive data ever presented for any water flow test facility. For the most part, performance equals or exceeds design specifications. The key performance characteristics are as follows:

- **Temporal Velocity Stability.** For a single point measurement for run times on the order of two hours or more, the velocity variation is within ± 0.15 % at the 95 % confidence level for all test section velocities from 0.5 to 18 m/s (1.6 to 59 ft/s) as shown in Figure 10. The temporal stability is new data for the LCC and is probably not reported for any other flow facility.
- **Spatial Velocity Uniformity.** Most recent velocity measurements indicate a spatial variation in axial velocity of ± 0.34 to ± 0.62 % at the 95 % confidence level for test section velocities of 3 to 16 m/s (9.8 to 52 ft/s) from Figure 36 and Table 4. The values are systematically lower near the middle of the test section in bay 4 and higher at the entrance. These values are also systematically lower than reported in earlier measurements by Blanton and Etter [4]. The newer data is with smaller spatial resolution. Spatial uniformity data are not available in the open literature for any other flow facility.
- **Turbulence.** Turbulence or more specifically relative turbulence intensity is a commonly quoted performance characteristic for water tunnels and wind tunnels. From Figure 53, the measured values are between 0.2 and 0.5 % depending upon velocity. These values are higher than the 0.1 % design goal, but the higher measured values are probably the result of the asymmetric design and the low contraction ratio of 6. For tunnels with contraction ratios of 9 or greater, the measured turbulence intensity is 0.1 % for a high-quality water tunnel. The results for the LCC are compared to other U. S. water tunnels and the SSPA large cavitation tunnel in Sweden in Table 6.

Results are documented on detailed procedures for the calibration of the LDA and related uncertainty. The LDA is calibrated with a rotating disk. The uncertainty in velocity is dependent on velocity, but the variation in velocity units is small. The analysis indicates that the uncertainty can be reduced to less than ± 18 mm/s (0.06 ft/s) at the 95 % confidence level with a calibration radius of 50 mm (Figure 5). The processor calibration contributes an additional 10 mm/s in uncertainty (Figure 6), which results in a total uncertainty in calibration of less than 21 mm/s (0.07 ft/s).

The primary contributor to velocity uncertainty is the manufacturer's specification on the rotational rate of the disk. The low data scatter in the processor calibration indicates that further improvement is possible through direct calibration of the rotational rate of the disk. An adaptation of the method by Bean and Hall [7] should be implemented. Direct calibration is necessary to provide NIST traceability of the LDA measurements.

The long-term temporal velocity stability and tunnel acceleration have been described. In addition to quantifying performance, this data also provides guidelines for tunnel operation. The following are preliminary guidelines:

- **High Speed.** For velocities of 5 m/s (16 ft/s) and greater, 5 minutes are required for speed stability. Tunnel stability is determined by the operators from tunnel pressure readings and velocity readings based on dynamic pressure.
- **Low Speed.** For velocities below 5 m/s, 15 to 20 minutes are necessary for speed stability. At the lower speeds, the tunnel operators have no indication of velocity due to the low dynamic pressure. Velocity stability can only be determined by an LDA measurement.

- **No Flow.** No flow can only be determined by an LDA measurement. Flow is considered to be zero when the LDA reads a magnitude less than 10 mm/s (0.39 inches/s) for an unpowered model. For a powered model, the propeller acts as a pump; consequently, the velocity will never be zero. In both cases, approximately 30 minutes are required for velocity stability.
- **Acceleration.** The tunnel decelerates faster than it accelerates. Speed stability is attained sooner when the speed is changed from a higher velocity to a lower one.

Specific tests may vary from these guidelines. Speed stability should always be determined with multiple LDA measurements with 2 to 5 minute interval, until the velocity variation is within $\pm 0.15\%$ of the measurement.

The tunnel velocity is set by rotational speed of the pump and then measured by LDA. At pump speeds below 7 rpm or approximately 2 m/s (6.6 ft/s), the relation between rpm and flow velocity is linear, while above 7 rpm the velocity has a power-law relation in Figure 20 with an exponent of about 1.04. From the data in Figure 20, tunnel speed can be set precisely by pump speed in one or two iterations with a nominal linear slope value of 0.32 m/s/rpm.

As shown in Figure 21, a model propeller can have a significant effect on tunnel velocity as determined by the pump-speed set point. In fact for a pump speed of zero, the tunnel velocity will be non-zero with a powered model. As stated previously, 30 minutes may be required for tunnel speed stability. To date, tunnel velocity at no flow with a powered model has not been acquired, but such measurements should be recorded in the future. One exception is the LCC OWD test [12] where the tunnel velocity was measured as 0.435 m/s (1.4 ft/s) at a model propeller speed of 660 rpm and zero pump speed. Approximately, 20 minutes were necessary for a stable velocity measurement.

The deceleration measurement for the submarine crashback experiment in Figure 27 provides an indication for a potential method for a significant reduction in time for no flow. The tunnel pump could be run in reverse to slow the tunnel velocity faster. However, an operational sequence would have to be developed empirically for an optimal time to no flow.

As stated previously, the uniformity results in Table 4 can be applied as benchmark data for future evaluation of the tunnel flow. The higher results from the HiFoil experiment demonstrate that axial velocity variation on the order of 1 % is an indication of blockage of the flow management section by debris. The long-term velocity stability at 18 m/s (59 ft/s) during HiFoil in Figure 10 is higher than other recent measurements and may also be caused by flow blockage in the flow management section. The higher variation in the 1996 uniformity measurements in comparison to those reported by Blanton and Etter [4] may also be such an indication. Velocity uniformity measurements can be a useful tool in the identification of a maintenance problem with the flow management section.

The variation of the vertical velocity component has consistently been the same at about 2 % as indicated by a comparison of Table 4 and Table 5. All of the contour plots indicate two large organized structures in the vertical velocity component near the tunnel wall of $+4\%$ or $+2.3^\circ$. Since these structures have been unaffected by debris in the flow management section, they are likely the result of the design of the asymmetric contraction section or some other design feature. The three-dimensional flow structures in the test section should be characterized with the recently developed stereo PIV (Particle Imaging Velocimetry) system.

The measured turbulence in the test section appears to be consistent with values reported for other facilities. The results from independent measurements with CTAs from two different manufacturers are in agreement. As another verification, the turbulence should also be measured in the plenum just upstream from the contraction for comparison with the results from Penn State [13], [14]. The turbulence in the plenum is expected to be between 1 and 3 %. Recent measurements with the LCC LDA with lower pmt voltage settings indicate that the LDA background noise can be on the order of 0.5 %. Consequently, measurement of the turbulence in the plenum is possible by LDA. Window ports are available for the measurement.

In summary, the flow measurements reported here demonstrate that the LCC is a high-quality world-class facility. The results should be a useful guide for future experiments at the LCC.

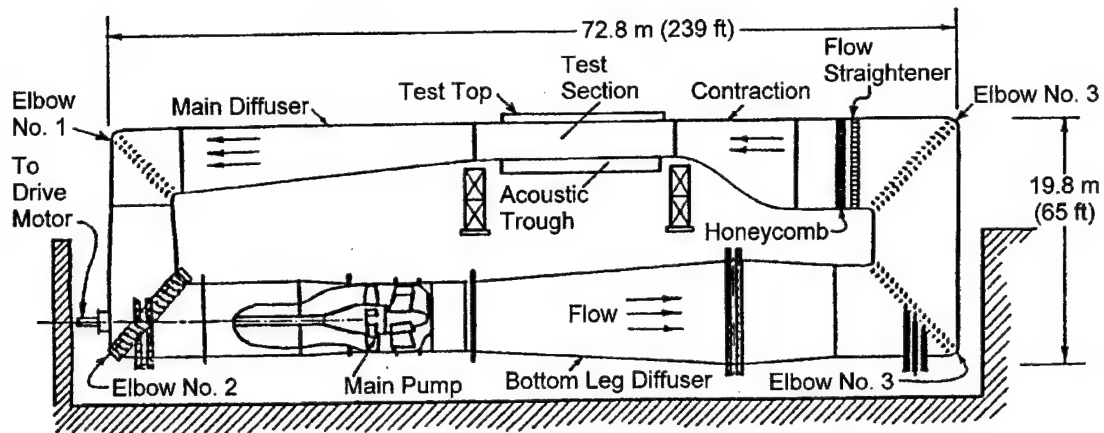


Figure 1. Schematic Drawing of the LCC [1]

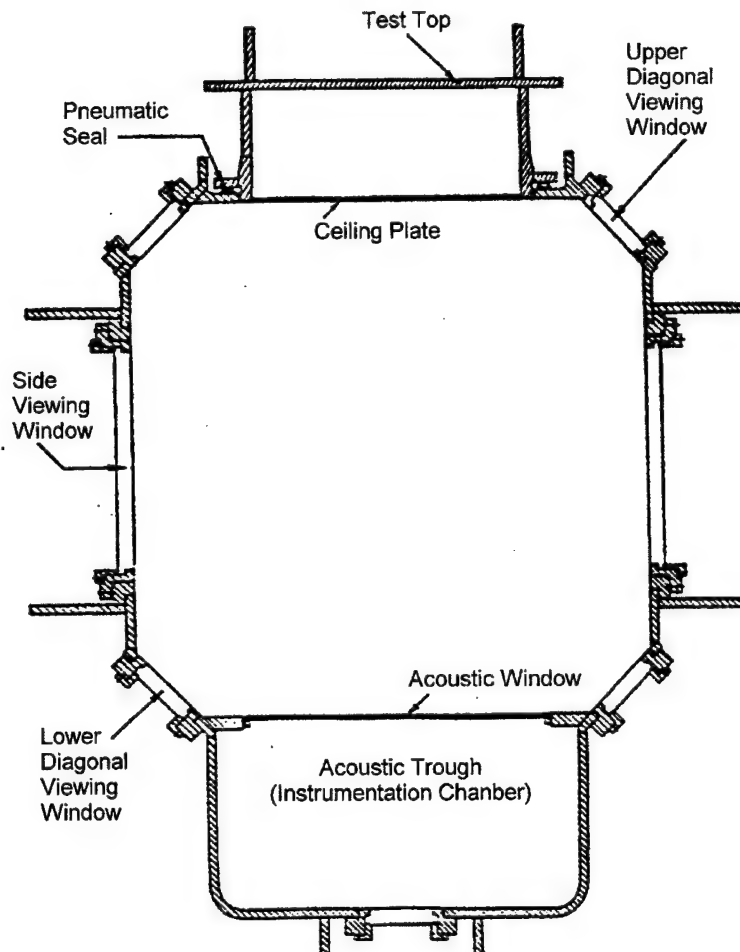


Figure 2. LCC Test Section Cross-Section [1]

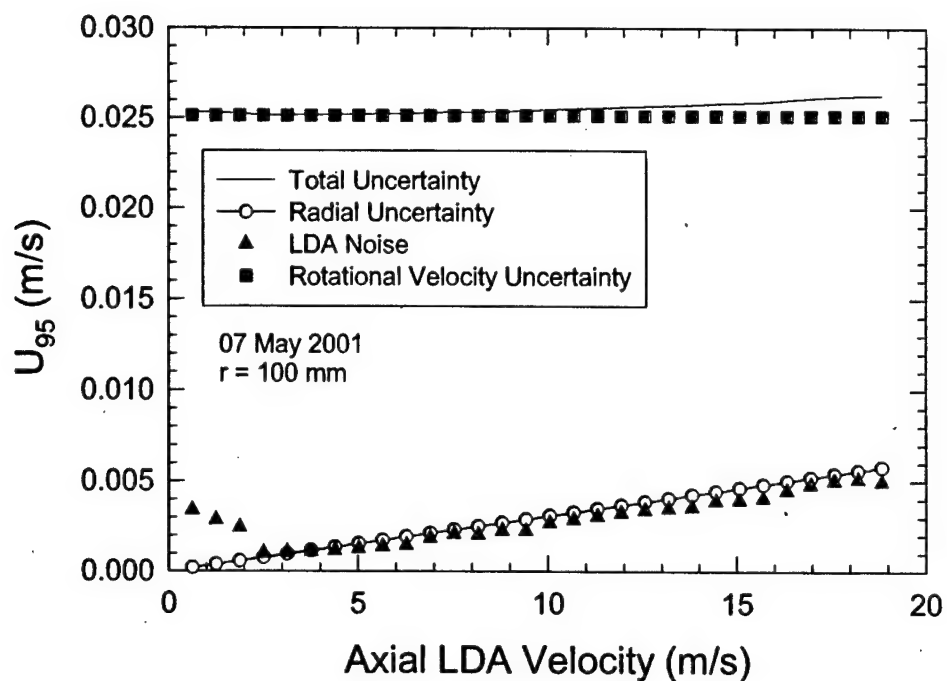


Figure 3. Uncertainty Estimates in LDA Calibration from Rotating Disk at 100 mm Radius

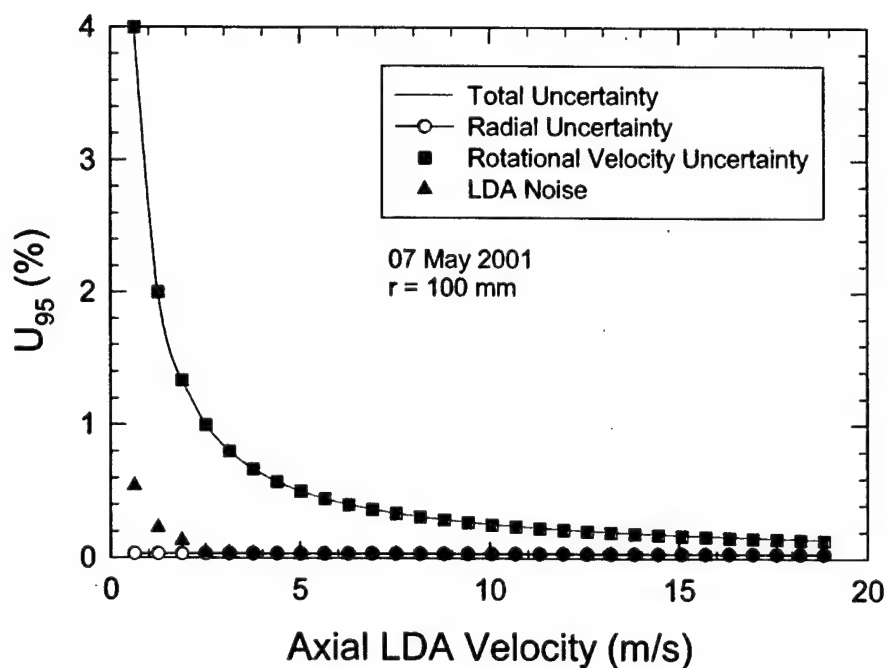


Figure 4. Relative Uncertainty in LDA Calibration from Rotating Disk

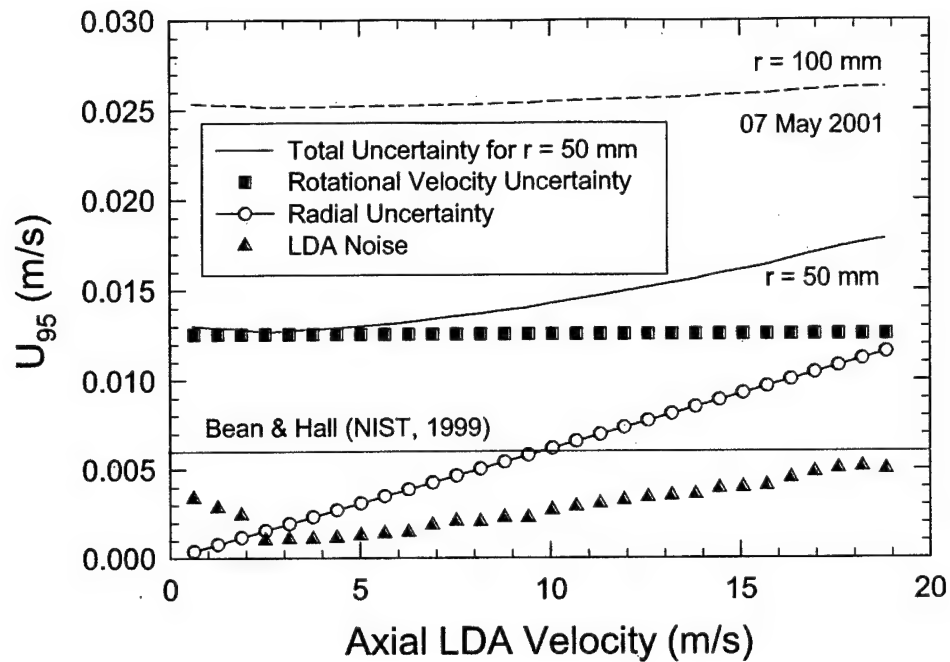


Figure 5. Uncertainty in LDA Calibration from Rotating Disk at 50 mm Radius

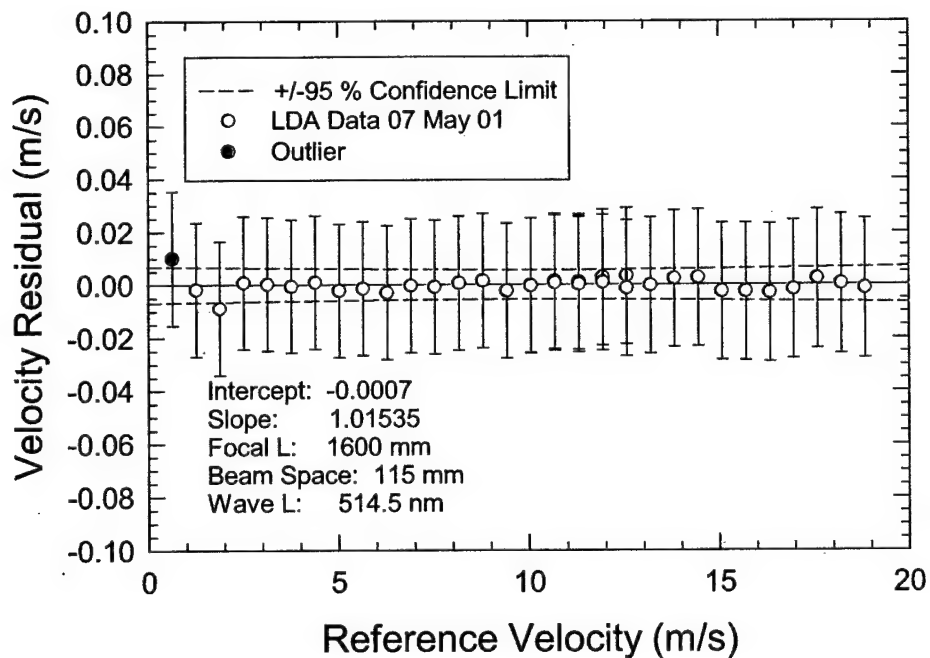


Figure 6. Residual Plot for Calibration of Axial Velocity Component

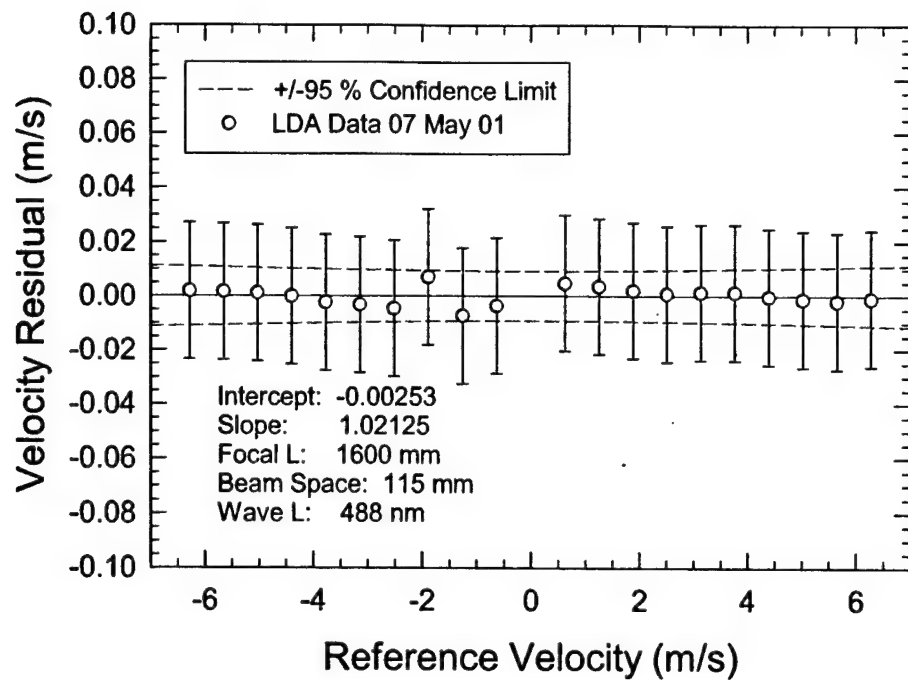


Figure 7. Residual Plot for Calibration of Vertical Velocity Component

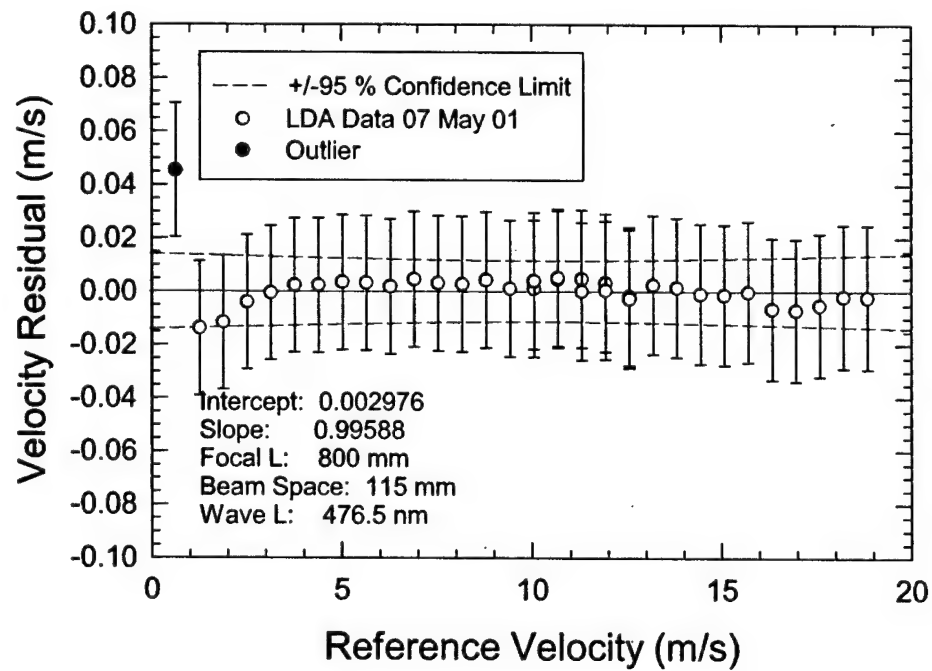


Figure 8. Residual Plot for Calibration of Tunnel Velocity

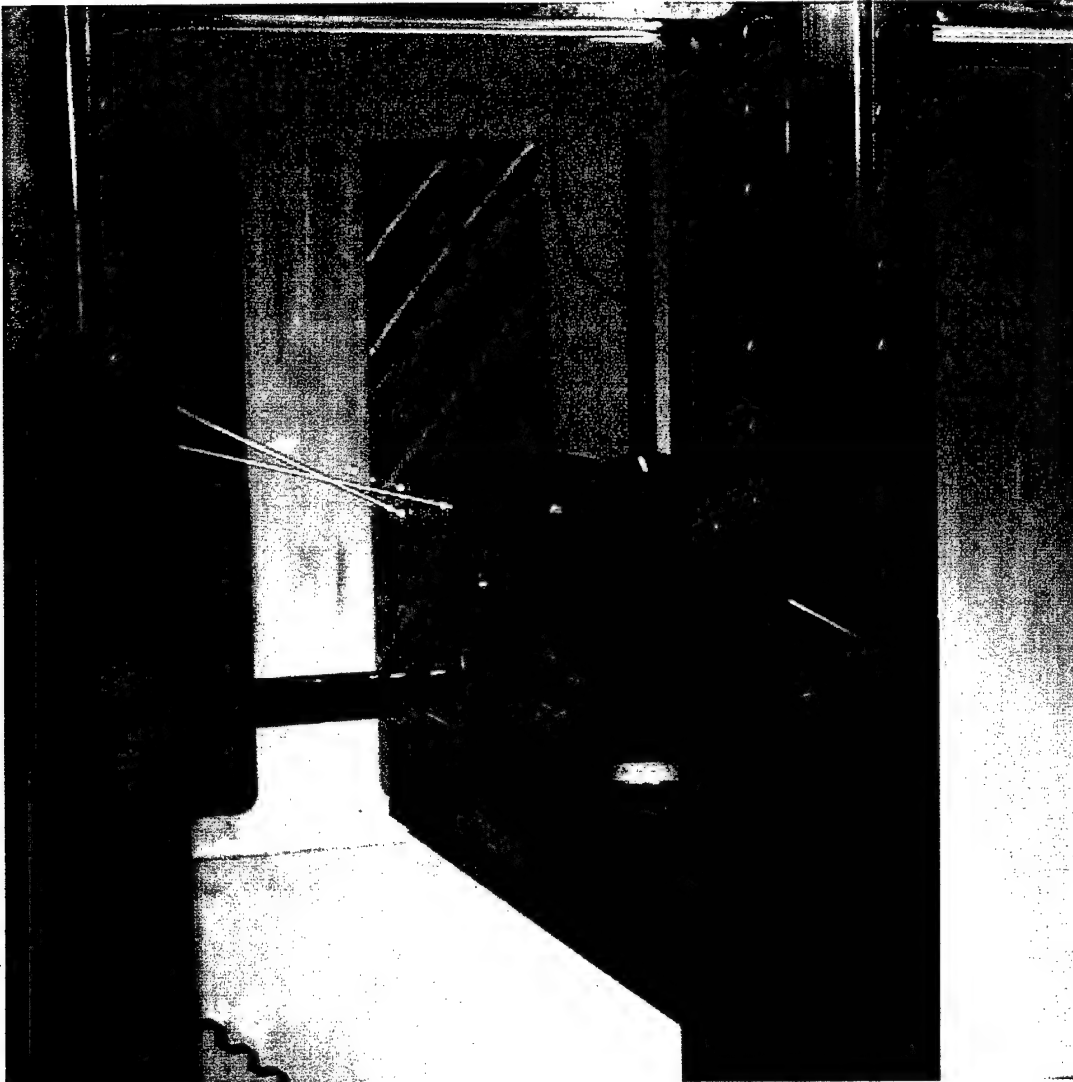


Figure 9. Fiber Optic Probe Installation for Tunnel Velocity Measurement

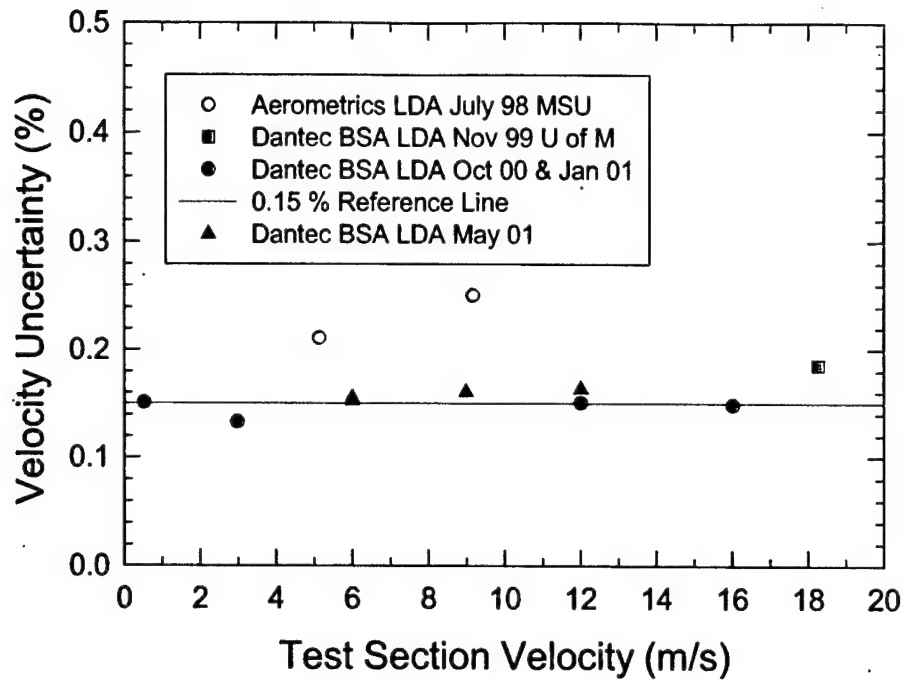


Figure 10. Long-Term Temporal Stability of LCC Test Section Velocity

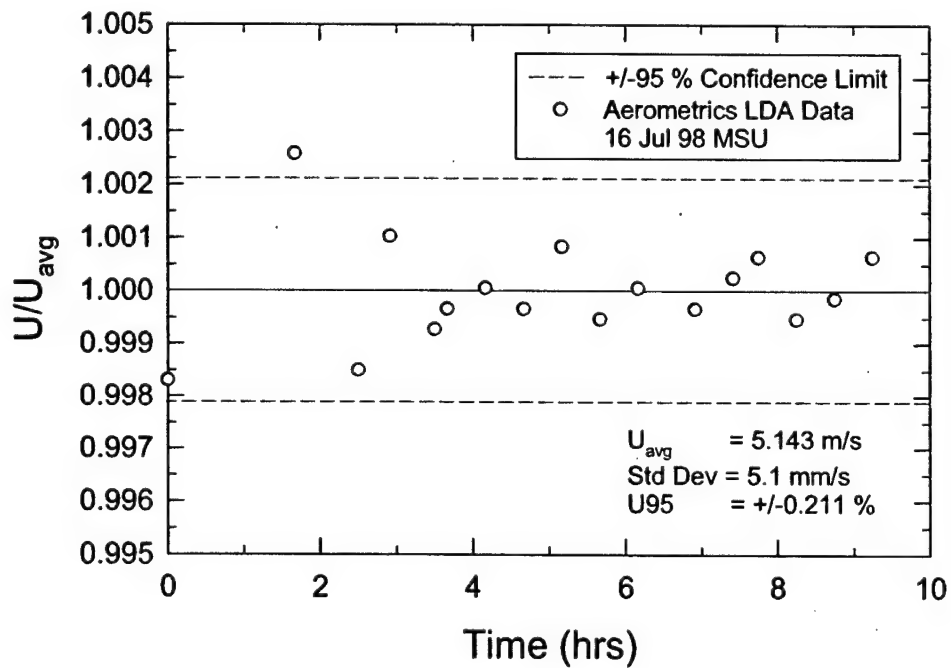


Figure 11. Time Series of Test Section Velocity for Submarine Model at 5 m/s

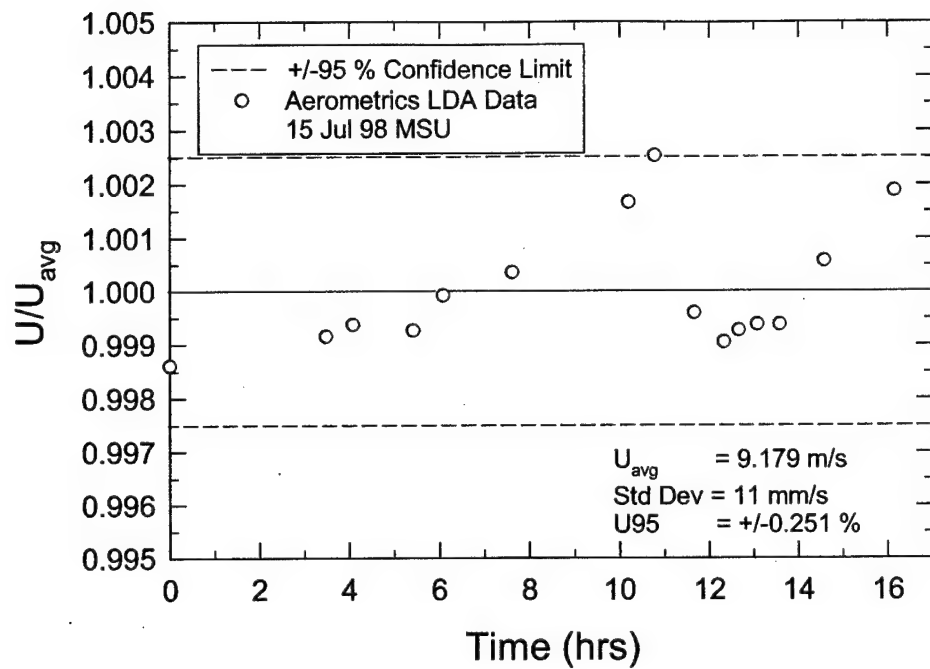


Figure 12. Time Series of Test Section Velocity for Submarine Model at 9 m/s

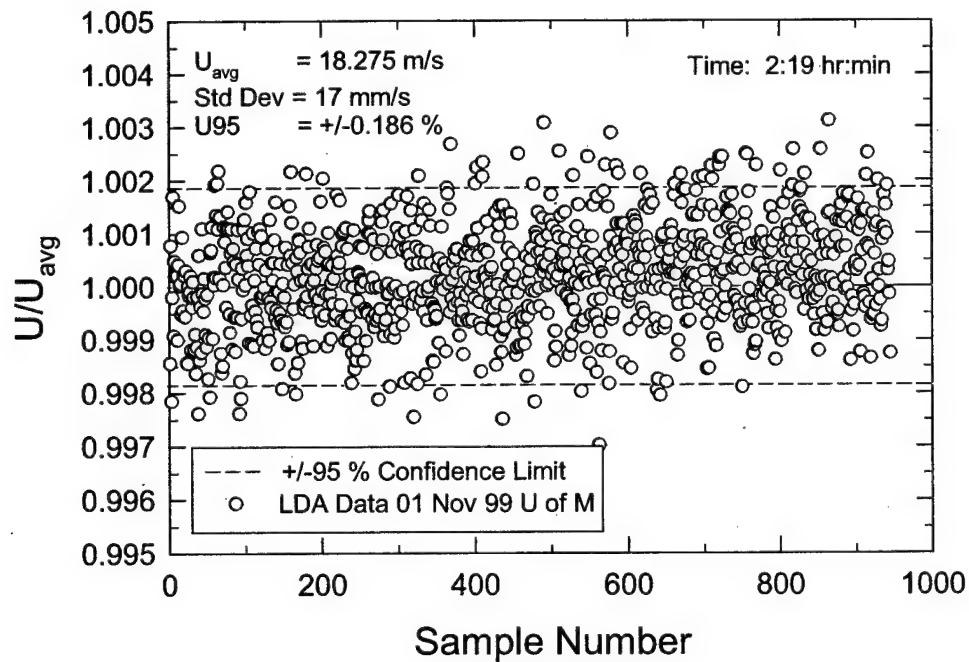


Figure 13. Time Series of Test Section Velocity for Hydrofoil Model at 18 m/s

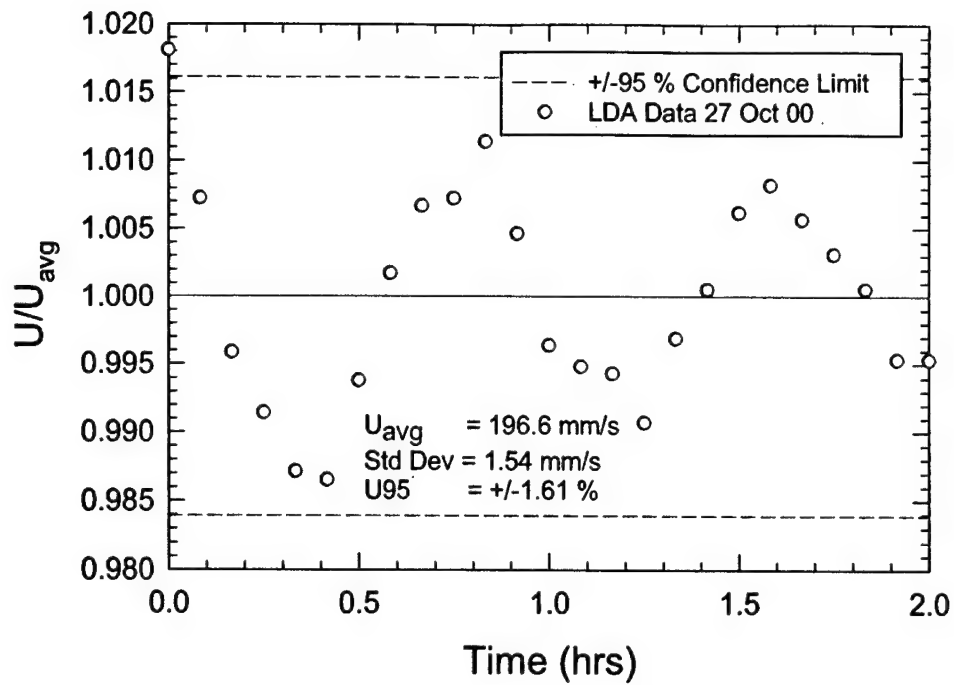


Figure 14. Time Series of Empty Test Section at 0.2 m/s

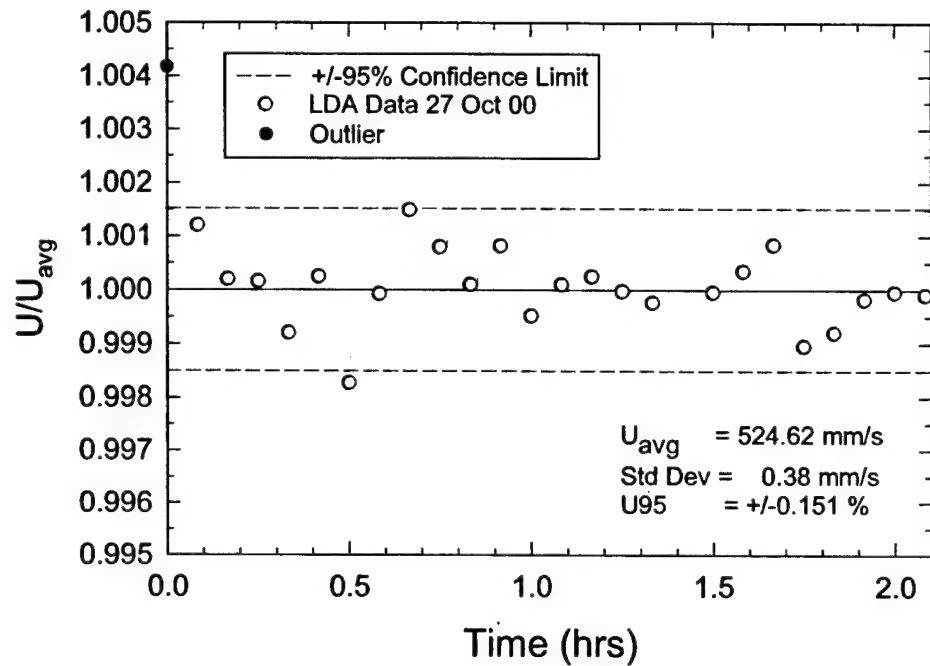


Figure 15. Time Series of Empty Test Section at 0.5 m/s

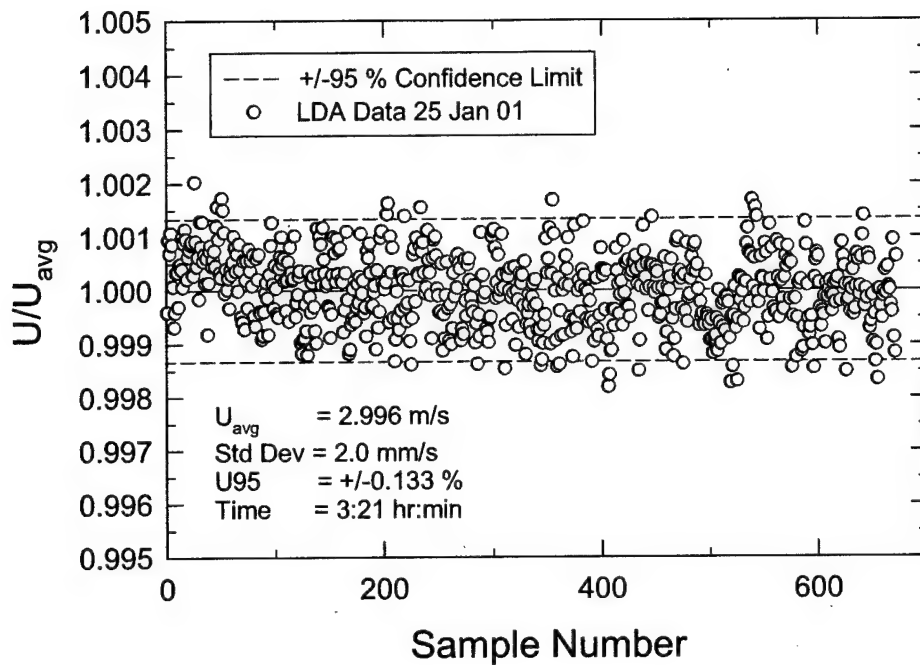


Figure 16. Time Series of Empty Test Section at 3.0 m/s

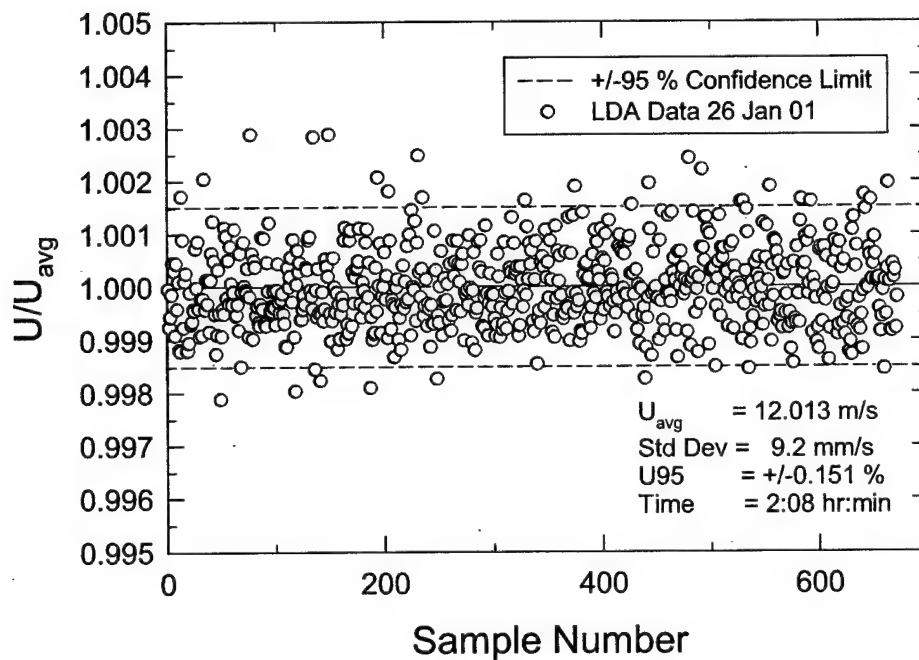


Figure 17. Time Series of Empty Test Section at 12.0 m/s

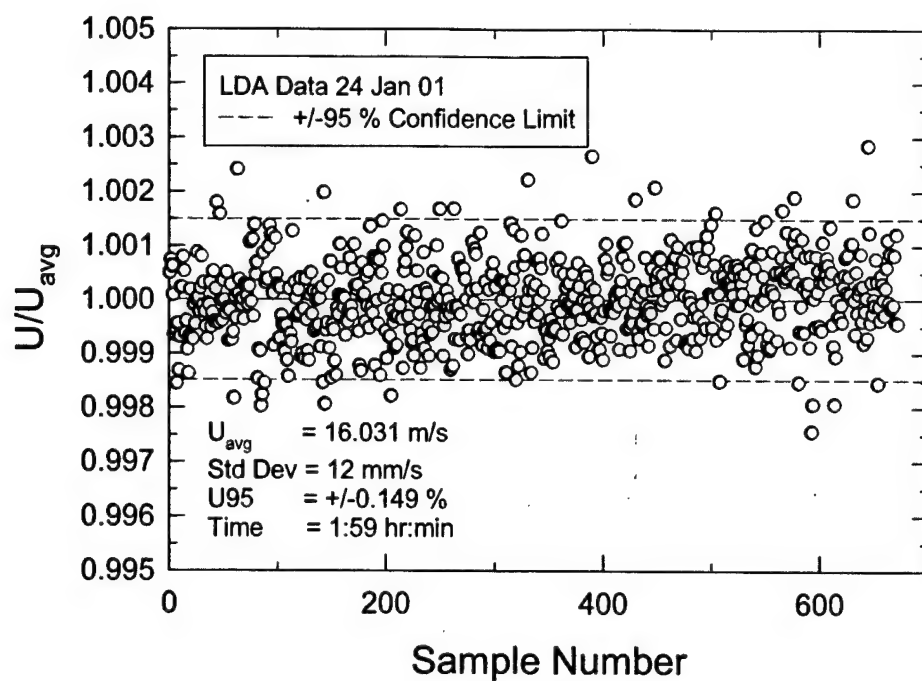
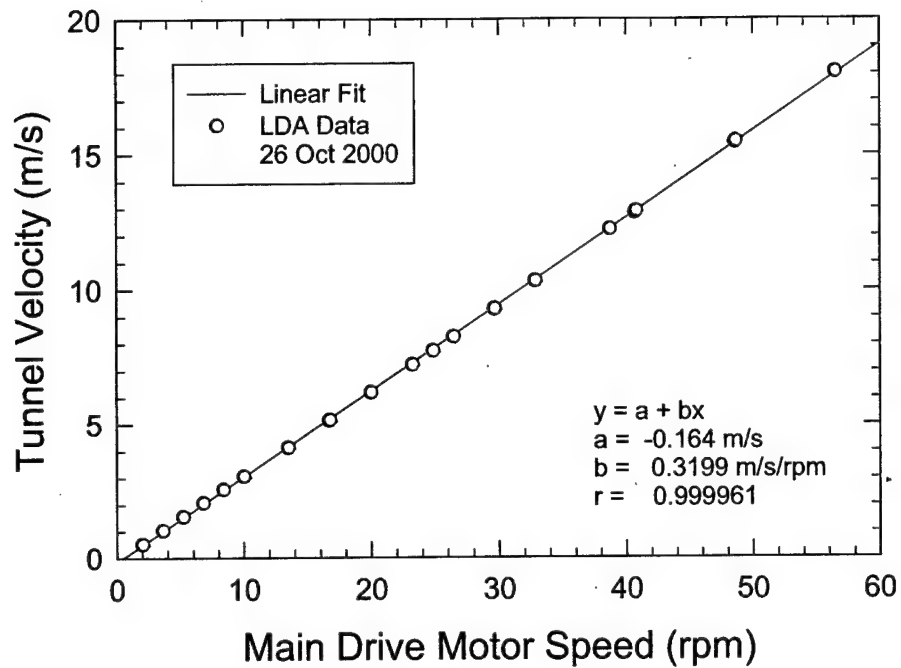
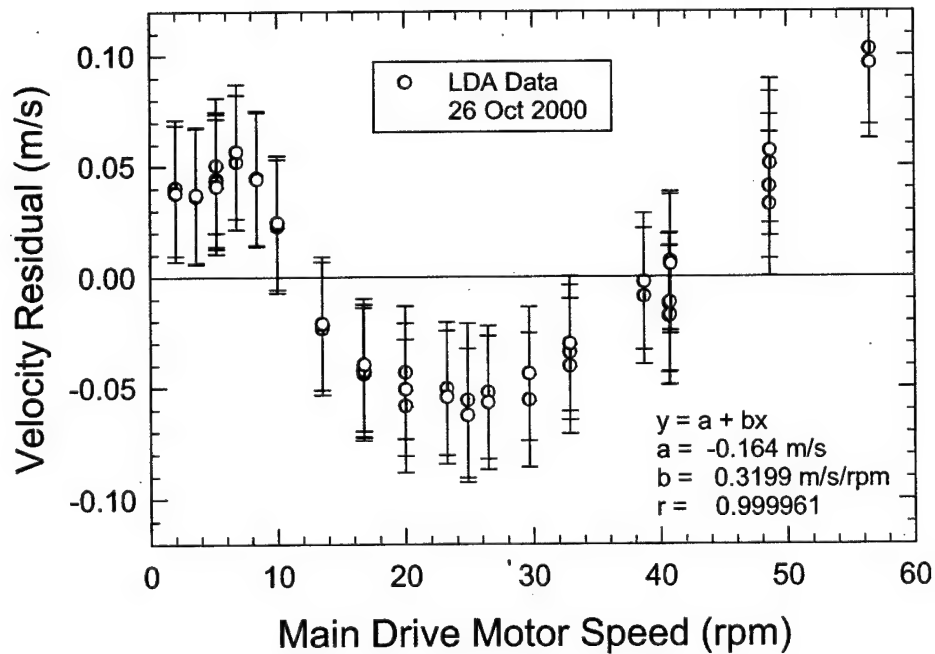


Figure 18. Time Series of Empty Test Section at 16.0 m/s



a. Linear Fit



b. Residuals

Figure 19. Tunnel Velocity from Main Pump Speed for Linear Curve Fit

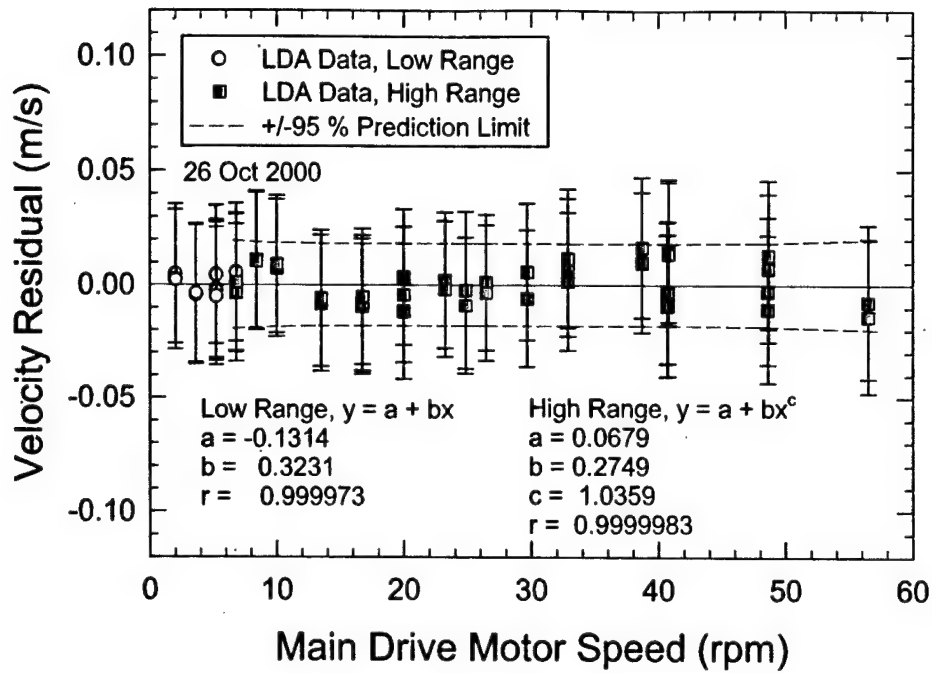


Figure 20. Tunnel Velocity Residuals from Main Pump Speed for Power-Law Fit

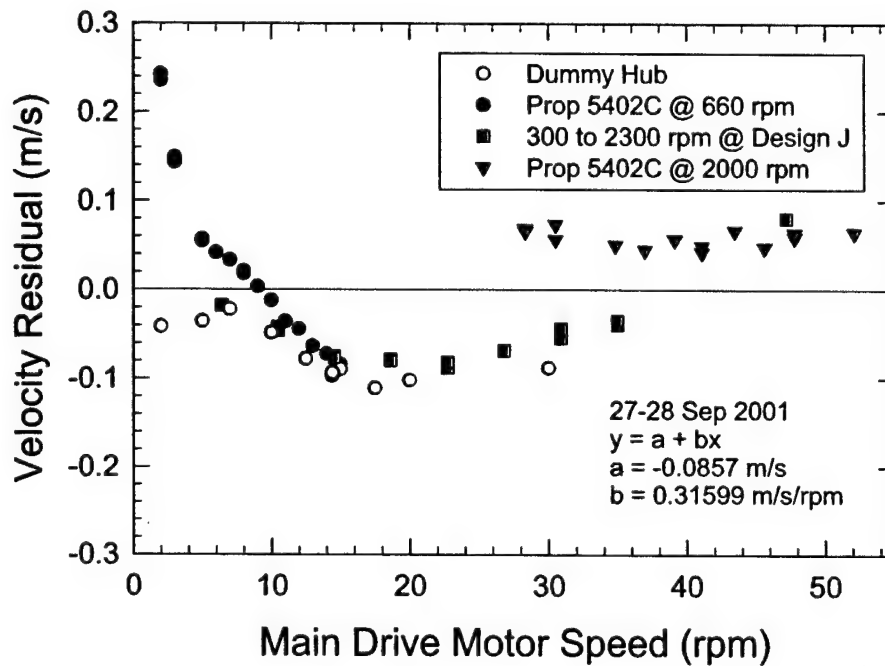


Figure 21. Velocity Residuals for LCC Open Water Dynamometer [12]

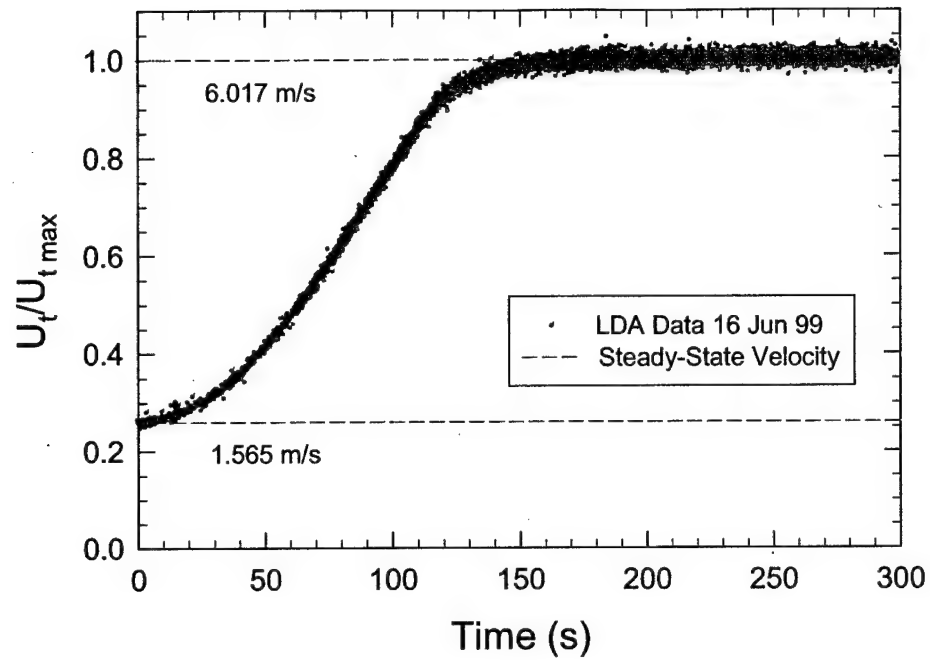


Figure 22. Test Section Acceleration from 1.6 to 6 m/s for NUWC Towed Array

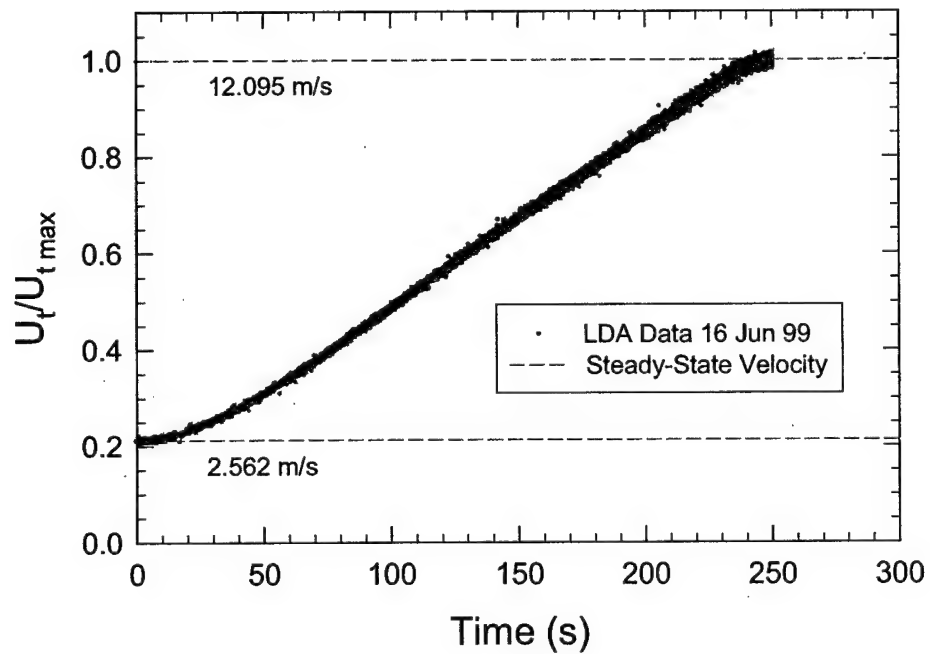


Figure 23. Test Section Acceleration from 2.5 to 12 m/s for NUWC Towed Array

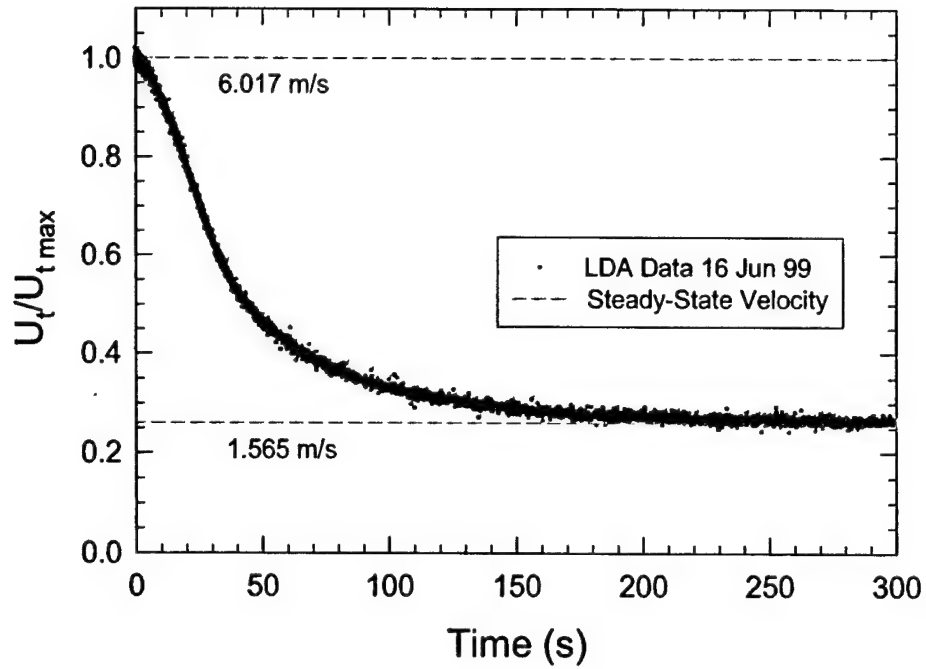


Figure 24. Test Section Deceleration from 6 to 1.6 m/s for NUWC Towed Array

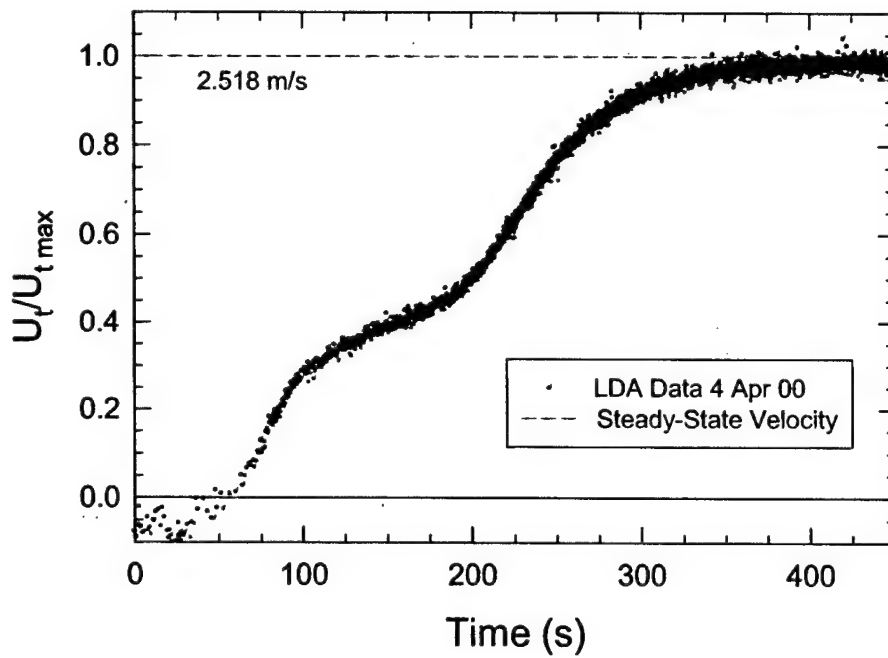


Figure 25. Test Section Acceleration for Submarine Crashback at -600 rpm

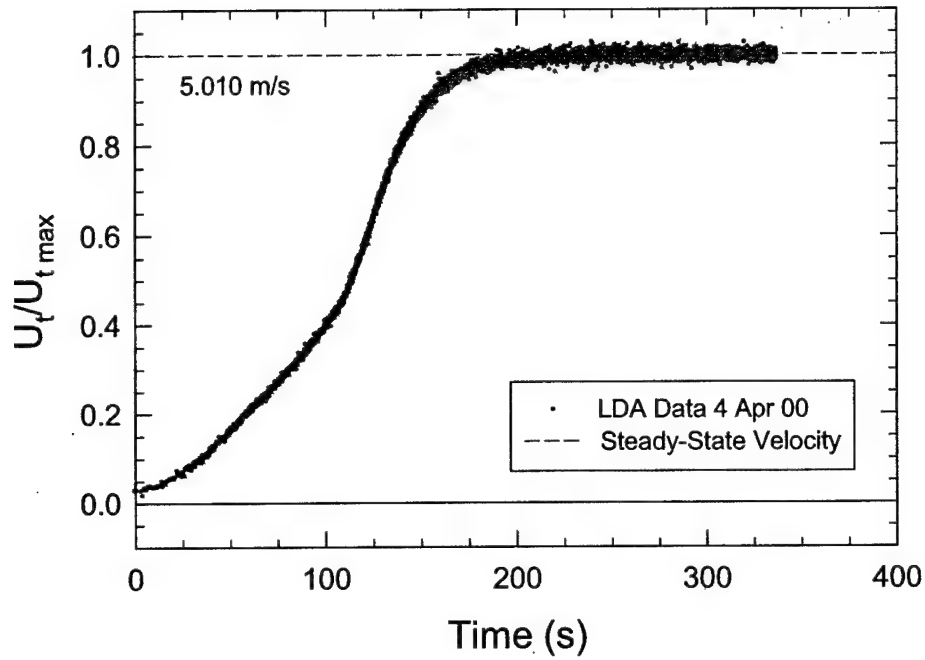


Figure 26. Test Section Acceleration for Submarine Crashback at -200 rpm

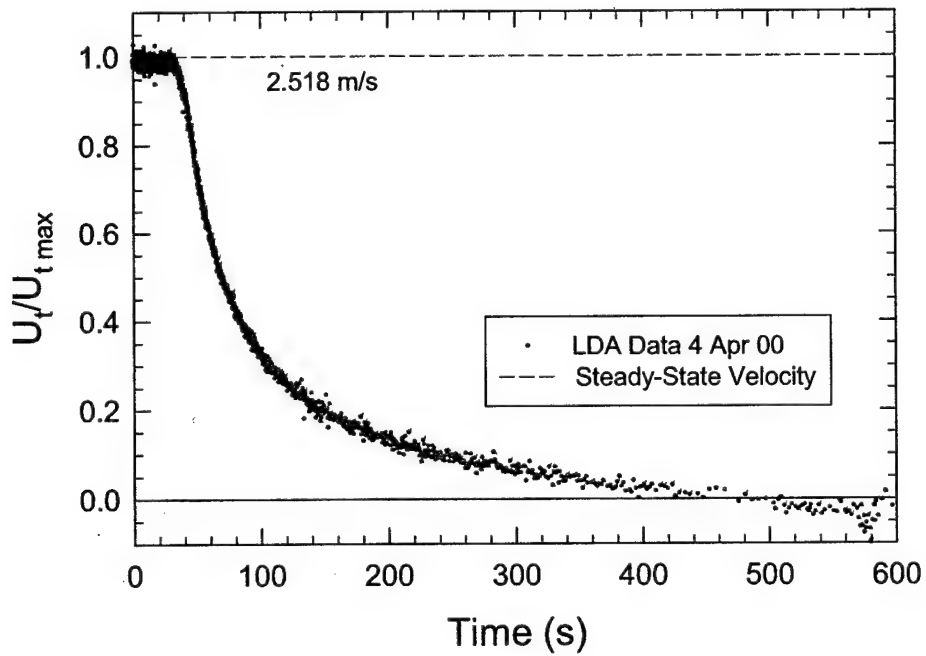


Figure 27. Test Section Deceleration for Submarine Crashback at -600 rpm

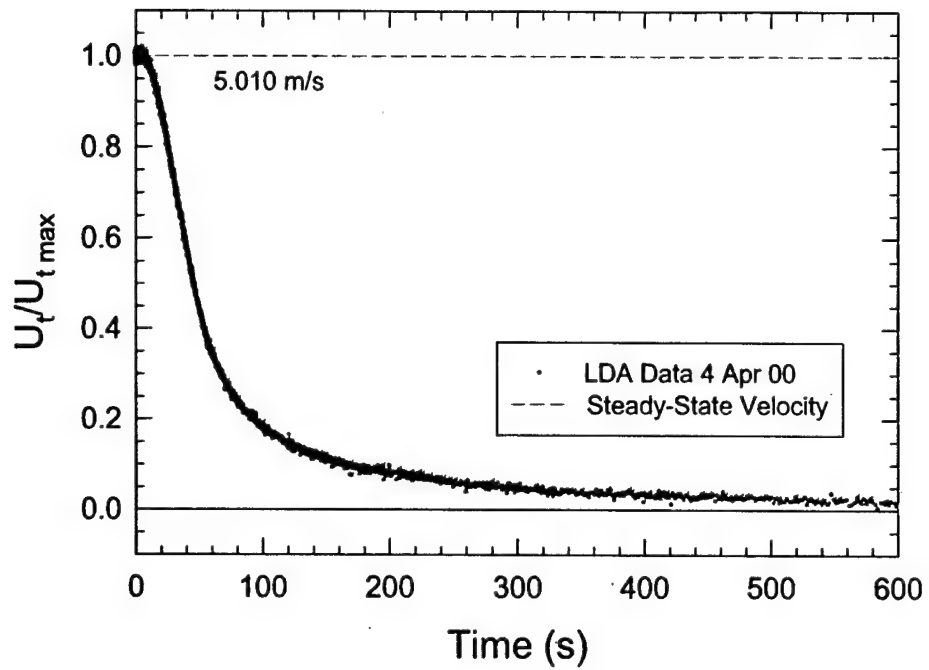
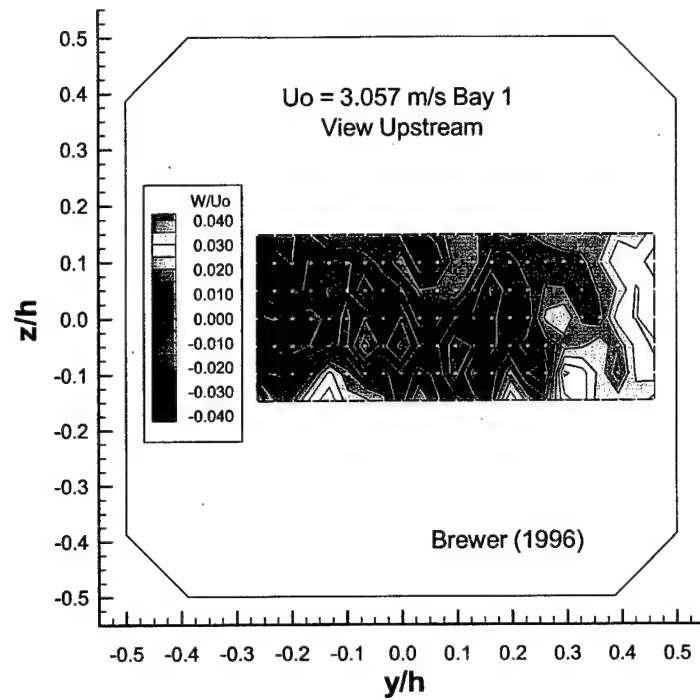
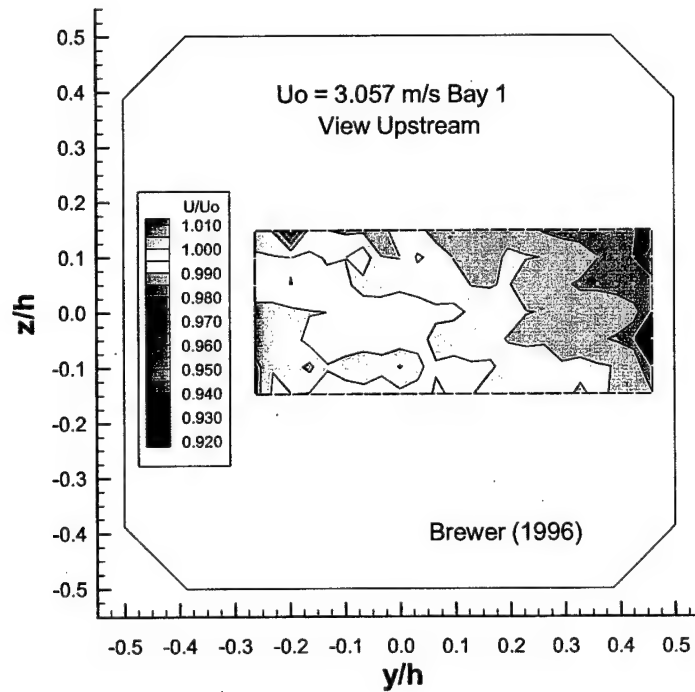


Figure 28. Test Section Deceleration for Submarine Crashback at -200 rpm

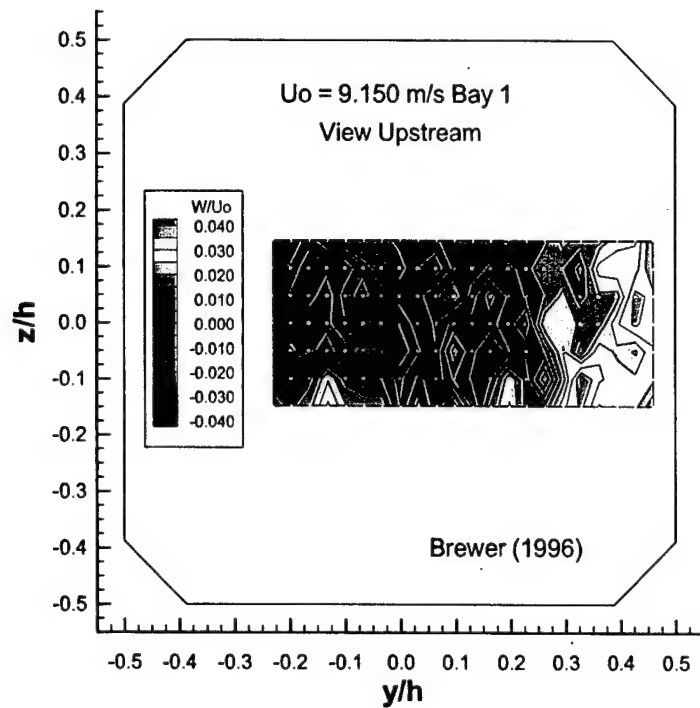


(a) Vertical Velocity Component

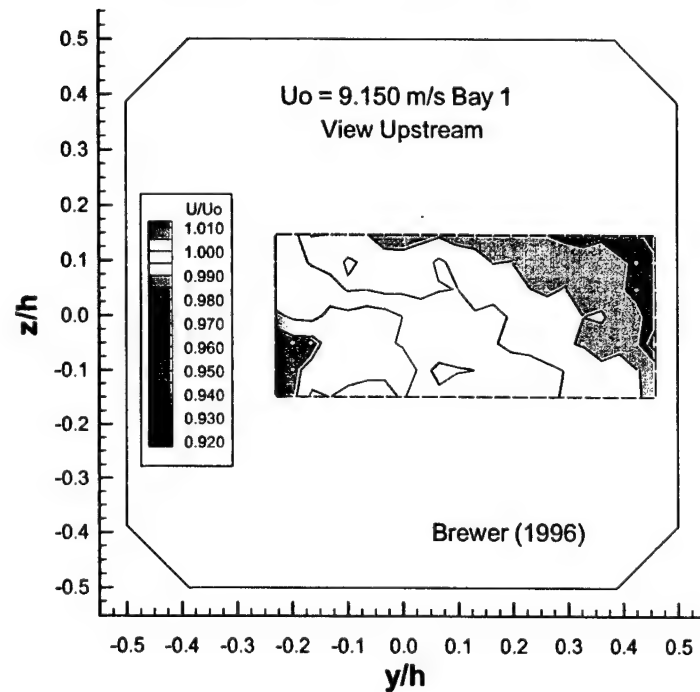


(b) Axial Velocity Component

Figure 29. Contour Plots for an Empty Test Section in Bay 1 at 3.1 m/s

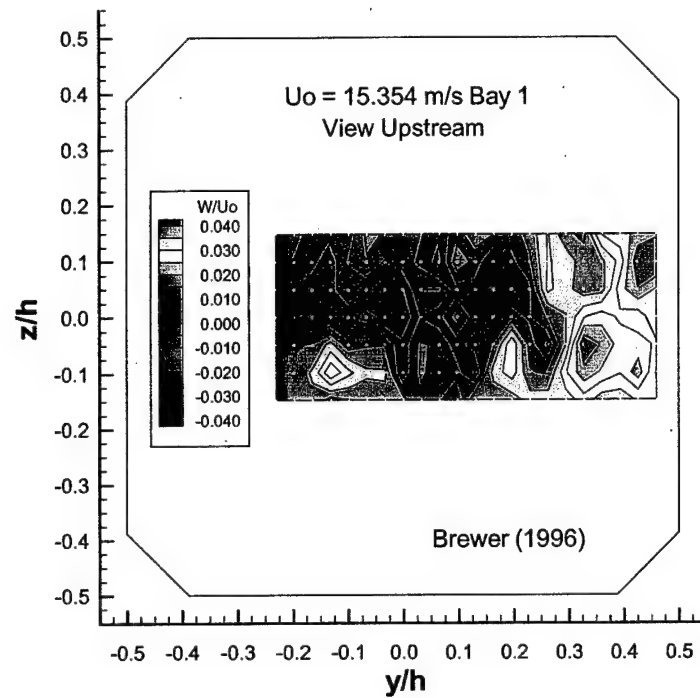


(a) Vertical Velocity Component

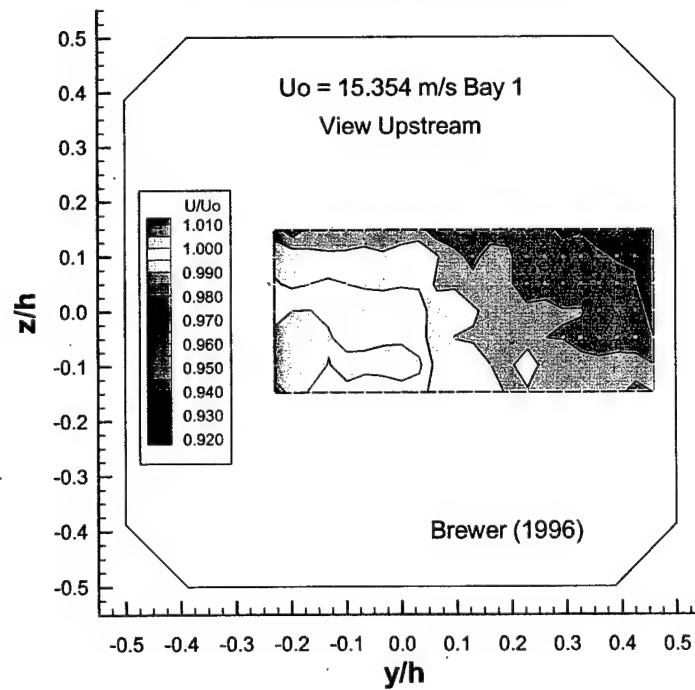


(b) Axial Velocity Component

Figure 30. Contour Plots for an Empty Test Section in Bay 1 at 9.2 m/s

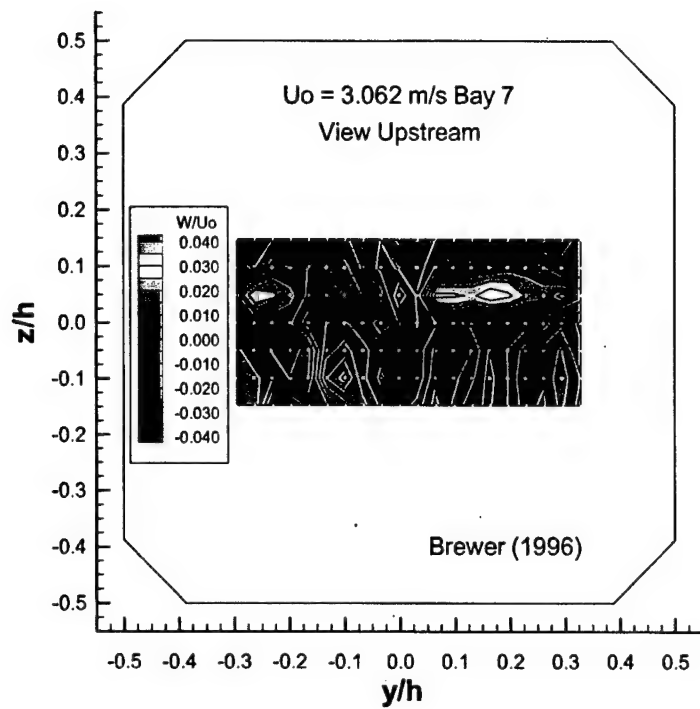


(a) Vertical Velocity Component

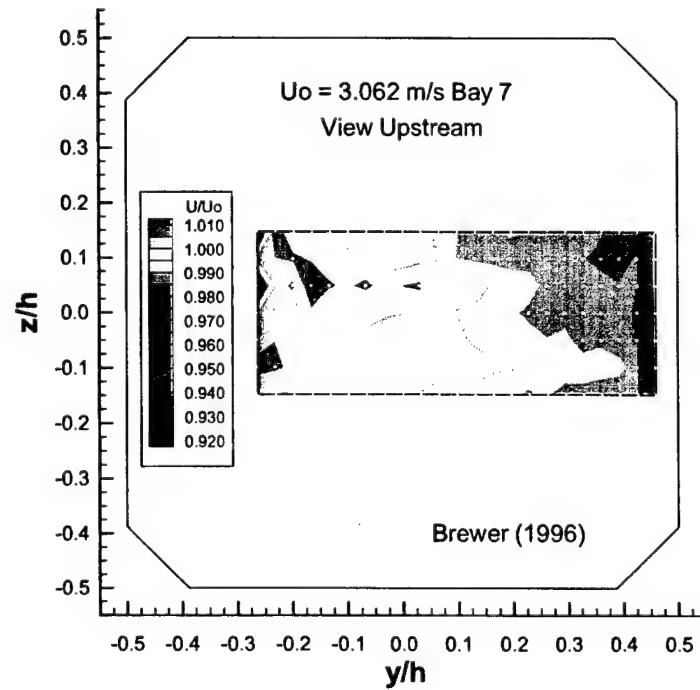


(b) Axial Velocity Component

Figure 31. Contour Plots for an Empty Test Section in Bay 1 at 15.4 m/s

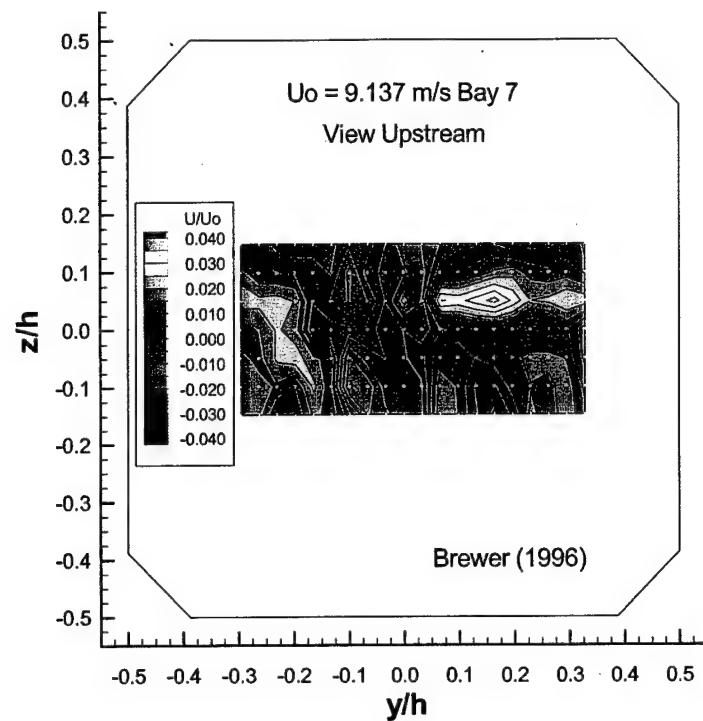


(a) Vertical Velocity Component

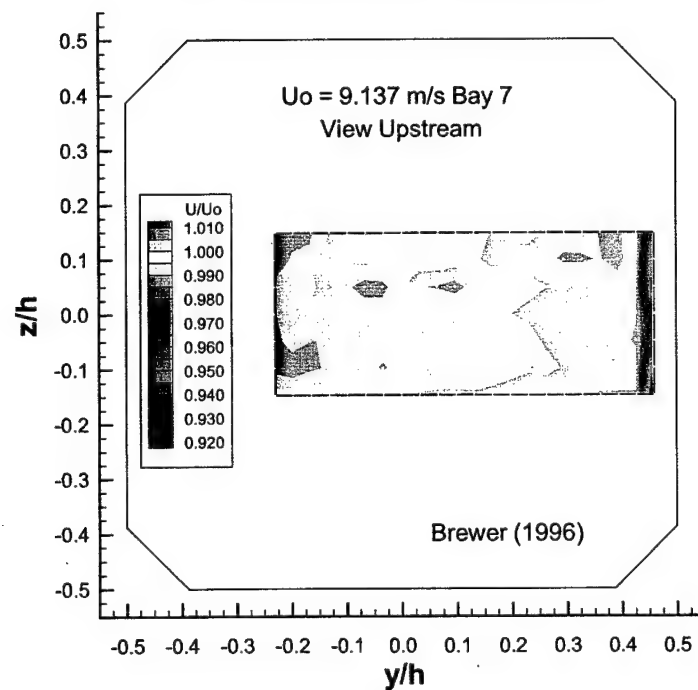


(b) Axial Velocity Component

Figure 32. Contour Plots for an Empty Test Section in Bay 7 at 3.1 m/s

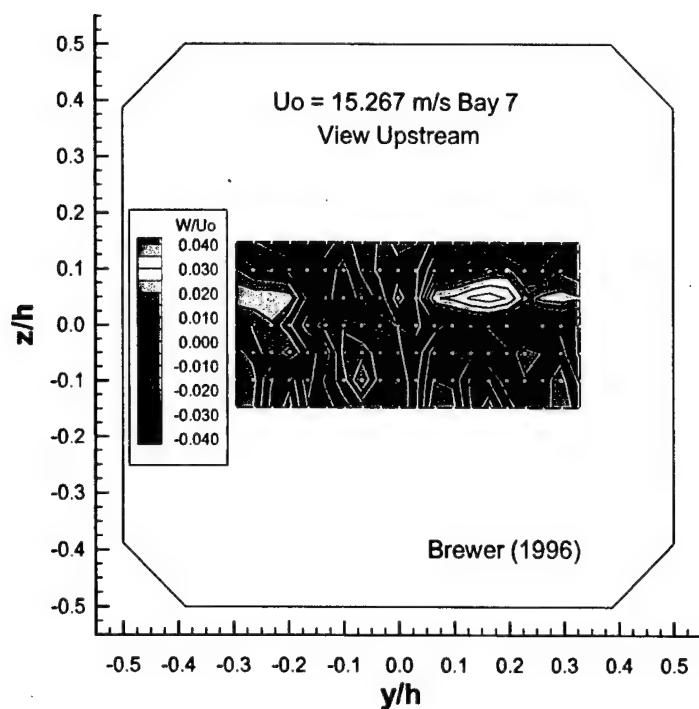


(a) Vertical Velocity Component

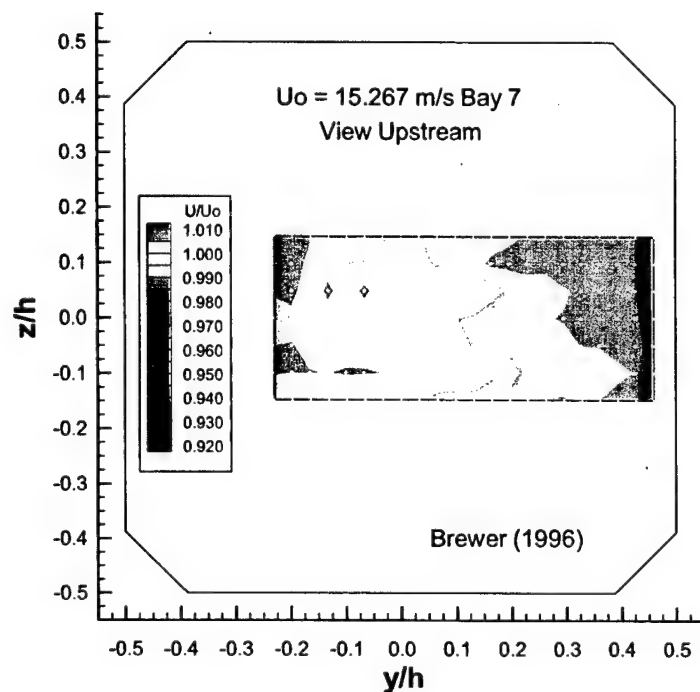


(b) Axial Velocity Component

Figure 33. Contour Plots for an Empty Test Section in Bay 7 at 9.1 m/s



(a) Vertical Velocity Component



(b) Axial Velocity Component

Figure 34. Contour Plots for an Empty Test Section in Bay 7 at 15.3 m/s

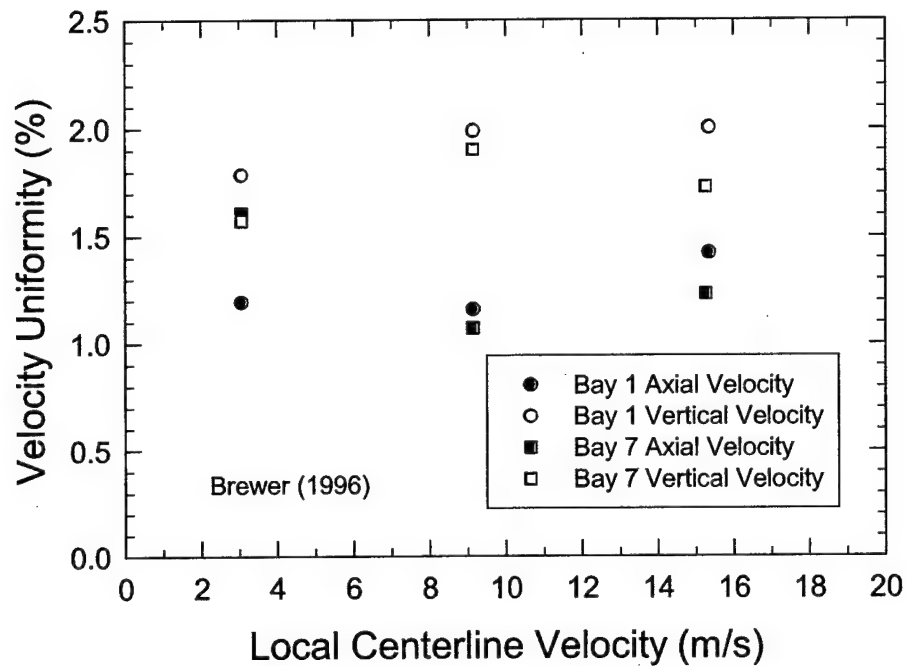


Figure 35. Summary of Velocity Uniformity Measurements for 1996

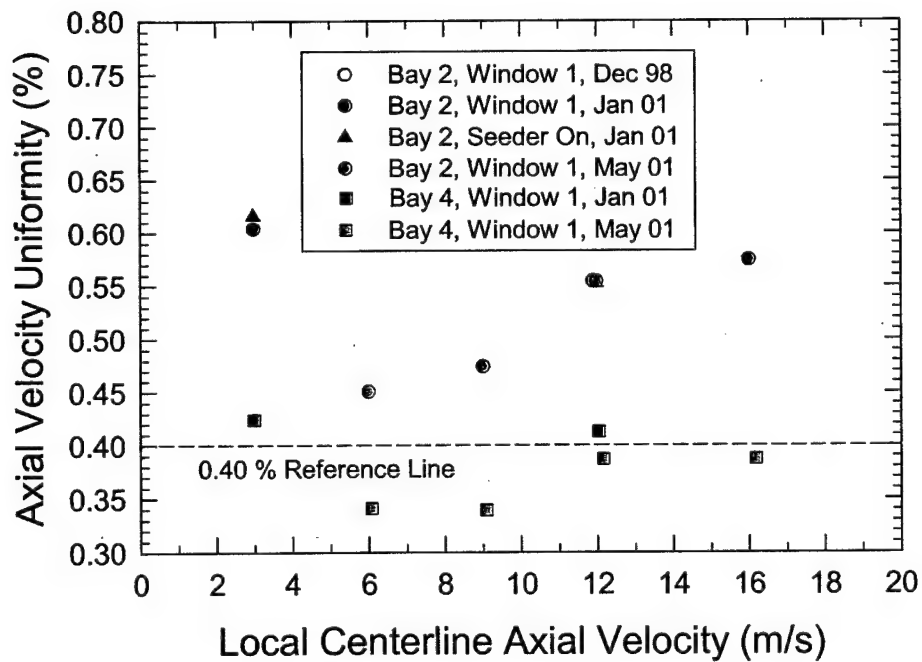


Figure 36. Summary of Spatial Variation in Axial Velocity

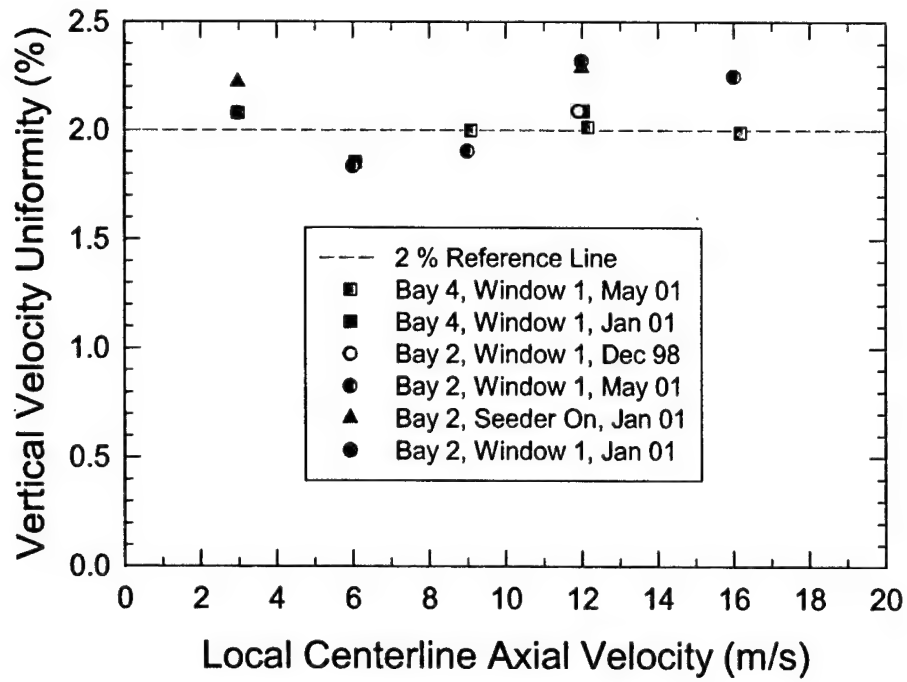
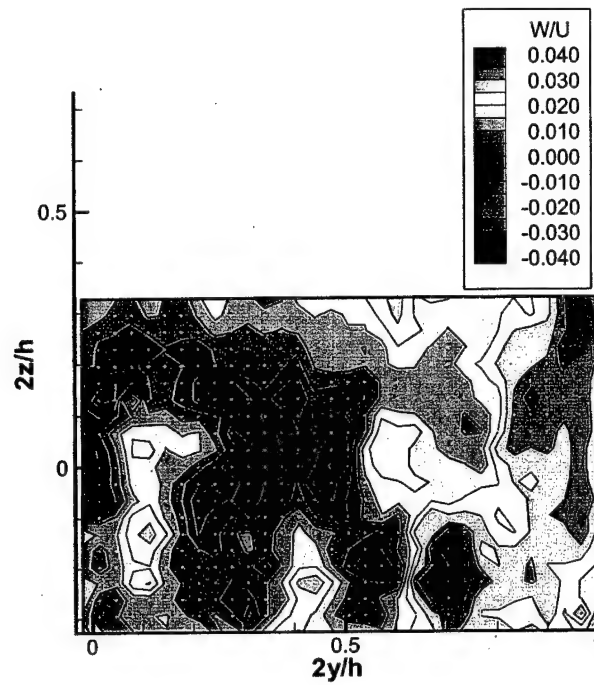
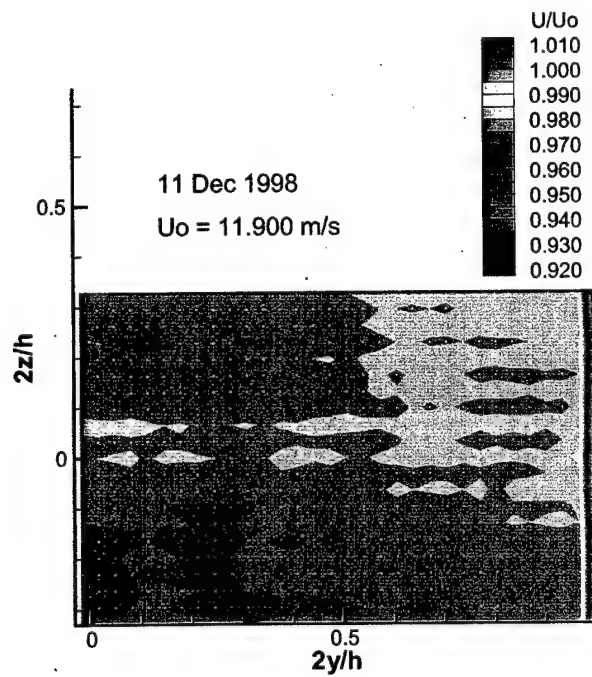


Figure 37. Summary of Spatial Variation in Vertical Velocity

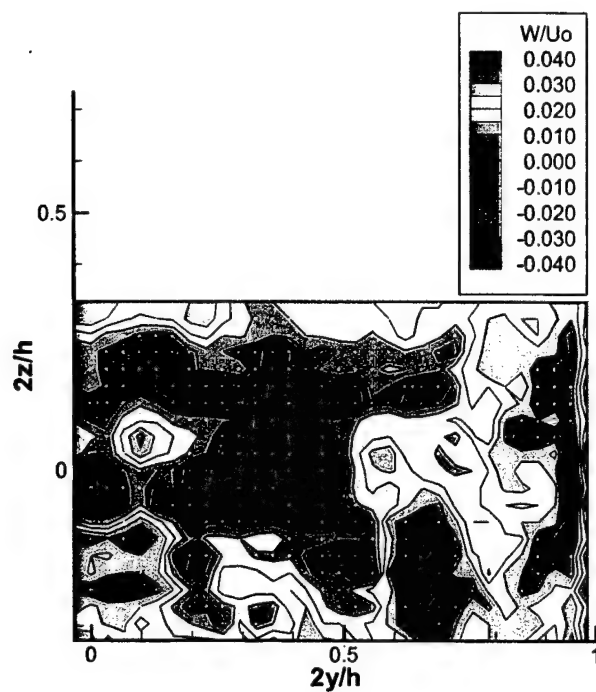


(a) Vertical Velocity Component

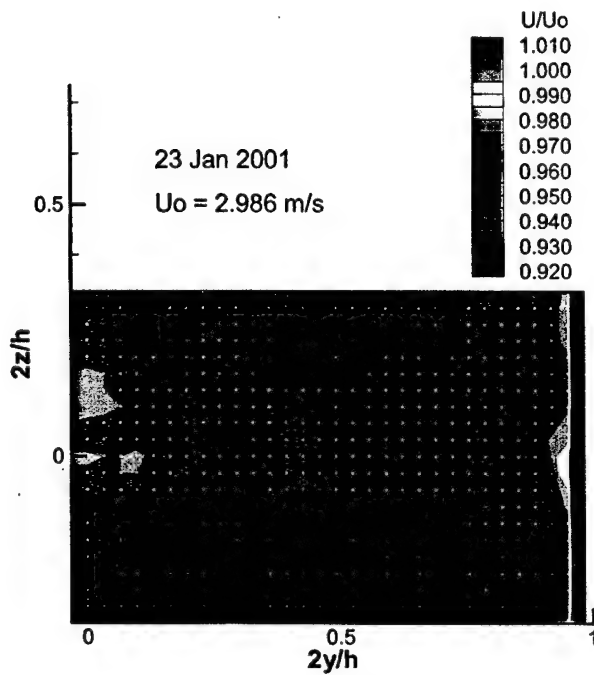


(b) Axial Velocity Component

Figure 38. Contour Plots for Test Section in Bay 2 Window 1 at 12 m/s in 1998

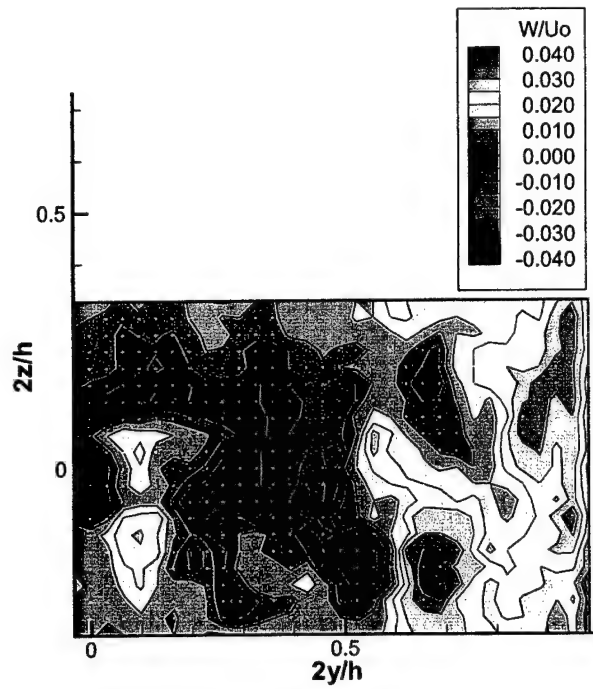


(a) Vertical Velocity Component

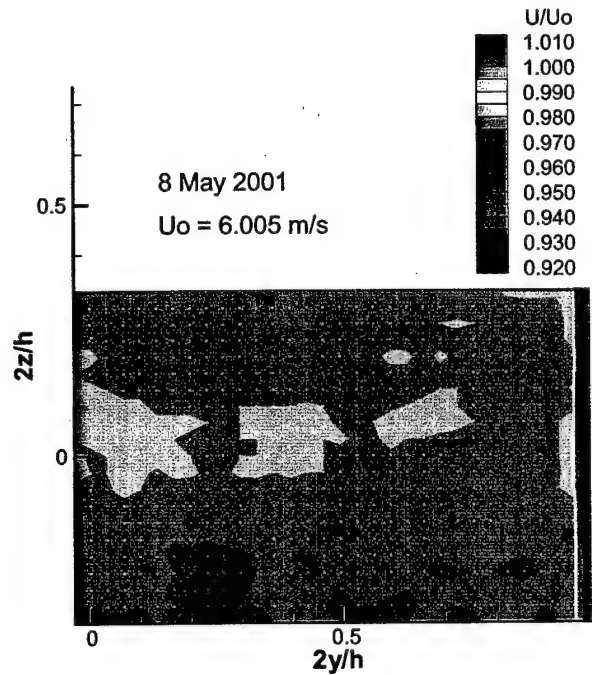


(b) Axial Velocity Component

Figure 39. Contour Plots for Test Section in Bay 2 Window 1 at 3 m/s in 2001

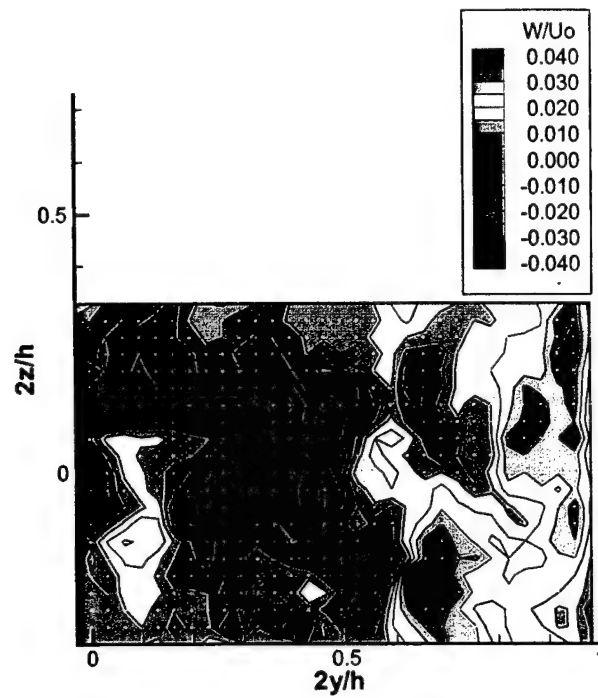


(a) Vertical Velocity Component

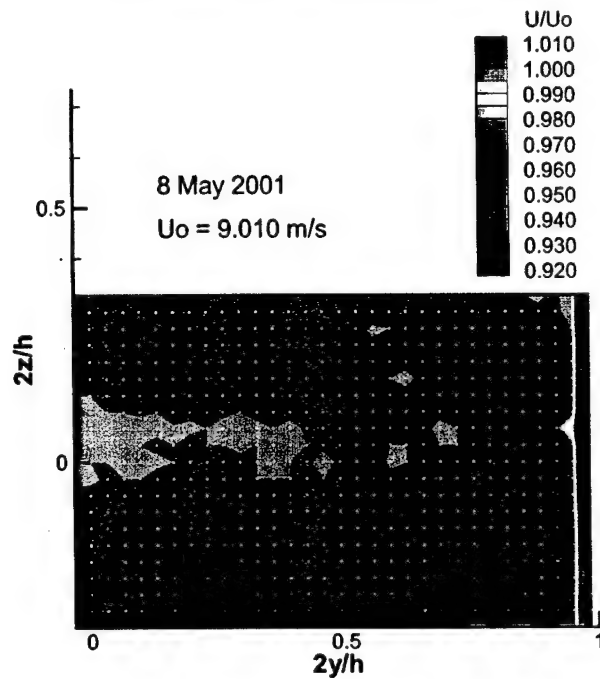


(b) Axial Velocity Component

Figure 40. Contour Plots for Test Section in Bay 2 Window 1 at 6 m/s in 2001

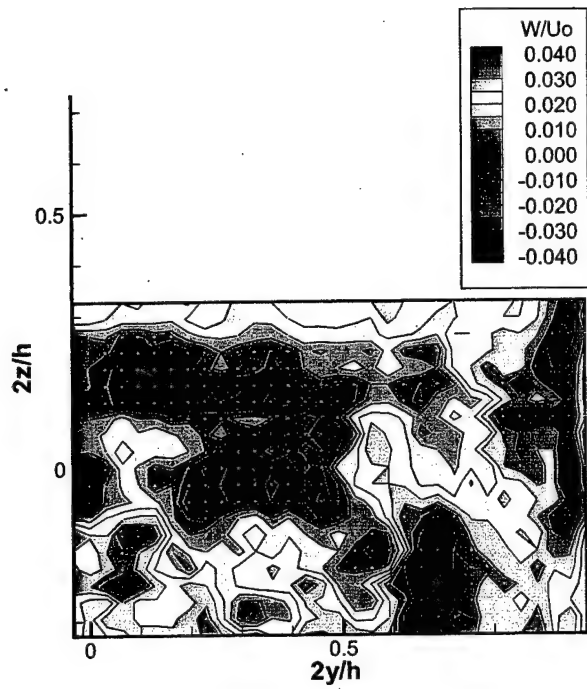


(a) Vertical Velocity Component

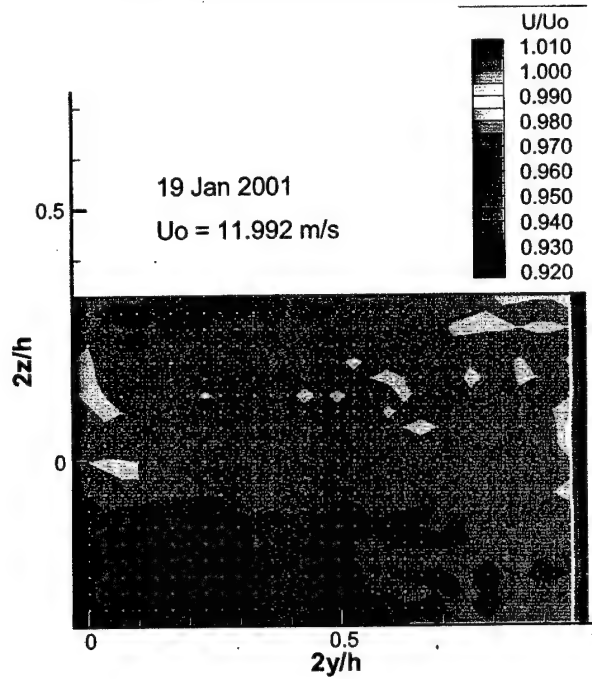


(b) Axial Velocity Component

Figure 41. Contour Plots for Test Section in Bay 2 Window 1 at 9 m/s in 2001

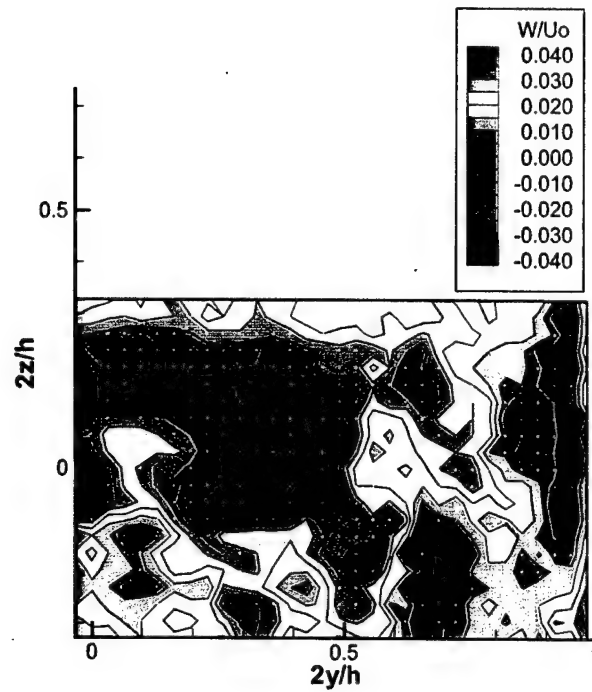


(a) Vertical Velocity Component

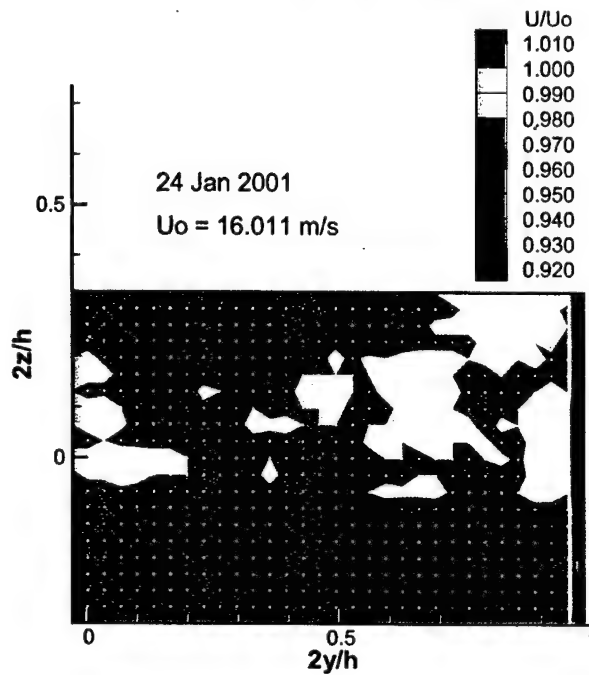


(b) Axial Velocity Component

Figure 42. Contour Plots for Test Section in Bay 2 Window 1 at 12 m/s in 2001

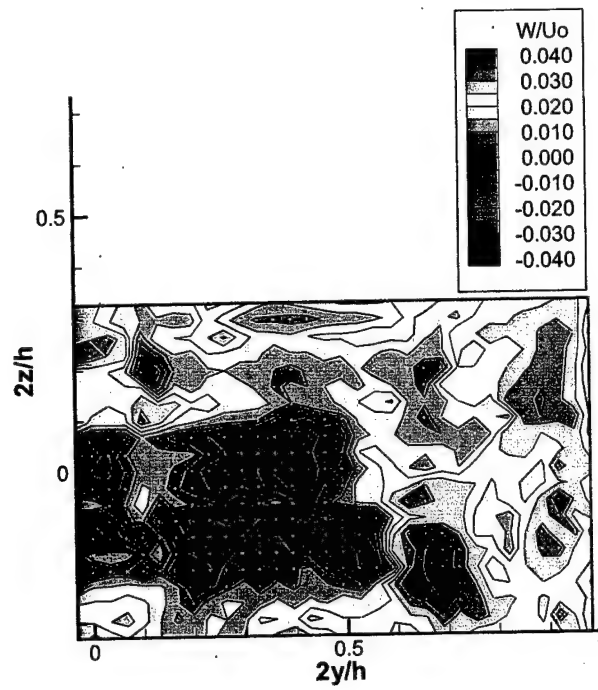


(a) Vertical Velocity Component

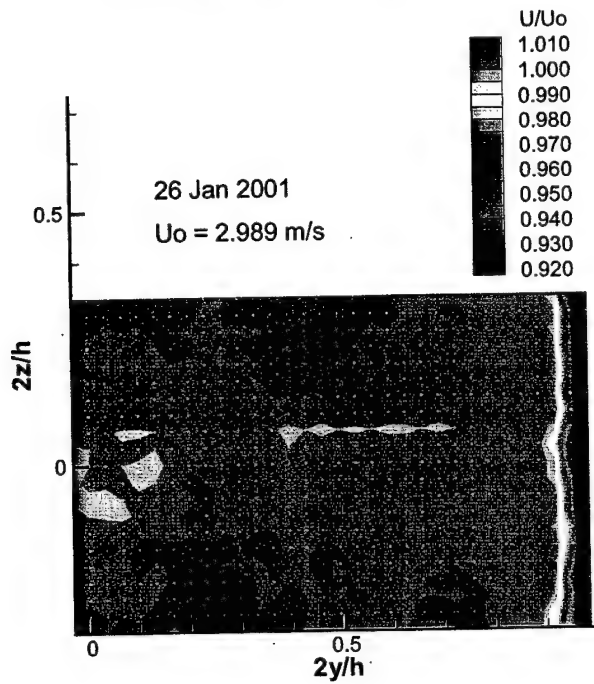


(b) Axial Velocity Component

Figure 43. Contour Plots for Test Section in Bay 2 Window 1 at 16 m/s in 2001

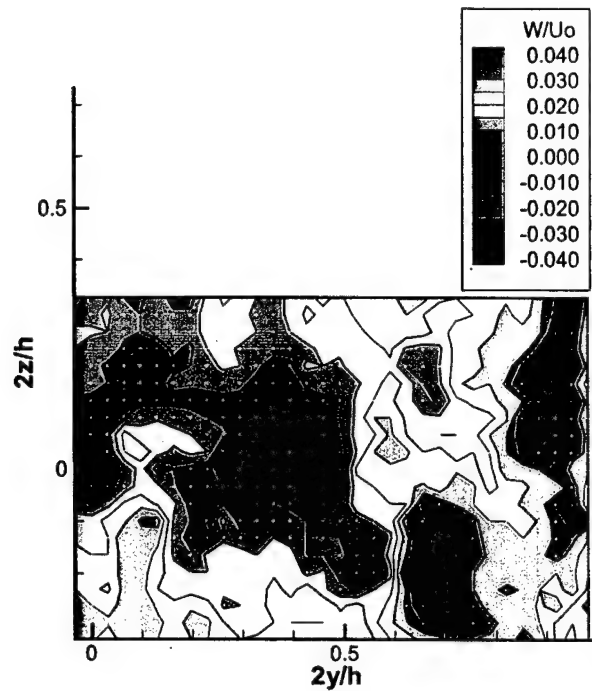


(a) Vertical Velocity Component

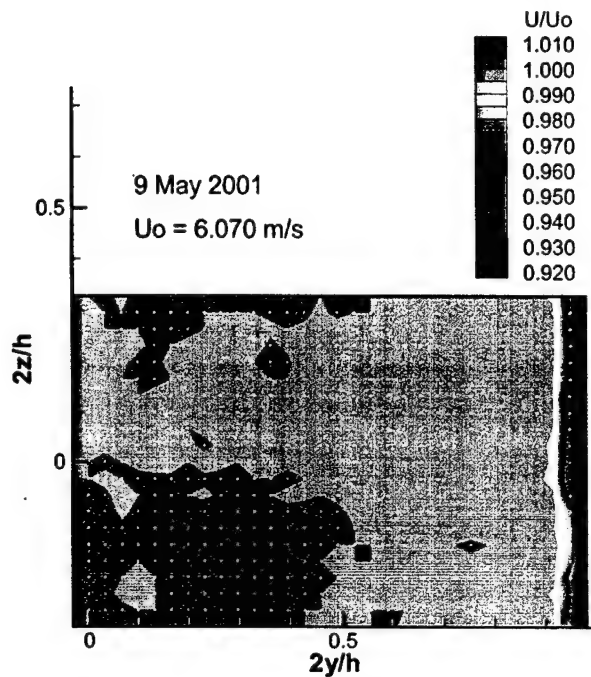


(b) Axial Velocity Component

Figure 44. Contour Plots for Test Section in Bay 4 Window 1 at 3 m/s in 2001

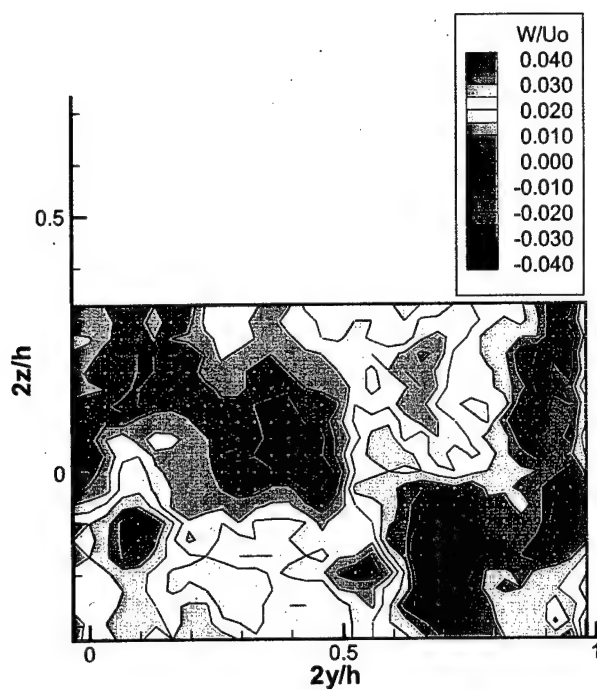


(a) Vertical Velocity Component

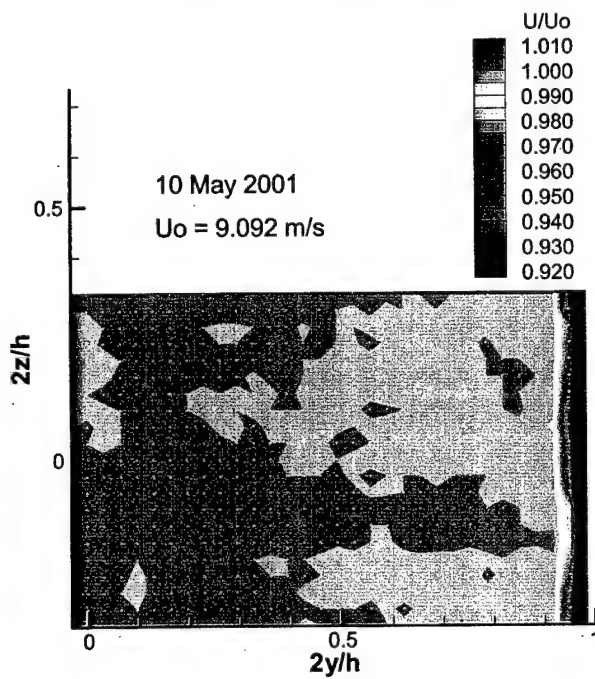


(b) Axial Velocity Component

Figure 45. Contour Plots for Test Section in Bay 4 Window 1 at 6 m/s in 2001

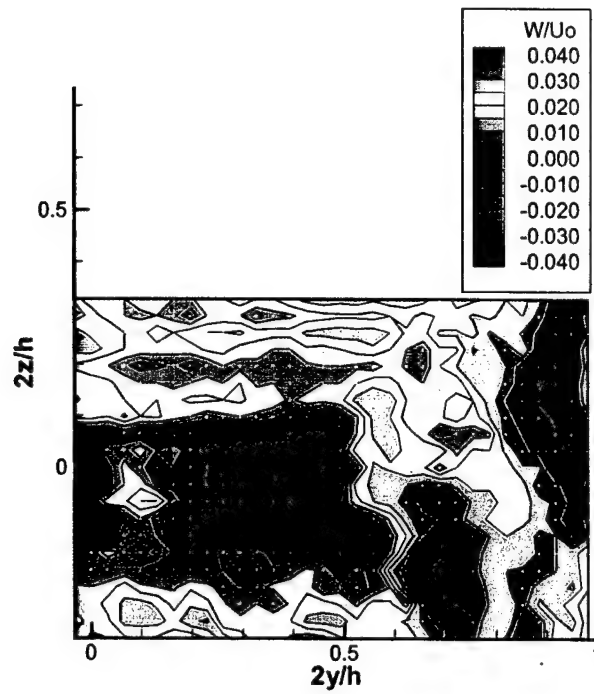


(a) Vertical Velocity Component

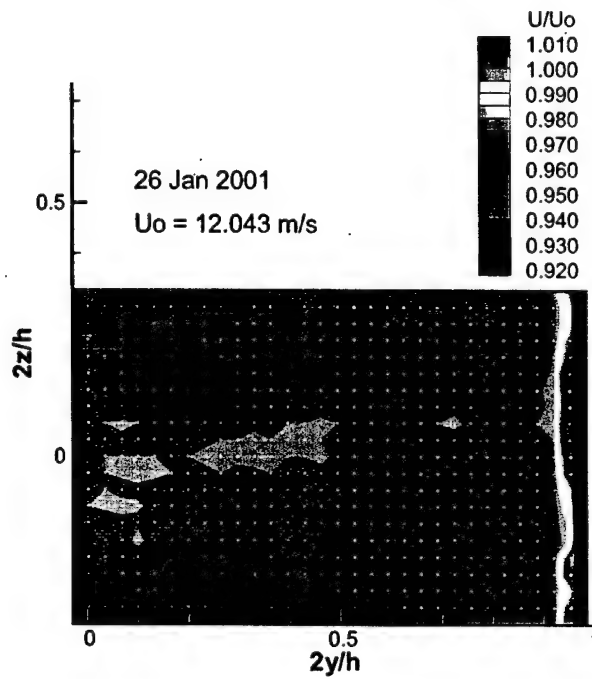


(b) Axial Velocity Component

Figure 46. Contour Plots for Test Section in Bay 4 Window 1 at 9 m/s in 2001

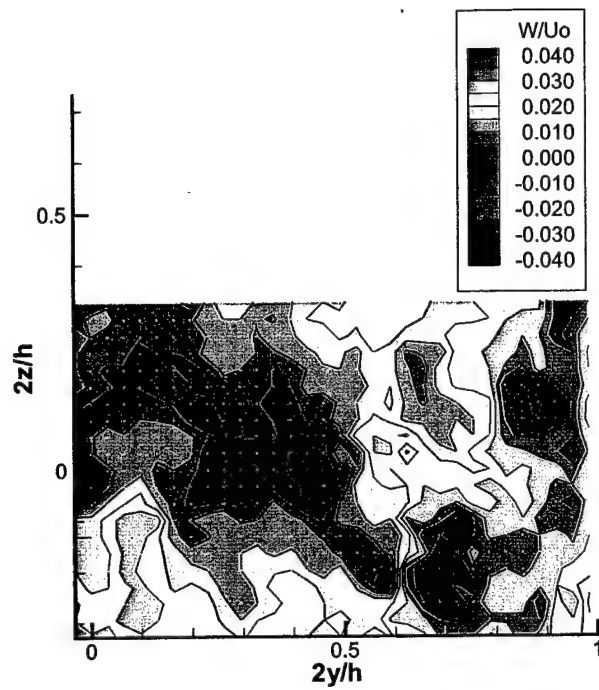


(a) Vertical Velocity Component

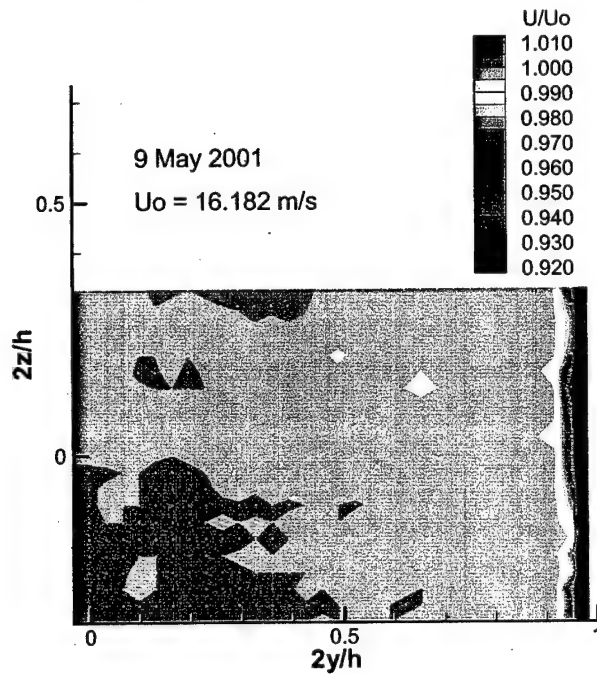


(b) Axial Velocity Component

Figure 47. Contour Plots for Test Section in Bay 4 Window 1 at 12 m/s in 2001



(a) Vertical Velocity Component



(b) Axial Velocity Component

Figure 48. Contour Plots for Test Section in Bay 4 Window 1 at 16 m/s in 2001



Figure 49. Hot-Film Support Fixture and Submarine Strut at Test-Top Stand

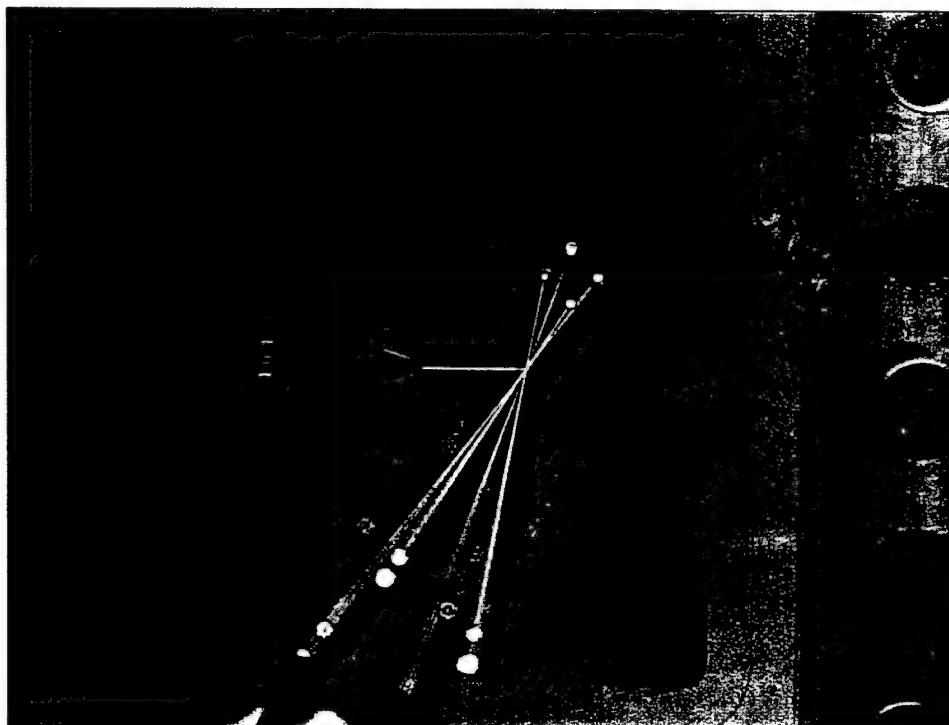
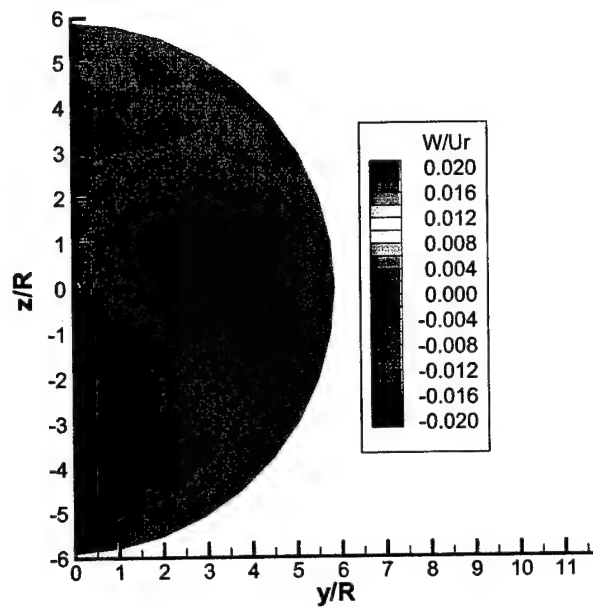
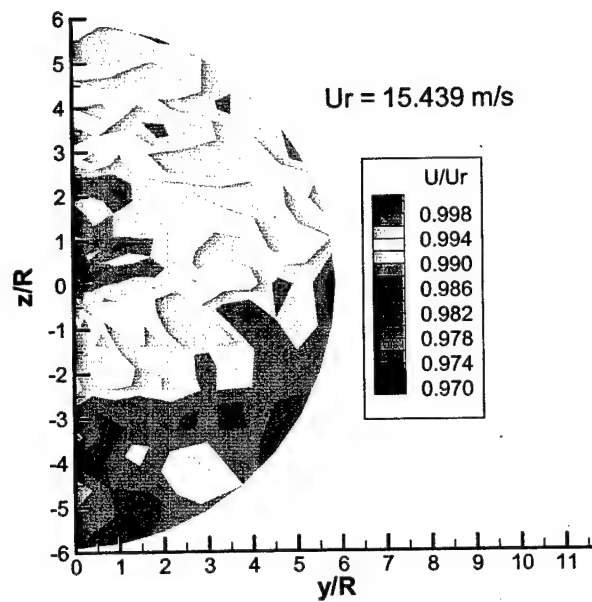


Figure 50. Hot-Film in Test Section with LDA in Operation in Bay 4 Window

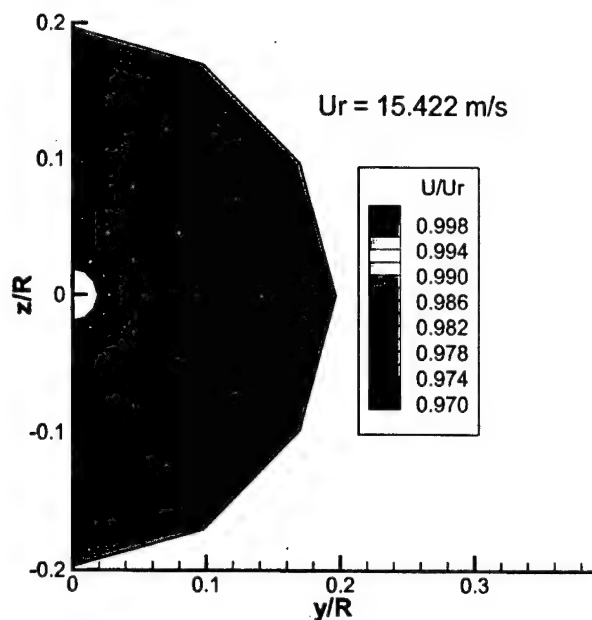


(a) Vertical Velocity Component

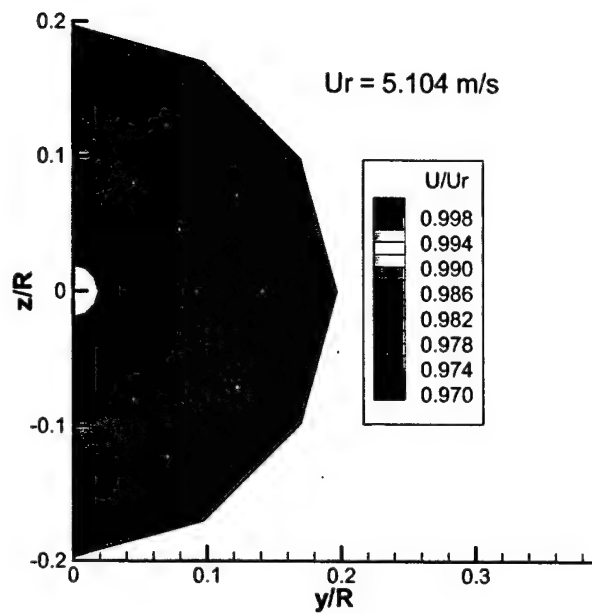


(b) Axial Velocity Component

Figure 51. Inflow to Conical Hot-Film 2 mm Upstream at 15 m/s



(a) Axial Velocity Component at 15 m/s



(b) Axial Velocity Component at 5 m/s

Figure 52. Inflow to Conical Hot-Film 2 mm Upstream at High Resolution

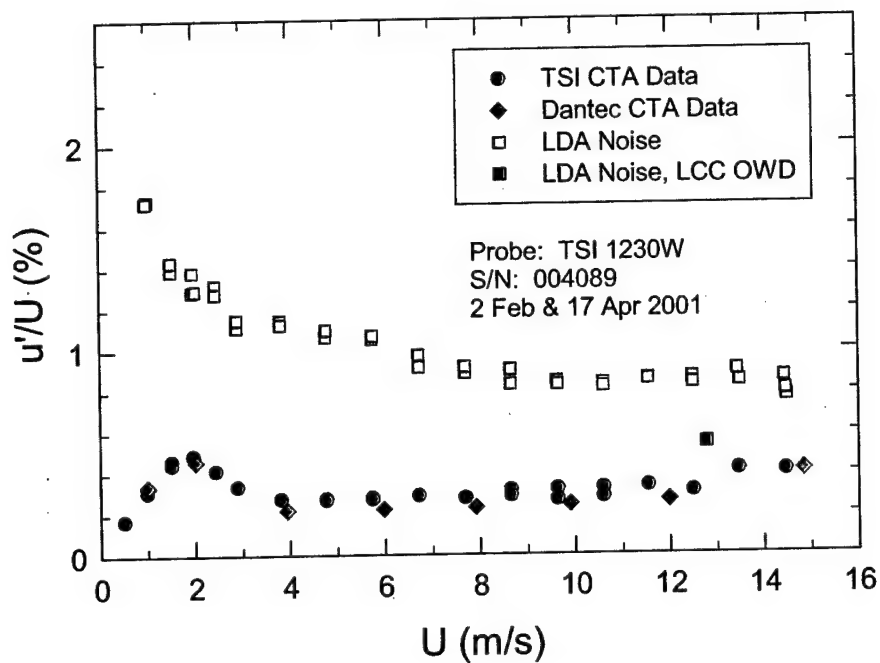


Figure 53. Test Section Turbulence from Hot-Film in Comparison to LDA Noise

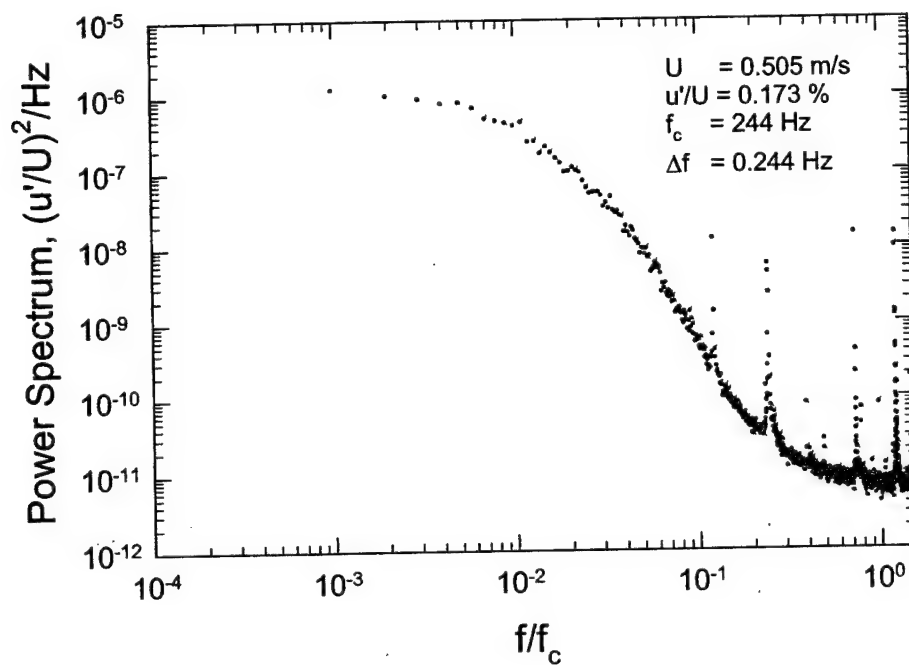
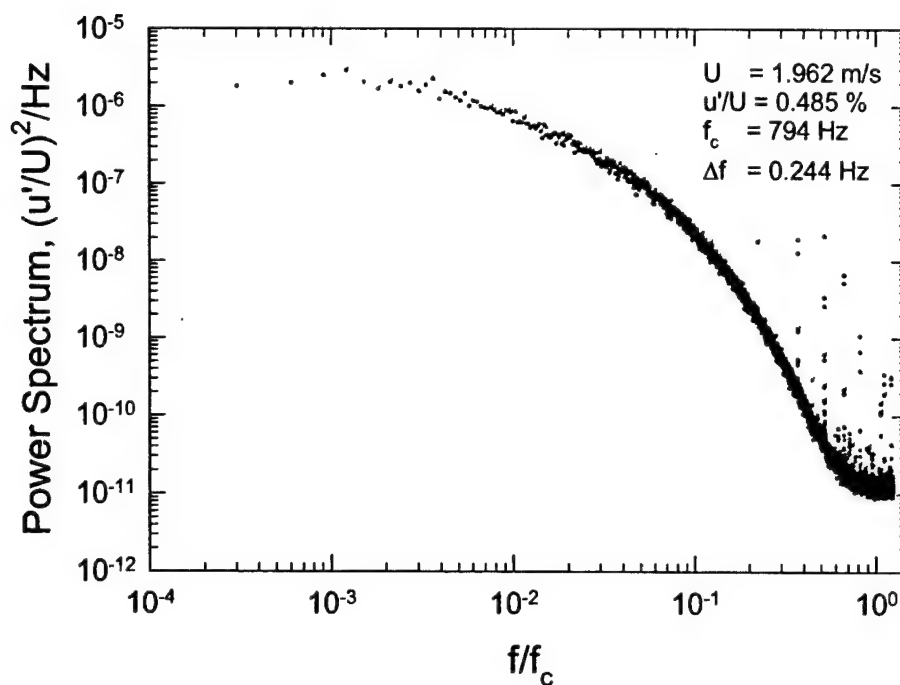
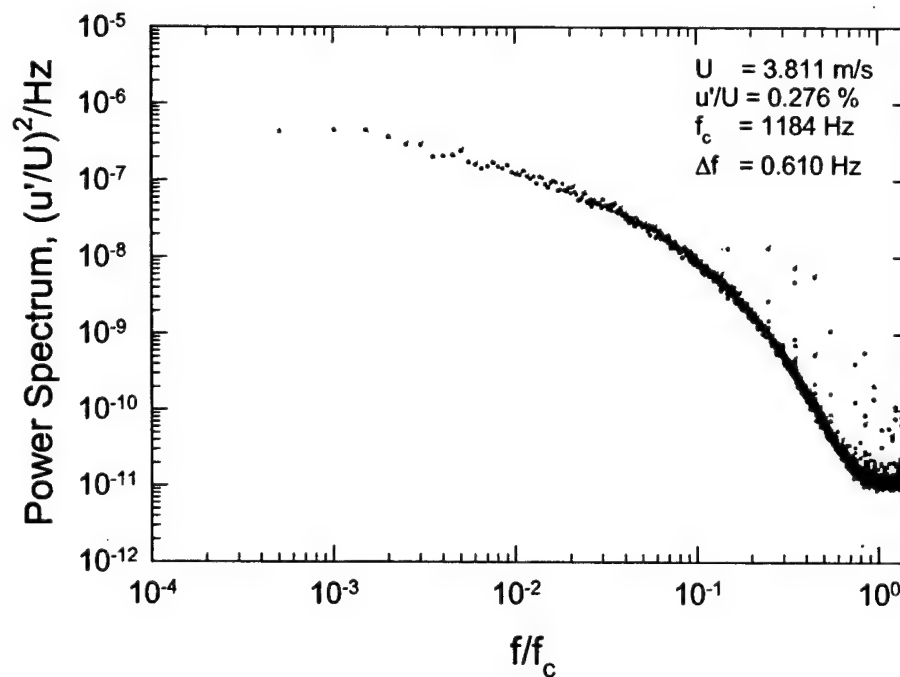
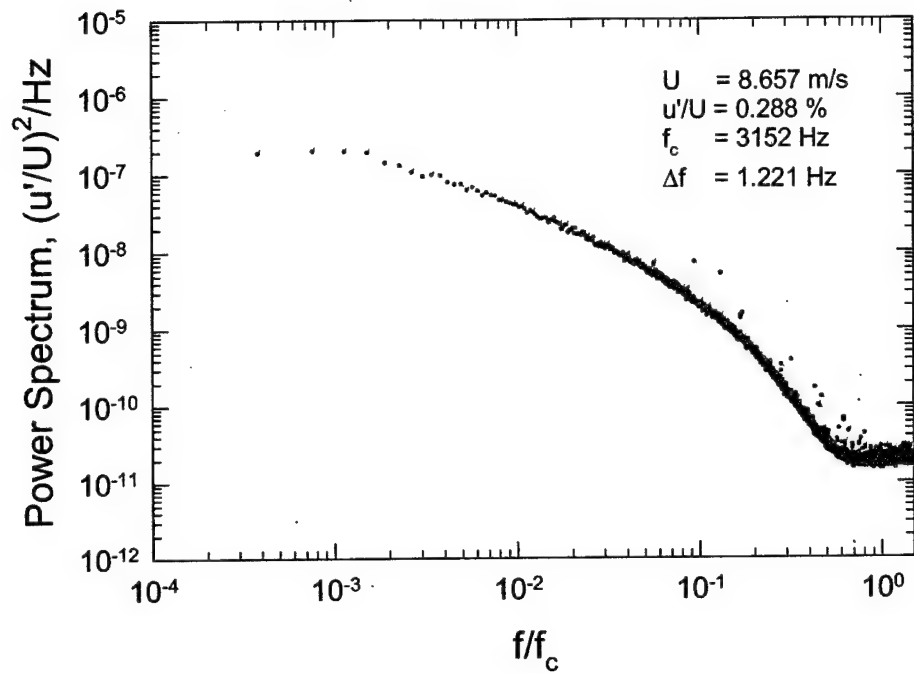
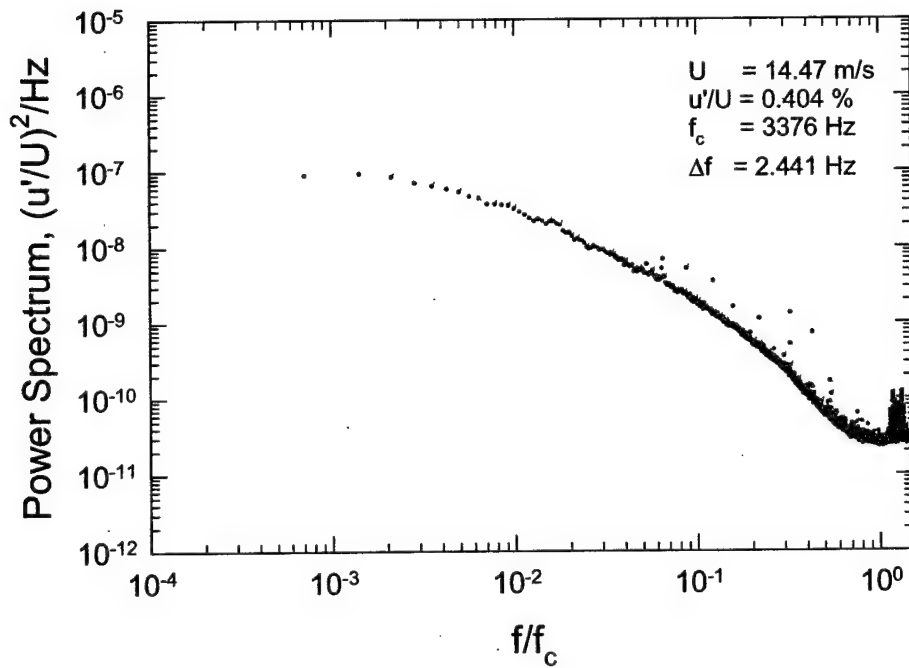


Figure 54. Velocity Frequency Spectrum for 0.5 m/s

**Figure 55. Velocity Frequency Spectrum for 2 m/s****Figure 56. Velocity Frequency Spectrum for 4 m/s**

**Figure 57. Velocity Frequency Spectrum for 9 m/s****Figure 58. Velocity Frequency Spectrum for 14.5 m/s**

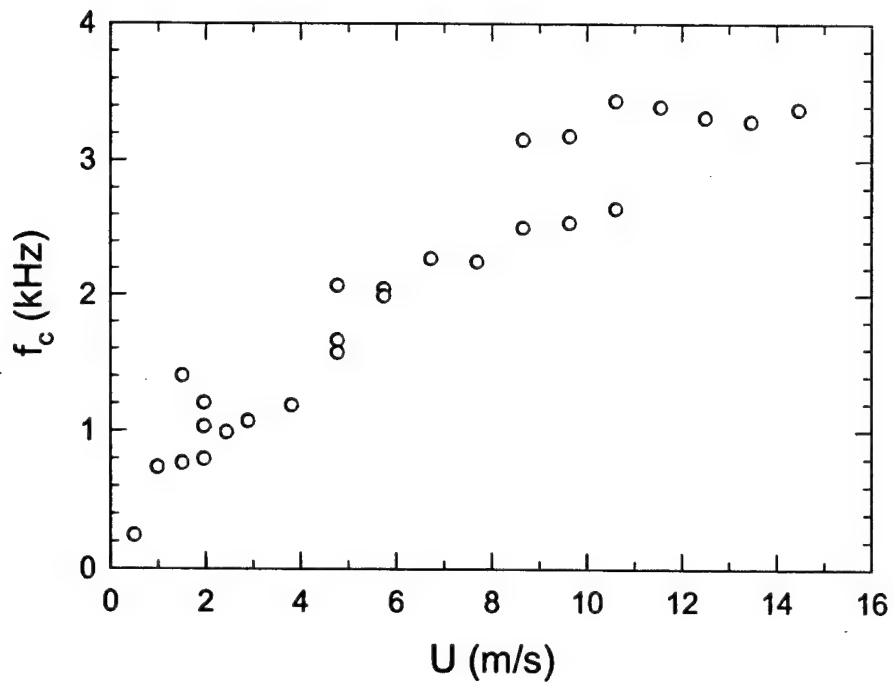


Figure 59. Measured Cutoff Frequency of Turbulence from Spectra

Table 1. Optical Characteristics for Dantec 85 mm Fiber Optic Probe

| Parameter | Symbol | Units | Value | Value | Value |
|-----------------------|-----------|---------|--------|--------|--------|
| Beam diameter | d | mm | 1.35 | 1.35 | 1.35 |
| Beam expansion | M | | 2.775 | 2.775 | 2.775 |
| Beam spacing | D | mm | 115 | 115 | 115 |
| Focal Length | f | mm | 800 | 1600 | 1600 |
| Wave length | λ | nm | 476.5 | 488 | 514.5 |
| Half angle | κ | degrees | 4.11 | 2.06 | 2.06 |
| Fringe spacing | δ | microns | 3.32 | 6.79 | 7.16 |
| Beam waist diameter | de | microns | 129.56 | 265.37 | 279.78 |
| Probe diameter | dm | microns | 129.89 | 265.54 | 279.96 |
| Probe length | dl | mm | 1.81 | 7.39 | 7.79 |
| No. of fringes | Nf | | 39.09 | 39.09 | 39.09 |
| Probe length in water | dl | mm | 2.40 | 9.83 | 10.36 |

Table 2. Optical Characteristics for Dantec 112 mm Fiber Optic Probe

| Parameter | Symbol | Units | Value | Value |
|-----------------------|-----------|---------|--------|--------|
| Beam diameter | d | mm | 4.1 | 4.1 |
| Beam expansion | M | | 1.5 | 1.5 |
| Beam spacing | D | mm | 111 | 111 |
| Focal Length | f | mm | 1600 | 1600 |
| Wave length | λ | nm | 488 | 514.5 |
| Half angle | κ | degrees | 1.99 | 1.99 |
| Fringe spacing | δ | microns | 7.04 | 7.42 |
| Beam waist diameter | de | microns | 161.65 | 170.43 |
| Probe diameter | dm | microns | 161.75 | 170.53 |
| Probe length | dl | mm | 4.66 | 4.92 |
| No. of fringes | Nf | | 22.98 | 22.98 |
| Probe length in water | dl | mm | 6.20 | 6.54 |

Table 3. Window Locations Relative to Test Top Opening

| Bay # | Window # | x (in) | x (mm) | x/L |
|-------|----------|--------|---------|--------|
| 1 | 1 | 8.38 | 212.7 | 0.0162 |
| 1 | 2 | 38.50 | 977.9 | 0.0745 |
| 2 | 1 | 86.88 | 2206.6 | 0.1682 |
| 2 | 2 | 117.00 | 2971.8 | 0.2265 |
| 3 | 1 | 165.38 | 4200.5 | 0.3202 |
| 3 | 2 | 195.50 | 4965.7 | 0.3785 |
| 4 | 1 | 243.88 | 6194.4 | 0.4722 |
| 4 | 2 | 274.00 | 6959.6 | 0.5305 |
| 5 | 1 | 322.38 | 8188.3 | 0.6242 |
| 5 | 2 | 352.50 | 8953.5 | 0.6825 |
| 6 | 1 | 400.88 | 10182.2 | 0.7761 |
| 6 | 2 | 431.00 | 10947.4 | 0.8345 |
| 7 | 1 | 479.38 | 12176.1 | 0.9281 |
| 7 | 2 | 509.50 | 12941.3 | 0.9864 |
| 8 | 1 | 557.88 | 14170.0 | 1.0801 |
| 8 | 2 | 588.00 | 14935.2 | 1.1384 |

L = Test top opening, 13.11 m (516.5 in)

Table 4. Statistics of Measurements for Test Section Velocity Uniformity

| Date | Bay | Uo (m/s) | n | Mean U/Uo | Std. Dev. U/Uo | U95 (%) | n | Mean W/Uo | Std. Dev. W/Uo | U95 (%) |
|------------|-----|-------------|-----|--------------|-------------------|------------|-----|--------------|-------------------|------------|
| 11-Dec-98 | 2 | 11.900 | 651 | 1.0018 | 0.00282 | 0.554 | 648 | 0.0146 | 0.0106 | 2.089 |
| 23-Jan-01 | 2 | 2.986 | 649 | 1.0055 | 0.00308 | 0.604 | 647 | 0.0178 | 0.0106 | 2.078 |
| *25-Jan-01 | 2 | 2.983 | 650 | 1.0065 | 0.00314 | 0.616 | 643 | 0.0186 | 0.0113 | 2.221 |
| 8-May-01 | 2 | 6.005 | 651 | 1.0024 | 0.00230 | 0.451 | 649 | 0.0127 | 0.0093 | 1.835 |
| 8-May-01 | 2 | 9.010 | 651 | 1.0028 | 0.00241 | 0.474 | 646 | 0.0125 | 0.0097 | 1.904 |
| 19-Jan-01 | 2 | 11.992 | 651 | 1.0036 | 0.00282 | 0.554 | 651 | 0.0189 | 0.0118 | 2.320 |
| *22-Jan-01 | 2 | 11.988 | 650 | 1.0037 | 0.00281 | 0.552 | 650 | 0.0209 | 0.0117 | 2.288 |
| 24-Jan-01 | 2 | 16.011 | 649 | 1.0026 | 0.00292 | 0.574 | 649 | 0.0178 | 0.0115 | 2.248 |
| 26-Jan-01 | 4 | 2.989 | 616 | 1.0037 | 0.00216 | 0.424 | 616 | 0.0159 | 0.0106 | 2.080 |
| 9-May-01 | 4 | 6.070 | 630 | 0.9991 | 0.00174 | 0.341 | 628 | 0.0190 | 0.0094 | 1.852 |
| 10-May-01 | 4 | 9.092 | 630 | 1.0002 | 0.00173 | 0.339 | 627 | 0.0206 | 0.0102 | 1.999 |
| 26-Jan-01 | 4 | 12.043 | 629 | 1.0035 | 0.00210 | 0.413 | 625 | 0.0188 | 0.0106 | 2.089 |
| 10-May-01 | 4 | 12.157 | 630 | 0.9987 | 0.00197 | 0.387 | 626 | 0.0175 | 0.0103 | 2.015 |
| 9-May-01 | 4 | 16.182 | 629 | 0.9984 | 0.00197 | 0.387 | 629 | 0.0175 | 0.0101 | 1.989 |

*PIV seeder flow at maximum

Table 5. Statistics for Velocity Uniformity Measurements for HiFoil Experiment

| Uo (m/s) | n | Mean U/Uo | Std. Dev. U/Uo | U95 (%) | Mean W/Uo | Std. Dev. W/Uo | U95 (%) |
|-------------|-----|--------------|-------------------|------------|--------------|-------------------|------------|
| 3.066 | 165 | 1.0019 | 0.00451 | 0.891 | 0.0128 | 0.0104 | 2.051 |
| 6.192 | 165 | 1.0029 | 0.00532 | 1.050 | 0.0116 | 0.0110 | 2.175 |
| 12.399 | 165 | 1.0016 | 0.00473 | 0.935 | 0.0095 | 0.0119 | 2.351 |
| 18.883 | 176 | 1.0015 | 0.00705 | 1.391 | 0.0102 | 0.0122 | 2.402 |

Table 6. Characteristics of U. S. Water Tunnels and SSPA

| Organization/Location | Ref. | Test Section Dimensions (m) | Area Ratio | Maximum Velocity (m/s) | u'/U (%) |
|---------------------------------------|--------------------|--------------------------------|---------------|---------------------------|---------------|
| Cal. Tech Pasadena, CA | [18] | 0.356 D | 20 | --- | 0.04 |
| Case Western Reserve Cleveland, OH | [19], [20] [21] | 0.15 x 0.23 | 25 | 12 | 0.2 |
| NIST Gaithersburg, MD | [15], [16] | 0.61 D | 9 | 6.1 | 0.1 |
| Penn State U. State College, PA | [13], [14] | 1.22 D | 9 | 18.3 | 0.1 |
| NOSC San Diego, CA | [22] | 0.305 | 7.5 | 19 | 0.1 |
| Southwest Research San Antonio, TX | [23] | 0.152 x 0.229 | 16.7 | 5 | 0.07 |
| SSPA Sweden Goteborg, Sweden | [24] | 2.1 x 1.22 | 2.76 | 9.9 | 0.15 |
| LCC Memphis, TN | | 3.05 x 3.05 | 6.0 | 19 | 0.2 |

Blind Copy to:

5010 Files w/o encl.

5100 Files w/o encl.

5040 Yarnall (3)

5060 Walden (1)

5102 Hornaday (3)

Cutbirth (3)

5200 Day (2)

5300 Johnston (1)

Coakley (1)

5400 Etter (1)

Park (3)

Wilson (1)

DTIC (1)

Library (2)

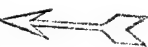


Table 7. Summary of Turbulence Data for TSI IFA-300 CTA

| U | Pump ω | Samples | Time | SR | LP | u'/U | Δf | Blade f |
|--------|---------------|---------|--------|-------|----------|--------|------------|---------|
| (m/s) | (rpm) | (kpts) | (s) | (kHz) | (kHz) | (%) | (Hz) | (Hz) |
| 0.5048 | 2.06 | 512 | 262.14 | 2 | 10.1726 | 0.2441 | 0.240 | |
| 0.9900 | 3.63 | 512 | 262.14 | 2 | 10.3129 | 0.2441 | 0.424 | |
| 1.510 | 5.19 | 1024 | 209.72 | 5 | 20.4647 | 0.6104 | 0.606 | |
| 1.510 | 5.19 | 512 | 262.14 | 2 | 10.4460 | 0.2441 | 0.606 | |
| 1.962 | 6.75 | 1024 | 209.72 | 5 | 20.4912 | 0.6104 | 0.788 | |
| 1.962 | 6.75 | 1024 | 209.72 | 5 | 20.4899 | 0.6104 | 0.788 | |
| 1.962 | 6.75 | 512 | 262.14 | 2 | 10.4854 | 0.2441 | 0.788 | |
| 2.438 | 8.33 | 1024 | 209.72 | 5 | 20.4162 | 0.6104 | 0.972 | |
| 2.894 | 9.87 | 1024 | 209.72 | 5 | 20.3375 | 0.6104 | 1.152 | |
| 3.811 | 13.05 | 1024 | 209.72 | 5 | 20.2757 | 0.6104 | 1.523 | |
| 4.772 | 16.22 | 2048 | 209.72 | 10 | 50.2745 | 1.2207 | 1.892 | |
| 4.772 | 16.22 | 2048 | 419.43 | 5 | 20.2776 | 0.6104 | 1.892 | |
| 4.772 | 16.22 | 1024 | 209.72 | 5 | 20.2691 | 0.6104 | 1.892 | |
| 5.744 | 19.40 | 2048 | 209.72 | 10 | 50.2807 | 1.2207 | 2.263 | |
| 5.744 | 19.40 | 1024 | 209.72 | 5 | 20.2739 | 0.6104 | 2.263 | |
| 6.724 | 22.56 | 2048 | 209.72 | 10 | 50.2902 | 1.2207 | 2.632 | |
| 7.696 | 22.56 | 2048 | 209.72 | 10 | 50.2774 | 1.2207 | 2.632 | |
| 8.657 | 25.68 | 4096 | 209.72 | 20 | 100.3152 | 2.4414 | 2.996 | |
| 8.657 | 25.68 | 2048 | 209.72 | 10 | 50.2877 | 1.2207 | 2.996 | |
| 9.634 | 31.90 | 4096 | 209.72 | 20 | 100.2675 | 2.4414 | 3.722 | |
| 9.634 | 31.90 | 2048 | 209.72 | 10 | 50.3193 | 1.2207 | 3.722 | |
| 10.602 | 35.00 | 4096 | 209.72 | 20 | 100.3237 | 2.4414 | 4.083 | |
| 10.602 | 35.00 | 4096 | 209.72 | 20 | 100.2801 | 2.4414 | 4.083 | |
| 11.549 | 38.08 | 4096 | 209.72 | 20 | 100.3321 | 2.4414 | 4.443 | |
| 12.497 | 41.16 | 4096 | 209.72 | 20 | 100.3057 | 2.4414 | 4.802 | |
| 13.464 | 44.22 | 4096 | 209.72 | 20 | 100.4114 | 2.4414 | 5.159 | |
| 14.466 | 47.29 | 4096 | 209.72 | 20 | 100.4046 | 2.4414 | 5.517 | |

SR: Sample Rate

LP: Low Pass Filter Setting

Table 8. Summary of Turbulence Data for Dantec StreamLine CTA

| U (m/s) | Pump ω (rpm) | Samples (kpts) | Time (s) | SR (kHz) | LP (kHz) | u'/U (%) |
|-------------------|--|--------------------------|--------------------|--------------------|--------------------|---------------------------------|
| 1.006 | 3.63 | 262.14 | 131.07 | 2 | 1 | 0.3333 |
| 1.006 | 3.63 | 524.29 | 262.14 | 2 | 1 | 0.3385 |
| 2.018 | 6.75 | 524.29 | 262.14 | 2 | 1 | 0.4603 |
| 3.946 | 13.05 | 524.29 | 262.14 | 2 | 1 | 0.2189 |
| 5.987 | 19.56 | 1048.58 | 174.76 | 6 | 3 | 0.2237 |
| 7.920 | 25.68 | 1048.58 | 174.76 | 6 | 3 | 0.2299 |
| 9.905 | 31.90 | 1048.58 | 174.76 | 6 | 3 | 0.2445 |
| 11.999 | 38.40 | 1048.58 | 174.76 | 6 | 3 | 0.2630 |
| 14.848 | 47.29 | 1048.58 | 174.76 | 6 | 3 | 0.4064 |

SR: Sample Rate

LP: Low Pass Filter Setting

References

- [1] Etter, R. J. and Wilson, M. B., 1992. "The Large Cavitation Channel," Proceedings of the 23rd American Towing Tank Conference, University of New Orleans, New Orleans, LA, pp 243-252.
- [2] Etter, R. J. and Wilson, M. B., October 1993. "Testing ship designs in a water tunnel," Mechanical Engineering, Vol.115/No. 10, pp. 74-80.
- [3] Blanton, J. N., 1995. "Uncertainty Estimates of Test Section Pressure and Velocity in the Large Cavitation Channel," AIAA Paper 95-3079, pp. 1-9.
- [4] Blanton, J. N. and Etter, R. J., 1995. "Laser Doppler Velocimetry on a Body of Revolution in the Large Cavitation Channel," Laser Anemometry, FED Vol. 229, edited by Thomas T. Huang, et al., American Society of Mechanical Engineers, New York, pp. 379-385.
- [5] Coleman, H. W. and Steele, W. G., 1999. Experimentation and Uncertainty Analysis for Engineers, Second Edition, New York, John Wiley & Sons.
- [6] Guide to the Expression of Uncertainty in Measurement, 1995. International Organization for Standardization (ISO), Geneva, Switzerland.
- [7] Bean, V. E. and Hall, J. M., 1999. "New Primary Standards for Air Speed Measurement at NIST," 1999 NCSL Workshop and Symposium, pp. 413-421.
- [8] Scheffe, H., 1973. "A Statistical Theory of Calibration," The Annals of Statistics, Vol. 1, No. 1, pp. 1-37.
- [9] Carroll, R. J., Spiegelman, C. H., and Sacks, J., 1988. "A Quick and Easy Multiple-Use Calibration-Curve Procedure," Technometrics, Vol. 30, No. 2, pp. 137-141.
- [10] Bridges, D. H., Blanton, J. N., Brewer, W. H., and Park, J. T., 2003. "Experimental Investigation of the Flow Past a Submarine at Angle of Drift," AIAA Journal, Vol. 41, No. 1, pp. 71-81.
- [11] Bourgoyne, D. A., Ceccio, S. L., Dowling, D. R., Jessup, S., Park, J., Brewer, W., and Pankajakshan, R., 2001. "Hydrofoil Turbulent Boundary Layer Separation at High Reynolds Numbers," 23rd Symposium on Naval Hydrodynamics, Office of Naval Research, Arlington, Virginia, pp. 314-329.
- [12] Donnelly, M. J., Etter, R. J., and Park, J. T., 2002. "Evaluation of LCC Open Water Dynamometer," NSWCCD-50-TR-2002/010, Naval Surface Warfare Center, Carderock Division, West Bethesda, Maryland.
- [13] Lumley, J. L. and McMahon, J. F., 1967. "Reducing Water Tunnel Turbulence by Means of Honeycomb," Journal of Basic Engineering, Vol. 89, pp. 764-770.
- [14] Robbins, B. E., 1978. "Water Tunnel Turbulence Measurements Behind a Honeycomb," Journal of Hydraulics, Vol. 12, No. 3, pp. 122-128.
- [15] Madigosky, W. M., Mease, N. E., Mattingly, G. E., Sweringen, J., Crouch, G., Adair, D., Hendricks, E., and Gaster, M., 1990. "Fundamental Study of Tollmein-Schlichting Waves in a Boundary Layer—Part 1: Design and Characterization of Compliant Materials for Boundary Layer Control," Fluid Measurement and Instrumentation

- Forum—1990, FED-Vol. 95, edited by E. P. Rood and C. J. Blechinger, American Society of Mechanical Engineers, New York, pp. 15-18.
- [16] Hess, D. E., 1990. "An Experimental Investigation of a Compliant Surface beneath a Turbulent Boundary Layer," Ph. D. Dissertation, Johns Hopkins University, Baltimore, Maryland.
 - [17] Nagib, H. M., Marion, A., and Tan-atichat, J., 1984. "On the Design of Contractions and Settling Chambers for Optimal Turbulence Manipulation in Wind Tunnels," AIAA Paper 84-0536.
 - [18] Liepmann, H. W., Brown, G. L., and Nosenchuck, D. M., 1982. "Control of Laminar-Instability Waves Using a New Technique," *Journal of Fluid Mechanics*, Vol. 118, pp. 187-200.
 - [19] Dumholdt, L. C., 1963. "The Design and Performance of a Low-Turbulence Water Tunnel," Ph. D. Dissertation, Case Institute of Technology, Cleveland, Ohio.
 - [20] Strazisar, A. J., Reshotko, E., and Prahl, J. M., 1977. "Experimental Study of the Stability of Heated Laminar Boundary Layers in Water," *Journal of Fluid Mechanics*, Vol. 83, pp. 225-247.
 - [21] Shin, H. W., 1982. "Experimental Study of the Effects of Surface Roughness on Laminar Boundary Layer Stability in Water," Ph. D. Dissertation, Case Western Reserve University, Cleveland, Ohio.
 - [22] Hansen, R. J., Hunston, D. L., Ni, C. C., Reischman, M. M., and Hoyt, J. W., 1980. "Hydrodynamic Drag and Surface Deformations Generated by Liquid Flows Over Flexible Surfaces," *Viscous Flow Drag Reduction* edited by G. R. Hough, American Institute of Aeronautics and Astronautics, New York, pp. 438-452.
 - [23] Park, J. T., 1988. "Flow Visualization of a Manipulated Turbulent Boundary Layer: Interaction of a Tandem Large-Eddy-Breakup Device and Wall-Injection of a Drag-Reducing Polymer Solution," *Proceedings of Symposium on Hydrodynamic Performance Enhancement for Marine Applications* edited by R. H. Nadolink, Naval Underwater Systems Center, Newport, Rhode Island, pp. 169-179.
 - [24] Johnsson, C. A. and Brannstrom, K., 1987. "Some Recent Experiences in and Additions to the SSPA Large Cavitation Tunnel," *International Symposium on Cavitation Research Facilities and Techniques—1987*, FED-Vol. 57, edited by J. W. Holl and M. L. Billet, American Society of Mechanical Engineers, New York, pp. 19-25.
 - [25] Tan-atichat, J., 1980. "Effects of Axisymmetric Contractions on Turbulence of Various Scales," Ph. D. Dissertation, Illinois Institute of Technology, Chicago.
 - [26] Bruun, H. H., 1995. "Hot-Wire Anemometry," Oxford University Press, Oxford.
 - [27] Bonis, M. and van Thinh, N., 1973. "A Heat-Transfer Law for a Conical Hot-film Probe in Water," *Disa Information*, No. 14, pp. 11-14.

Distribution

| | Copies | | Copies |
|--|--------|---|--------|
| Mr. James N. Blanton 5353 Memorial Drive, #3064 Houston, TX 77007-8266 USA | 1 | NSWC, CARDEROCK DIVISION INTERNAL DISTRIBUTION | |
| | | Code Name | |
| Dr. Wesley H. Brewer Engineering Research Center, Rm 13-C Mississippi State University Box 9627 MS State, MS 39762 USA | 1 | 5000 I. Y. Koh | 1 |
| | | 5040 P. Yarnall, Jr. | 1 |
| | | 5050 B. L. Webster | 1 |
| | | 5060 D. A. Walden | 1 |
| | | 5080 J. R. Lee | 1 |
| Dr. William B. Morgan 110 Upton Street Rockville, MD 20850-1836 USA | 1 | 5100 M. J. Davis | 3 |
| | | 5102 B. C. Hornaday | 3 |
| | | J. M. Cutbirth | 3 |
| | | 5200 W. G. Day, Jr. | 1 |
| Dr. George Papadopoulos Dantec Dynamics, Inc. 777 Corporate Drive Mahway, NJ 07430-2008 USA | 1 | 5300 J. W. Johnston | 1 |
| | | D. B. Coakley | 1 |
| | | 5400 M. J. Donnelly | 1 |
| | | R. J. Etter | 1 |
| | | J. J. Gorski | 1 |
| Mr. Richard B. Philips Bldg. 990/1, Code 102 Naval Undersea Warfare Center Newport Division Newport, RI 02841 | 3 | S. D. Jessup | 1 |
| | | J. T. Park | 3 |
| | | K. D. Remmers | 1 |
| | | R. P. Szwerc | 1 |
| | | M. B. Wilson | 1 |
| | | 5500 T. R. Applebee | 1 |
| Dr. L. Patrick Purtell Office of Naval Research, Code 333 800 North Quincy Street Arlington, VA 22217-5660 USA | 3 | 5600 E. S. Ammeen | 1 |
| | | 7051 W. K. Blake | 1 |
| | | 7200 P. C. Shang | 1 |
| | | 7250 D. A. Noll | 1 |
| DTIC | 1 | Library | 2 |

This page intentionally left blank.